ISOSPIN DEPENDENCE OF FRAGMENTATION

A Dissertation

by

SARAH NICOLE SOISSON

Submitted to the Office of Graduate Studies of
Texas A&M University
in partial fulfillment of the requirements for the degree of

DOCTOR OF PHILOSOPHY

December 2010

Major Subject: Chemistry

ISOSPIN DEPENDENCE OF FRAGMENTATION

A Dissertation

by

SARAH NICOLE SOISSON

Submitted to the Office of Graduate Studies of
Texas A&M University
in partial fulfillment of the requirements for the degree of

DOCTOR OF PHILOSOPHY

Approved by:

Chair of Committee,	Sherry J. Yennello
Committee Members,	Che-Ming Ko
	Rand L. Watson
	Joseph B. Natowitz
Head of Department,	David H. Russell

December 2010

Major Subject: Chemistry

ABSTRACT

Isospin Dependence of Fragmentation. (December 2010)

Sarah Nicole Soisson, B.S., Stetson University

Chair of Advisory Committee: Dr. Sherry J. Yennello

Multifragmentation reactions have been used to study many of the complexities of the nucleus. Recently, work has been done to tie observables from multifragmentation reactions to astrophysical observables used in supernova explosions. To make this connection, it is necessary to have a highly excited, equilibrated system. The creation of a highly excited system is done for this dissertation by the reaction of one projectile, ^{32}S, on three targets, ^{112,124}Sn and ^{nat}Au at 45 MeV/nucleon. The forward array using silicon technology, FAUST, was used to collect the fragments produced from the excited projectiles. The motivation for this study was to isotopically identify the fragmenting source and to understand the relationship between its N/Z and the resulting fragmentation. This can then be used to constrain theoretical models which predict the evolution of supernova explosions.

Using an isotropically identified source, the resulting fragmentation of the projectile has been studied. It is shown that there are dependencies on the fragment mass distribution, fragment charge distribution and source excitation energy from the source N/Z. Looking more specifically at the fragments produced, it was found that there is a parallel velocity anisotropy in the particle emission. This anisotropy is found to be a direct result of the presence of an external Coulomb field. Using DIT+SMM theoretical calculations, the anisotropy has been found to be dependent on the distance at which the projectile breaks up from the target (external Coulomb field). As the parallel velocity is related to the angle of emission, it is of interest to extract out the average kinetic energy of each isotope to determine if there are

differences in the average kinetic energy by the angle of emission. It is found that the average kinetic energy is dependent on the emission angle in the quasi-projectile frame. Because of this, care should be taken when comparing between systems to ensure similar regions are being compared. However, the observation that the average kinetic energy changes as a function of the emission angle is not dependent on the presence of an external Coulomb field. Using DIT+SMM calculations, the differences between the average kinetic energy from different angles of emission are seen even when no external Coulomb field is present. These changes are attributed to the angular momentum. In all cases, a statistical framework, supplied by DIT+SMM calculations, can explain many phenomena seen from a fragmenting nucleus. However, the accuracy of the model varies when moving from a neutron-poor to a neutron-rich source.

To my best friend.

TABLE OF CONTENTS

LIST OF TABLES

TABLE Page

LIST OF FIGURES

FIGURE Page

FIGURE Page

FIGURE Page

FIGURE Page

FIGURE Page

FIGURE Page

FIGURE Page

FIGURE Page

FIGURE Page

CHAPTER I

INTRODUCTION

In the past several decades, multifragmentation reactions have been used to study many of the complexities of the nucleus [1–37]. Recently, work has been done to tie observables from multifragmentation reactions to astrophysical observables used in supernova explosions [38]. To make this connection experimentally, it is necessary to have a highly excited, equilibrated system. Type II supernova explosions are described by having a huge energy release of several tens of MeV/nucleon and can exhibit statistical equilibrium behavior [39, 40]. These conditions can be easily met by using multifragmentation reactions.

The study of nuclear multifragmentation provides a rich environment for studying hot nuclei in environments surrounded by other nucleons and nuclei, which mimic a supernova interior [41]. It has been demonstrated that the concept of an equilibrated source can be used to explain violent multifragmentation reactions [37]. In other words, multifragmentation reactions create a highly excited system that exhibits equilibrium properties. This allows one to extract properties of hot nuclei in environments with other nuclear species. The extracted information can possibly be used to constrain parameters for more realistic calculations of the nuclear composition of stellar matter. There are many different types of reactions that can lead to multifragmentation. Broadly these can be divided into two different categories: light-ion and heavy-ion reactions. In light-ion-induced reactions, projectiles are ^{4}He, protons and lighter, more exotic, particles such as pions or anti-protons [11–13, 32, 33]. In these reactions, the target (or compound system) is the source of the fragments as

---

The journal model is Physical Review C.

the projectile mass is small in comparison. For fragmentation to occur these reactions must have a small impact parameter, b, and the beam energy needs to be large enough to ensure that a sufficient deposition of energy into the target nucleus occurs. The energy dissipation in these reactions occurs by nucleon-nucleon scattering. Once the nuclear matter is excited, it begins to expand from internal pressure. From here it is theorized that as the system cools, the system may pass through regions which allow the system to fragment, for example a liquid-gas phase transition or spinodal regions. Heavy-ion induced reactions (where the projectile has $Z > 2$) can be further classified by impact parameter, b, and projectile energy. The following descriptions will follow an impact parameter dependence and as necessary will describe the energy dependence at the impact parameters.

Reactions at the smallest impact parameters are known as central heavy-ion collisions. In these collisions, the projectile needs to have a kinetic energy large enough to overcome the Coulomb barrier between the target nucleus and itself. When the barrier is overcome, a compound nucleus is formed. At the lowest beam energy needed for formation, the compound nucleus is left in an excited state. The excited state is achieved from the conversion of the kinetic energy from the projectile to the internal energy of the compound system. When the target or compound nucleus is excited, it can undergo fission processes, single particle (n, α, etc.) decay, sequential binary decay, or, at high enough excitation energies, multifragmentation.

Increasing the impact parameter from central collisions to more peripheral reactions, there is a dependence on the excitation energy. At low energies in this regime, the time of contact is fairly long and allows for greater interaction between the projectile and target. The projectile and target will interact in an overlap region, rotate around each other and then separate into a projectile-like-fragment (PLF) and a target-like-fragment (TLF). During the interaction time, a portion of the kinetic

energy from the projectile is redistributed into the excitation of the PLF and TLF through nucleon transfers and nucleon-nucleon collisions. Both the PLF and TLF are sources that produce fragments which may or may not be detected. When moving to higher energies at these impact parameters, the interaction between the target and projectile happens on very short time scales and three distinct regions of nucleons can be distinguished. The first region, known as a participant region, is where nucleons from the target and projectile overlap and interact. Those in the other two regions are known as target and projectile spectators. The participant region is highly excited from nucleon collisions and compressional heating [16, 17, 34, 35]. This type of reaction mechanism tends to occur well over the Fermi energy region [42].

Moving to even greater impact parameters, where there is less overlap between the target and projectile, peripheral interactions can occur. In many of these collisions very few nucleon-nucleon collisions and transfer of nucleons between the projectile and target occur. When the projectile energy is sufficiently large, the nucleon-nucleon collisions transfer enough energy to allow fragmentation to occur. Much work has been done in this regime to study the fragmentation of excited projectiles [4,5,12–15].

At the largest impact parameters elastic and inelastic reactions occur. However, these reactions tend to not induce fragmentation. In elastic reactions, only the trajectory of the projectile is changed and no energy goes into the excitation of the target or projectile. For the inelastic reactions, the projectile kinetic energy can go into the excitation of the target and projectile. However, the energy dissipated is low and the probability for fragmentation is low. Regardless of the reaction pathways described above, there have been two classes of theoretical approaches to describe fragmentation of excited nuclei: dynamical and statistical theories.

The first methods used to attempt to describe a fragmenting system were to fit the data from low energy reactions where a well-defined source in both chemical

and thermal equilibrium could be identified. When these conditions are met, the dynamics of the system prior to equilibration has no effect on the distribution of fragments and only an excited source in equilibrium needs to be assumed to perform calculations. However, as one increases the beam energy, reaching an equilibrium state becomes unlikely. If equilibrium conditions are not met, a dependence on the entrance channel may been seen in the excited system. To address this, dynamical theories were developed which treat the colliding nuclei in a time-dependent manner.

A first attempt at describing nuclear collisions was done with the intranuclear cascade (INC) model. This model describes hadron-nucleus collisions [43]. This model originally attempted to treat the multiple collision processes while ignoring any nucleon-nucleon correlations and the nuclear mean field. Moving to heavy-ion collisions [44, 45], the projectile and target are initially treated as cold Fermi gases in their respective potential wells. The only quantum mechanical concept that is included in this model is the Pauli principle. To arrive at highly excited nuclei, the resonant states of the nucleons are produced through nucleon-nucleon scattering.

As mentioned above, if the chemical and thermal equilibrium of a system can be obtained, then the system can be treated statistically. There are two main categories of statistical decay: sequential binary and the simultaneous break-up of the excited nucleus. In sequential binary decay, the excited nucleus is allowed to go through several binary decays that are independent of each other. This theory assumes that there is a long time-scale for fragmentation. The theoretical code GEMINI [36] is a well known code which is based on this type of decay.

The simultaneous break-up of the excited nucleus provides a second type of model. In these models, the fragments are assumed to form in a volume (or density) which approximates the volume or density of the excited system. After this main partitioning occurs, which can have many fragments, it is possible that the fragments

produced could have enough energy to undergo a secondary decay into even smaller fragments. An often used example of this type of decay is the statistical multifragmentation model (SMM) [37]. Of course for GEMINI and SMM, the system must be in equilibrium before it begins to decay. If the assumption of equilibrium cannot be made, dynamical model calculations must be used.

The deep inelastic transfer (DIT) code was developed to describe damped nuclear collisions in the presence of the mean field at low energies. The DIT model depends on the mass transport of nuclear collisions [46]. As two nuclei collide at relatively large impact parameters, a window is opened which allows for the exchange of linear and angular momentum, mass, charge, and energy. The opening of the window is dependent on the potential barriers of the target and projectile. Independent stochastic transfer of nucleons leads to the energy transfer and fluctuations, which in turns leads to an excited quasi-projectile and quasi-target. DIT lacks treatment of nucleon-nucleon collisions even though it does include the nuclear mean-field.

Other dynamical models are appropriate for describing intermediate heavy-ion collisions. In these models the mean-field is used to describe the nuclear potential and collision terms for interacting nucleons. Codes that use this approach are BUU [47–49], LV [50], and BNV [41,51]. More sophisticated codes which include the dependence on isospin have been attempted in [19]. More complete models such as QMD, based on quantum molecular dynamics have also been used to describe intermediate energy heavy-ion collisions [52, 53]. This method uses a wave packet description of nucleons moving in the mean field to model the nucleon collisions and includes clusterization to produce fragments [9, 54]. Current state-of-the-art implementation of these methods are based on the AMD model by A. Ono [55].

It is also worthy to note that several hybrid models exist. They incorporate one or more of the above described methods to describe the various portions of a nuclear

collision. An example would be DIT+SMM. The DIT is used to describe the collision of the projectile and target. It produces hot nuclei which are then de-excited by the SMM model. This framework will be used throughout this work.

To understand the fragmentation process and expand our understanding of supernova explosions, theoretical models need to accurately predict experimental observables. This desire has lead to complex theoretical models and detector systems to study a diversity of nuclear reactions. To help constrain many of the parameters in the theoretical calculations a variety of multifragmentation reactions have been used. However, it is common to use very neutron-rich reactions which lead to neutron-rich sources [56–59]. This neglects trends which could be unique for neutron-poor sources that will not dominate in neutron-rich reactions. Also, these studies are done with very large nuclei. The treatment of very large nuclei proves difficult if a single, well defined source is desired [60,61]. Usually these large, neutron-rich nucleus-nucleus reactions give a wide range of masses which cannot be definitively resolved. This leads to average behaviors which may mask N/Z dependencies that exist in experimental observables.

Specifically in supernova calculations, the Equation of State (EOS) has been under investigation for over 25 years. Many modern day calculations still use one of the first EOS created [62–64]. For an accurate EOS, both light and heavy nuclei in statistical equilibrium need to exist to create a complete ensemble, but many calculations replace the ensemble with an "average" nucleus. This assumption was also used within a mean-field approach to the EOS [65]. Unfortunately, this method is not sufficient for the complete treatment of supernova processes [47, 66–68]. It is believed that this approximation distorts the true statistical ensemble in many cases [69]. Recent theoretical work has attempted to correct some of the deficiencies within a statistical framework [47,66,68]. In these expanded calculations an ensemble

with different nuclear species is used, but the partition sum includes only nuclei in long lived states known from terrestrial experiments. Also, for unknown neutron-rich hot nuclei, only properties of cold and slightly excited isolated nuclei are used.

The work presented here attempts to study some of the limitations in previous works. Three systems were chosen where the same projectile is reacted on three separate targets: ^{32}S + ^{112,124}Sn, ^{nat}Au at 45 MeV/nucleon. These experiments were performed at the Cyclotron Institute at Texas A&M University using the FAUST detector.

These reactions use a relatively small projectile on a comparatively large target. This allows for more peripheral reactions, where the projectile interacts with the target at large impact parameters, to be isolated from more central collisions. The FAUST array allows for the identification of the Z and A of each fragment in an event. This presents the ability to reconstruct the emitting source and know its Z and A with a high degree of accuracy. Once a source (Z, A) is identified, further analysis is done which definitively shows that the source N/Z does influence experimental observables.

In an attempt to understand this N/Z dependence and the physical mechanism of the fragmentation of a nucleus, the experimental data is compared with a hybrid model. The initial stage of the interaction, which produces an excited quasi-projectile, uses the deep inelastic transfer (DIT) model [10]. A statistical equilibrium is assumed and the output of DIT becomes the input for the statistical multifragmentation model (SMM) [37]. The results presented in this work can pave the way to a better refinement in our theoretical understanding of fragmenting nuclei as well as constraining supernova calculations.

CHAPTER II

EXPERIMENTAL

The Forward Array Using Silicon Technology (FAUST) [70] consists of 68 Si-CsI(Tl) detector telescopes arranged in 5 concentric rings, A-E, which are squares projected on a sphere. Each Si-CsI(Tl) telescope is comprised of an edge mounted 2 x 2 cm, 300 μm silicon detector followed by a CsI(Tl) crystal. In rings A-D, the CsI(Tl) crystals are 3 cm in length and in ring E the CsI(Tl) crystals are 2.26 cm in length. This arrangement allows for the FAUST array to cover 1.64° to 44.84° in the laboratory frame. Table I provides detailed information about the detector numbers and angular range in each ring. FAUST provides 90% coverage from 2.31° to 33.63°, 71% from 1.64° to 2.31° and 25% from 33.63° to 44.85°. The cross section of FAUST is shown in Figure 1. This design allows for the inactive area of a ring to be blocked by the active area of the ring in front to maximize the angular coverage. Mylar shielding is also placed in front of the rings of FAUST. Mylar of thickness of 0.833 mg/cm^3 is placed in front of ring E, 2.535 mg/cm^3 in front of ring C, and 4.778 mg/cm^3 in front of ring A. Ring E mylar was misaligned which caused ring D and ring B to have a double set of calibration points. In ring D, a spectrum for particles that passed through no mylar and those that passed through ring E mylar was seen. In ring B, a spectrum for particles that passed through ring C mylar and for particles that passed through both ring C and ring E mylar was seen.

Experimental data was taken at Texas A&M University using beams produced by the K500 Superconducting Cyclotron housed in the Cyclotron Institute. The beam used was 45 MeV/nucleon ^{32}S in a 13+ charge state. The targets chosen were ^{112,124}Sn and ^{nat}Au of thickness (purity) 1.15 mg/cm^2 (99.8%), 1.01 mg/cm^2 (97.2%), and 1.28 mg/cm^2 (100%) respectively. The beam current varied between $20-100$ nA

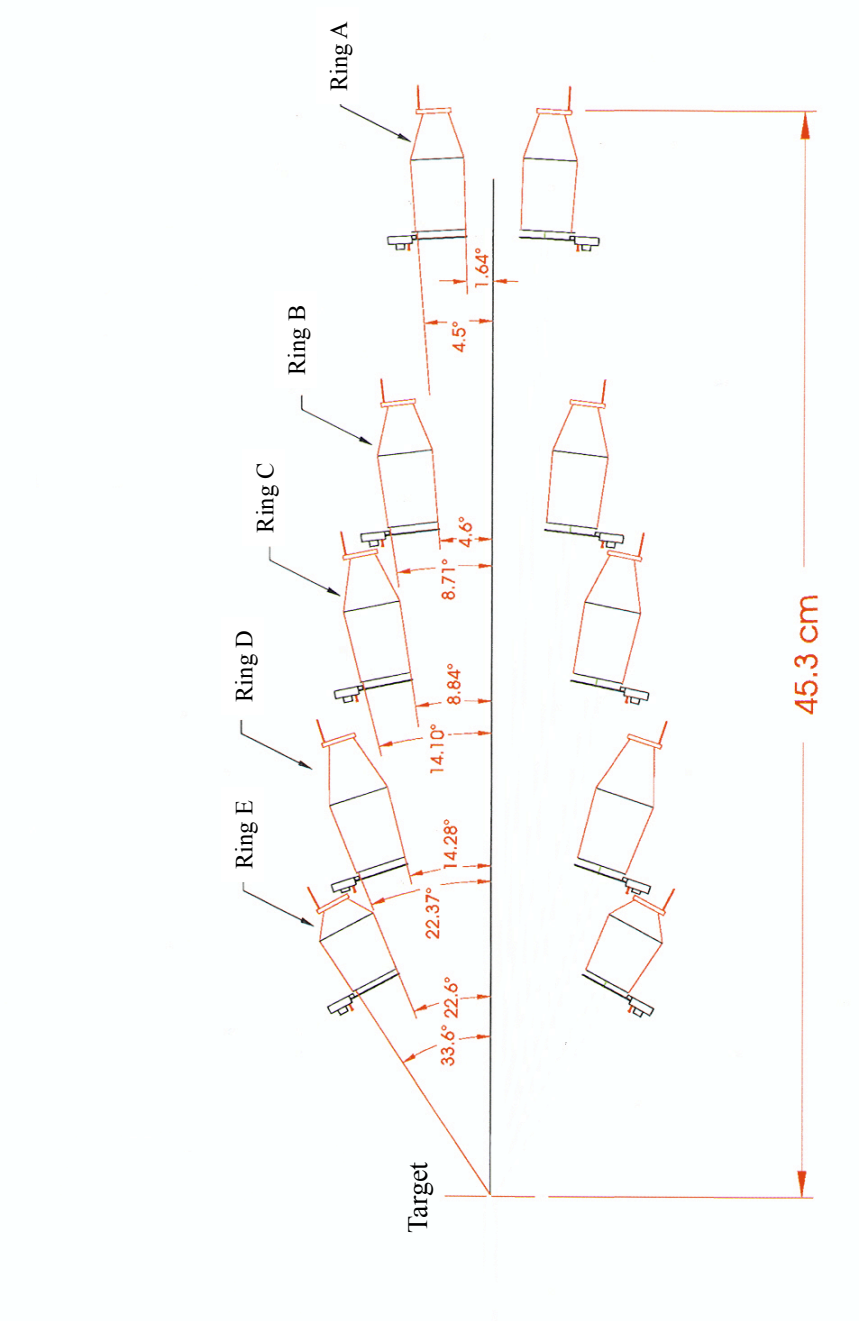

FIG. 1.: Cross section of the FAUST array.

TABLE I.: The detector number range and the angular range of each ring in FAUST.

Ring	Detector Numbers	Angle Range
A	$1-8$	1.64° - 6.36°
B	$9-20$	4.60° - 12.28°
C	$21-36$	8.84° - 19.73°
D	$37-52$	14.30° - 30.77°
E	$53-68$	22.63° - 44.84°

throughout the course of the experiment.

A. Electronics

The electronic signal analysis will be addressed in two sections: the silicon signals and the CsI(Tl) signals. Schematic representation of the electronic and triggering logic can be found in Figure 2, Figure 3, and Figure 4. A description of the modules used is given in Table II.

TABLE II.: Alphabetical list of electronic components used by FAUST.

Electronics Module	Desciption
CAEN C257 Scaler	A single-wide CAMAC module that provides 16 independent 24-bit counting channels [71].
CAEN N568B Amplifier	A single-wide NIM Spectroscopy Amplifier that provides 16 low-noise channels [72].

Table II continued

Electronics Module	Description
CBD 8210	A single-wide VME module which is a CAMAC branch driver. This module allows for a CAMAC branch to be driven from VME [73].
FAUST AC Coupler (Custom Design)	A single-wide NIM module that insures that each NIM signal input is output with only the AC component while the DC component is blocked.
FAUST Amplifier (Custom Design)	A custom-built NIM shaping/timing amplifier with 16-pin header input and output. There are 4 channels per module.
LeCroy 222 Dual Gate Generator	A single-wide NIM module which gives an adjustable width prompt or delayed gate [74].
LeCroy 628 Weighted Fan I/O	A single-wide NIM module that allows an analog or logic signal to be combined or split.
LeCroy 3377 TDC	A single-wide CAMAC module that has 32 input channels for time to digital conversion. It has a high speed ECL port for fast readout. Ran in common stop mode. [75].
LeCroy 3420 CFD	A single-wide CAMAC module which produces logic pulses when the input signal is larger than a given threshold [76].
LeCroy 429A Logic FI/FO	A single-wide NIM module with 4 logic inputs. Each logic input can be output as 2 complementary logic outputs [77].

Table II continued

Electronics Module	Description
LeCroy 4434 Scaler	A single-wide CAMAC module which has an ECL level input [78].
LeCroy 4448 Coincidence Register	A single-wide CAMAC module that gives a logical data level when the inputs is in coincidence with a common fast gate output [78].
LeCroy 4616 ECL-NIM-ECL	A single-wide NIM module that converts ECL to NIM signals or NIM to ECL signals. For each ECL input, three NIM and one ECL outputs are obtained. When one NIM signal is input, one ECL output is given [79].
LeCroy 623B Octal Discriminator	A single-wide NIM module that provides a logic pulse when an analog input exceeds a user set threshold [80].
Ortec Model RD 2000 Rate Divider	A single-wide NIM module that accepts a fast NIM input signal. The output signal is 1/n whose rate corresponds to the input signal rate divided by the set division factor 'n' [81].
Phillips Model 754 Octal 4 fold logic unit	A single-wide NIM logic unit. It contains 4 channels of 4 input logic with veto [82].
Phillips Model 7164/7164H ADC	A 16 channel CAMAC module which converts analog signals to digital signals [83]. Model 6164 has 16 lemo inputs while 7154H has a 32 pin header input.

Table II continued

Electronics Module	Description
Tennelec TC 455 Quad CFD	A single-wide NIM constant fraction discriminator with four independent channels [84].
Zepto Systems Pre-Amplifier	A pre-amplification chip which increases the pulse height of the input signal [85].

The silicon signals first are amplified by a Zepto system pre-amplifier [86]. The amplification was chosen ring by ring depending on the maximum signal height. The signal was chosen to be bipolar. These gains are provided in Table III. From the pre-amplifier the signal continues to the FAUST timing/shaping amplifier, with shaping time of 0.5 ms, which outputs a slow and a fast signal. The slow signal proceeds directly to the Phillips 7164/7164H ADC for collection by the computer. The fast signal goes to a LeCroy 3420 CFD to be processed into the main trigger. Please see Figure 2 for the electronics diagram for the Si signal processing.

For Ring A, the CsI(Tl) signals are first amplified by a Zepto systems 15 mV/MeV pre-amplifier. For Rings B-D, the CsI(Tl) signals were sent to a low noise InterFET N-JFET IFPA300 charge sensitive preamplifier. After the pre-amplifier, each signal continues to the FAUST timing/shaping amplifier with a 0.5 ms shaping time. A bipolar, slow signal is then sent to the Phillips 7164 ADC for collection by the computer. Please see Figure 3 for the electronics diagram for the CsI(Tl) signal processing.

To construct the trigger, the fast silicon signal that is generated by the FAUST amplifier is used. Each channel that is above a threshold signal is first sent to a LeCroy 3420 CFD. Each channel, above threshold, is recorded by a LeCroy 4434 Scaler, a

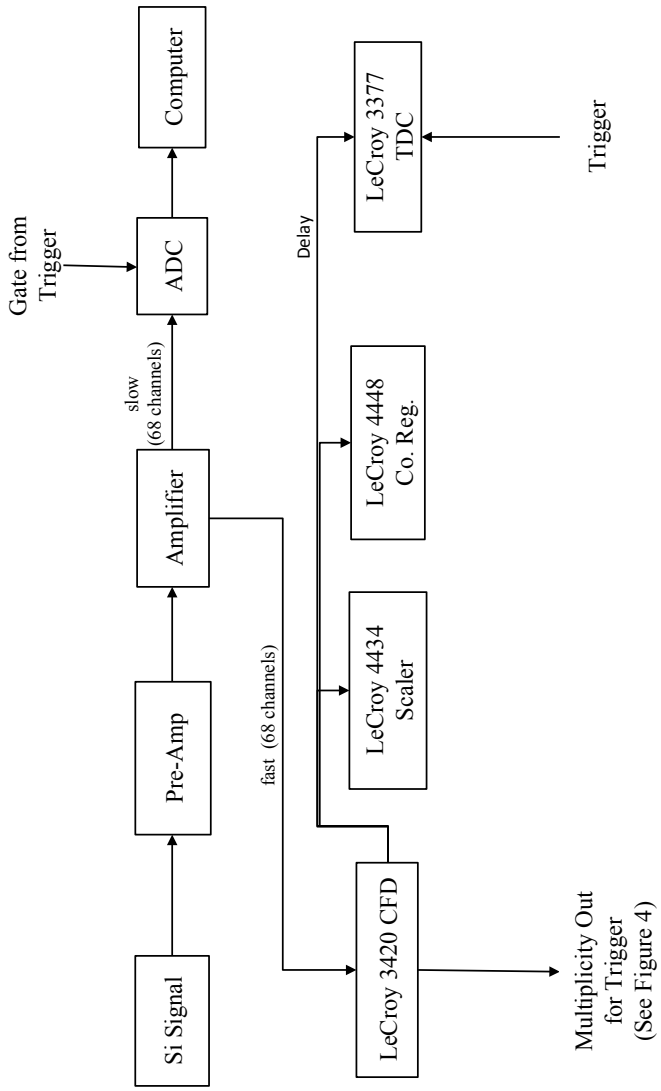

FIG. 2.: Silicon electronics diagram

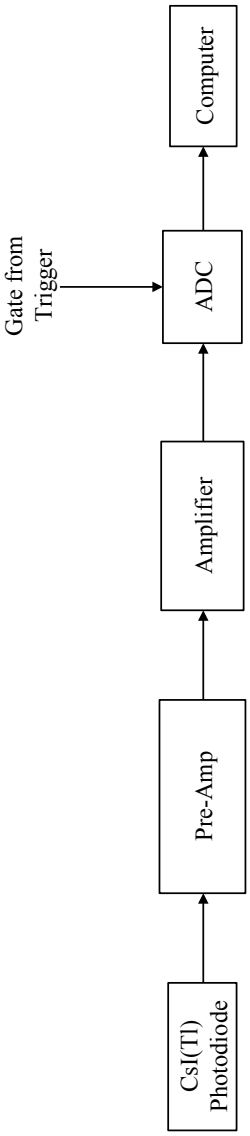

FIG. 3.: CsI(Tl) electronics diagram

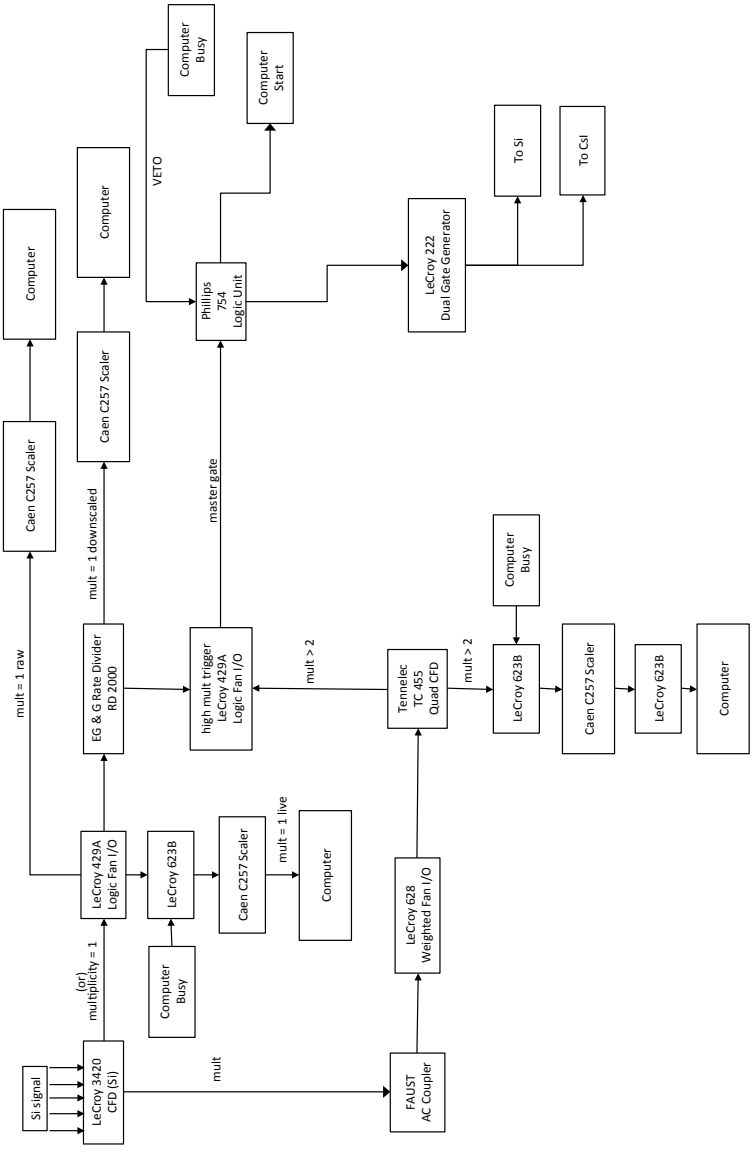

FIG. 4.: Trigger logic diagram

LeCroy 4448 Coincidence Register, and a LeCroy 3377 TDC. The TDC was set in common start mode. From the LeCroy 3420 CFD, 2 signals are produced, a "mult" and an "or". The "or" NIM logic signal is sent to a LeCroy 429A Logic Fan I/O to generate a multiplicity 1 signal. This multiplicity 1 signal from the LeCroy 429A Logic Fan I/O is sent on 3 different paths. The first goes to a Caen C257 Scaler to provide a multiplicity 1 scaler into the computer. The second path is to send the multiplicity 1 signal to a LeCroy 623B discriminator which generates the live multiplicity 1 signal in conjunction with the computer busy. The live multiplicity 1 signal is then sent to the Caen C257 Scaler. This is to determine how many multiplicity 1 events make it through the trigger gate and to the computer. The third path sends the multiplicity 1 signal to the EG & G RD 2000 Rate divider for downscaling.

Throughout the course of the experiment the downscale was set at 25. This downscale allows only 1 for every 25 multiplicity one events to be recorded by the computer. The second output from the CFD is the "mult" signal. It is a NIM signal with is 35 mV in height. Each ring has one CFD. To ensure that the "mult" signals have a common baseline, the signal is passed through the FAUST AC Coupler. From the FAUST AC Coupler the signals are combined in a LeCroy 628 Weighted Fan I/O to generate a total multiplicity signal. This total multiplicity signal then is sent to a Tennelec TD 455 Quad CFD where a multiplicity greater than 2 cut is made. This multiplicity greater than 2 is sent directly to the Caen C257 Scaler and to the Lecroy 623B Discriminator. The downscaled multiplicity 1 from the EG & G Rate Divider RD 2000 and the multiplicity greater than 2 signals are combined in a LeCroy 429A Logic Fan I/O to generate the master gate.

A computer busy signal, or veto, is needed to create the master gate live signal. This busy signal was generated by the CBD 8210 Event Trigger module. This signal is then converted to a NIM signal through a LeCroy 4616 ECL-NIM-ECL module. A

TABLE III.: Silicon pre-amplifier gains

Ring	Pre-Amplifier gain
A	5 mV/MeV
B	5 mV/MeV
C	5 mV/MeV
D	15 mV/MeV
E	15 mV/MeV

LeCroy 429A Logic Fan I/O generates multiple busy vetoes. The master gate and a computer veto are sent to a Phillips 754 Logic Unit to generate a master gate live. This master gate live signal is sent to a LeCroy 222 Dual Gate Generator to create a signal gate for the Phillips 7164/7164H ADC's. The ADCs, Coincidence Registers, TDCs, and the scalers are read by the computer to generate the data stream. The transport manager, developed by K. Hagel, allows for the computer to read the data provided by the CAMAC crates, generate a data stream and write the data to disk for further analysis. The analysis manager, also developed by K. Hagel, allows for real-time access of the data stream. Each detector, scaler and telescope is monitored separately through the analysis manager in real time to determine if the experiment is progressing smoothly.

B. Particle Identification

Particle identification was done using a linearization method that employed the point-to-curve algorithm [87]. First, elemental lines are drawn using user picked points on a two dimensional Si channel vs. CsI(Tl) channel plot. The elemental lines are drawn

on the most intense isotope in a given elemental line. They are typically drawn with $\approx 20 - 30$ user picked points. If one isotope in a given elemental line is not distinguishable over the others, the line was drawn on the lower edge of the elemental line. For each user chosen line, a large number of computer generated points, usually 70, are placed along the user chosen line at a given interval. The interval is determined by the length of the line from the first user chosen point to the last user chosen point divided by the number of computer generated points the user wishes.

In Figure 5 one can see the computer generated points laid on top of the user chosen line. The number of points is defined for each detector to allow for variation in the detector gain and saturation in the silicon. Very large or very small gain will necessitate less or more points respectively to allow for a good point-to-curve distance to be found with no anomalies. Each user picked line was broken into regions where a 2^{nd} or 3^{rd} degree polynomial was fit. An odd number of points was chosen for the region. The number of points is user defined, but usually consisted of 7 points. To define the 7 point region, each computer generated point is defined to be the center of the 7 point region. The 7 points are then fit with a polynomial. This polynomial is stored for later use and referenced by the point which generated it. For the first 7 points a different procedure was used. The first point was the end point of its associated polynomial. For points $2 - 4$, the associated polynomial was constructed as if the points were the second point in the fit. At the high energy tail, a linear line was fit to the last 7 points. Figure 6 shows the overlying polynomials constructed from the spline fitting of the 7 points. The polynomial constructed from each spline fit is shown and has a different color. As shown, the polynomials lie on top of one another and trace the shape of the elemental line.

For each particle recorded, its Si channel and CsI(Tl) channel are compared to each elemental line drawn to determine which two chosen lines the point falls between.

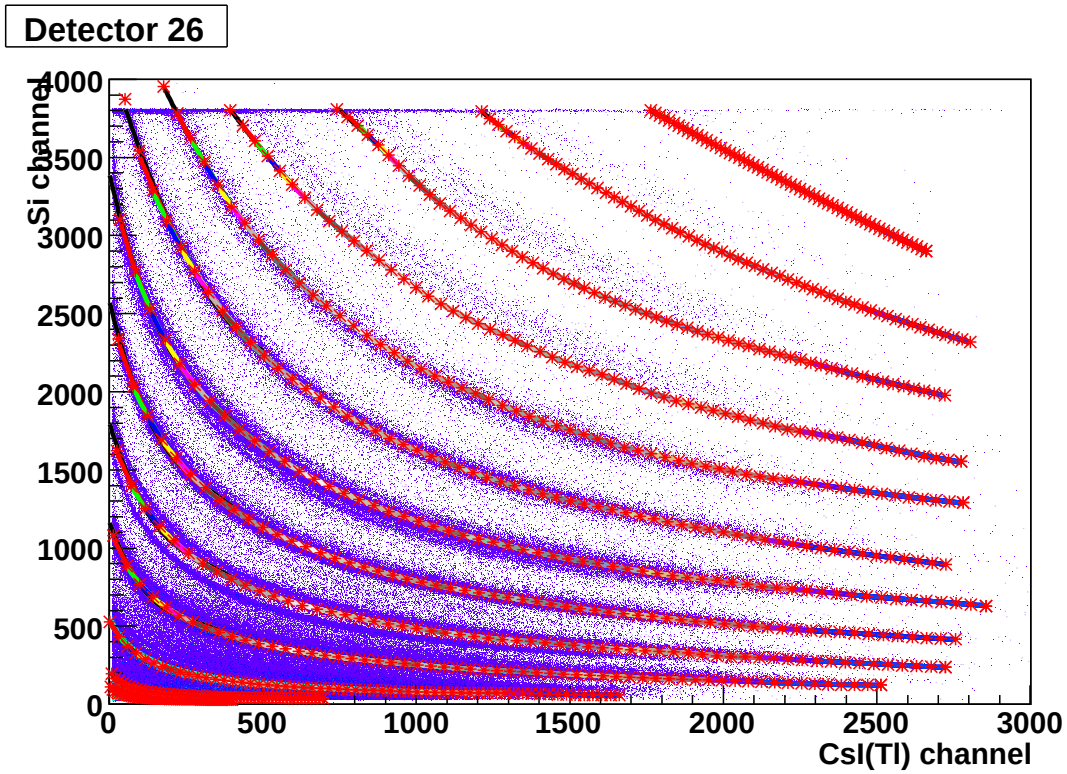

FIG. 5.: Silicon channel vs. CsI(Tl) channel plot with the computer generated points.

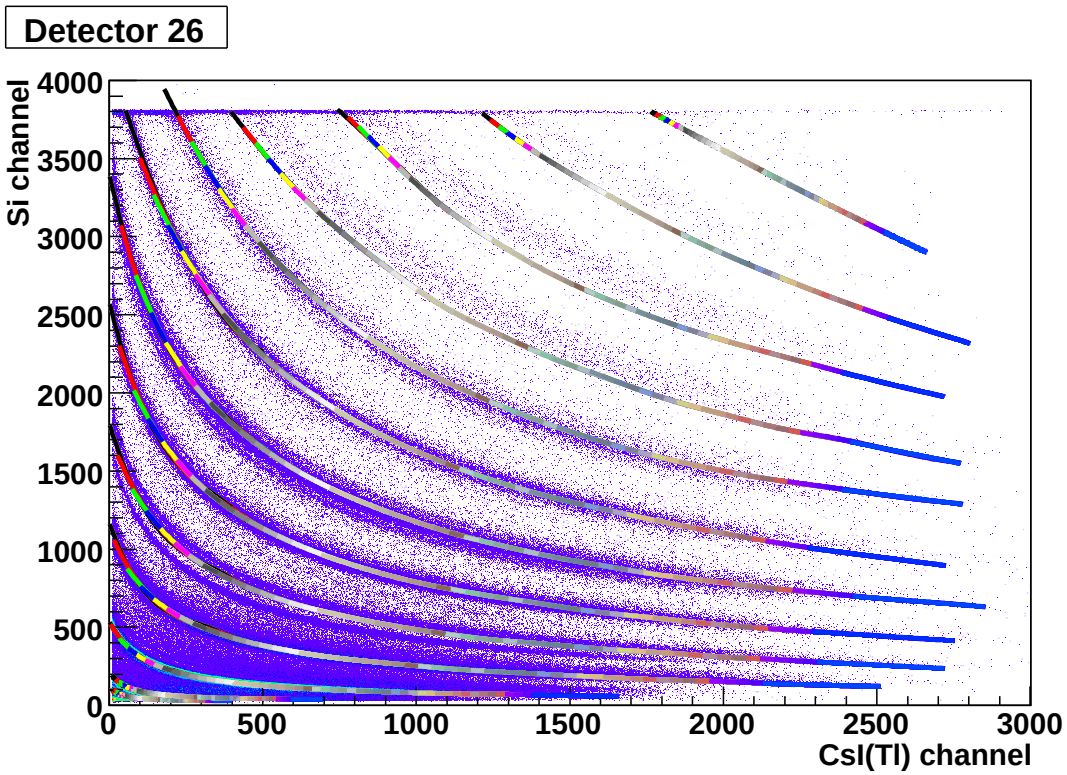

FIG. 6.: Si channel vs. CsI(Tl) channel with the polynomial fits. Each color along an elemental band represents an individual spline fit.

To determine which lines the particle falls between, the coordinates of the particle are compared to each computer generated point to determine the closest point. Once the closest point has been determined, the corresponding polynomial as defined above is used to find the closest point within the polynomial region using the point-to-curve algorithm [87]. An example of this method is given in Figure 7. The black star in Figure 7 corresponds to a given charged particle. The red lines extending from the black star show the closest point to the given polynomials.

Each user picked line is adjusted, and the procedure above is repeated, until the resulting linearized Z vs. CsI(Tl) plot yields a linear relationship. This relationship is shown in Figure 8. The curvature along the lower edge of the bands at high Z values corresponds to the elemental band not reaching the y-axis on the Si vs. CsI(Tl) plot as it deposits enough energy in the silicon to not register within the range of the ADC.

Once straight lines are achieved as illustrated in Figure 8, a one dimensional projection of the x-axis is generated as shown in Figure 9. Zooming in on each Z band, the isotopes of a given Z are determined by fitting Gaussians to the resulting peaks. An example is given in Figure 10. For Be (Z = 4), Gaussian 1, which defines ^{9}Be, is blue and Gaussian 2, which defines ^{10}Be, is in green. For the region represented in Figure 10, all particles that are between the two red lines are identified as $Z = 4$, Be. To assign an isotopic identity, a vertical line is defined where Gaussian 1 and Gaussian 2 intersect. To the left of this line is the isotope identified as ^{9}Be and to the right of this line, the isotope is identified as ^{10}Be. On the left side of our vertical line shown in Figure 10(b), we look at the Gaussian 1 (blue) in relation to Gaussian 2 (green). A second point is defined where Gaussian 2 (green) is only 5% of the height of Gaussian 1 (blue). This point is represented by a dashed line. Anything to the left of this dashed line is defined as ^{9}Be and anything between the dashed line and the solid

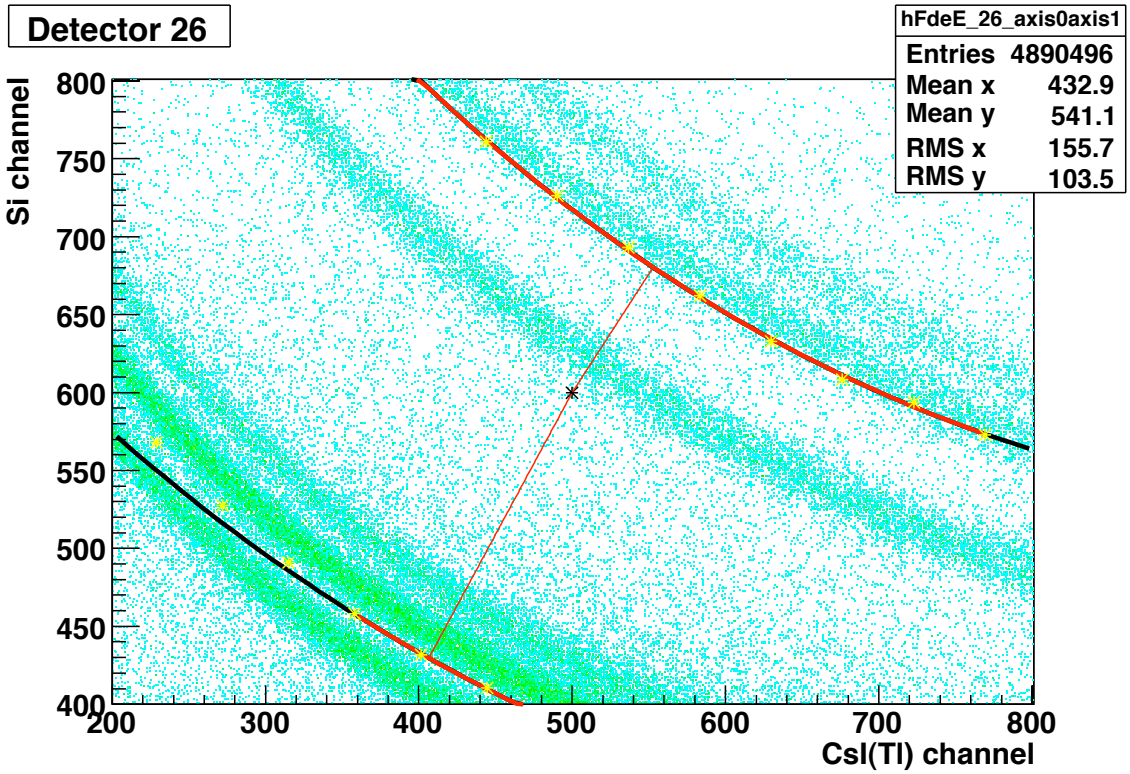

FIG. 7.: Silicon channel vs. CsI(Tl) channel plot illustrating the procedure used to define the two closest lines for a given point. The black star represents a given point (charged particle). Each yellow star is a computer generated point which represents the user chosen elemental lines. The closest polynomials are shown in red, overlapping with the computer chosen points. The extension of these polynomials is represented by black lines. These extensions do not follow the curvature of the computer generated lines demonstrating the necessity of having multiple polynomials for different ranges of the elemental lines. The thin red lines extending from the black star show the closest distance on each of the polynomials.

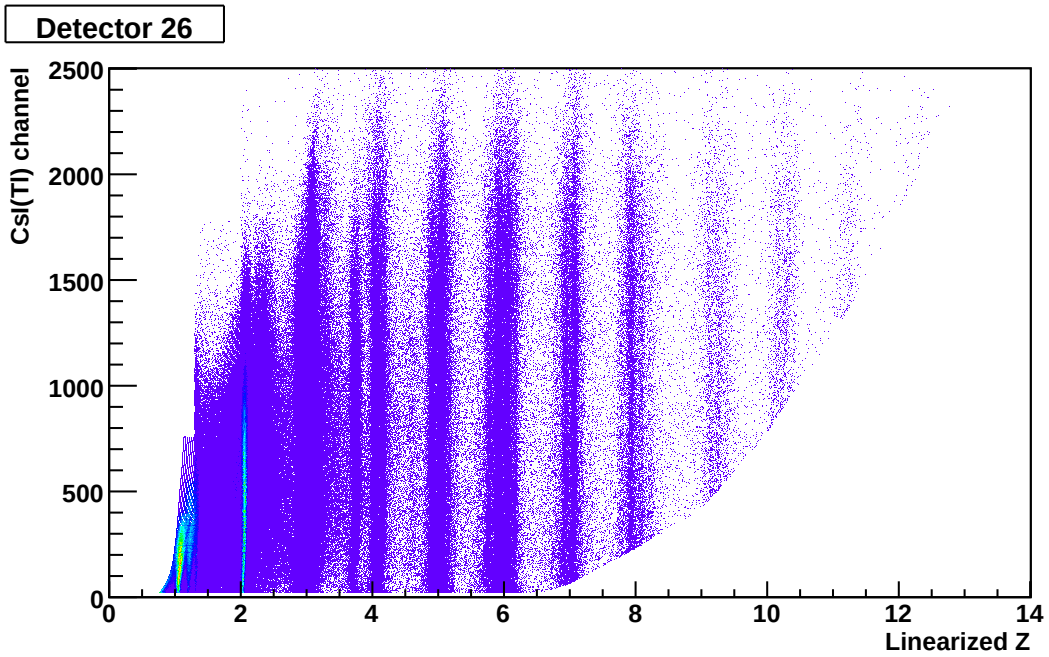

FIG. 8.: An example of a linearized Z vs. CsI(Tl) channel plot. The linearized Z on the x-axis corresponds to the silicon axis on the Si vs. CsI(Tl) plots. The curvature at high Z values correspond to the elemental band not reaching the y-axis on the Si vs. CsI(Tl) plot as it deposits enough energy in the silicon to not register within the range of the ADC.

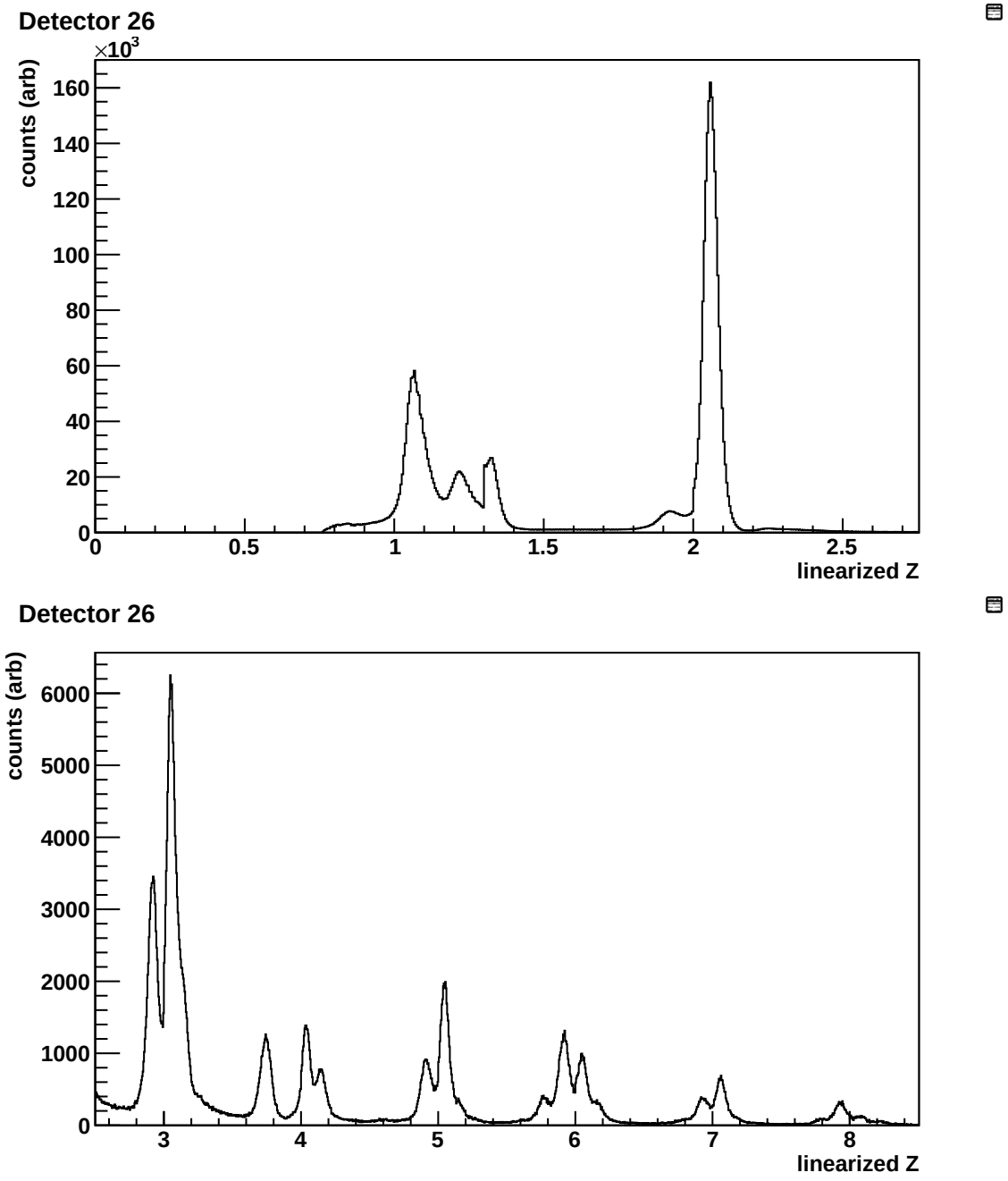

FIG. 9.: Projected results of the linearization procedure. The top panel shows the $Z = 1 - 2$ region while the bottom pane shows the $Z = 3 - 8$ region for detector 26.

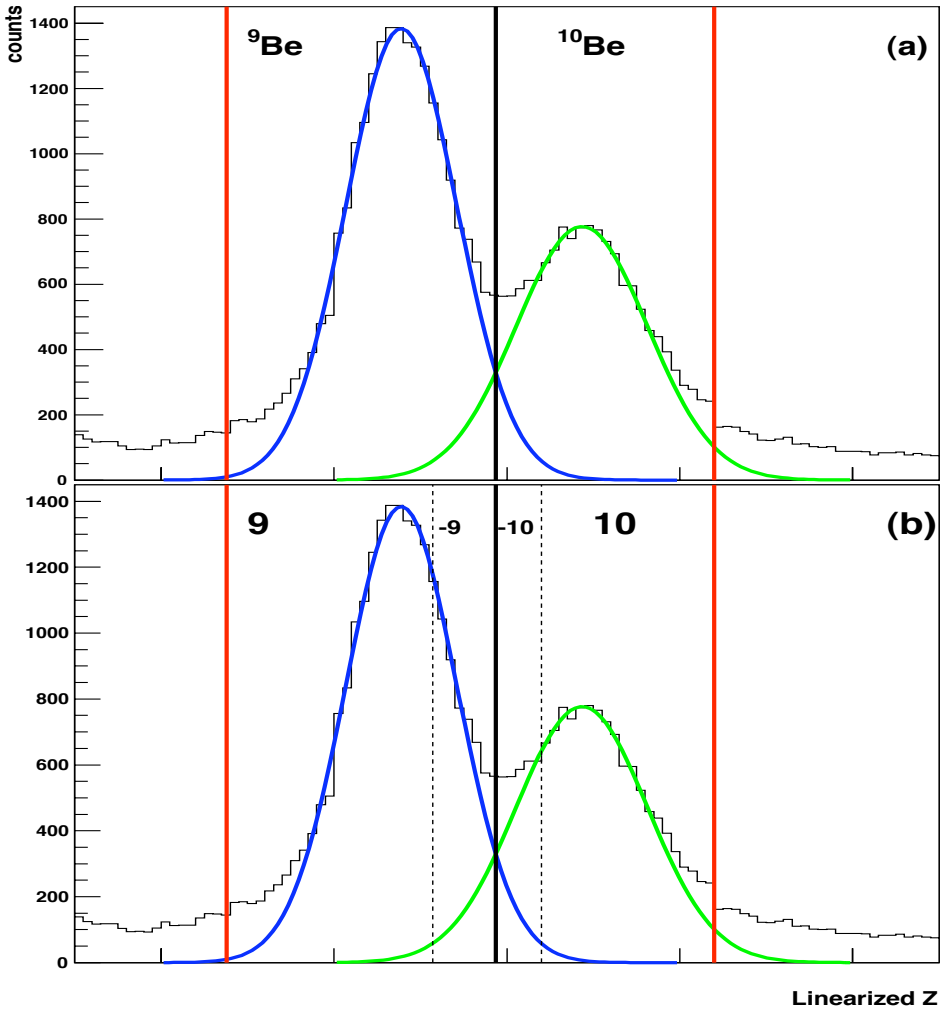

FIG. 10.: Example of particle identification using Gaussians. a)Gaussians used for particle identification. Blue, Gaussian 1, is for ^{9}Be and green, Gaussian 2, is for ^{10}Be. The solid vertical line is the division between the two isotopes as defined by the point where Gaussian 1 and Gaussian 2 cross. b) Same definitions as in (a). The dotted vertical line is the divisions created when Gaussian 2 is only 5% the height of Gaussian 1. Within the range presented in this figure, the red lines represent the outer limits within which an element is defined.

line is defined as ^{9}Be but is flagged as a negative A, to represent that we do not meet at 95% confidence in the identification of the isotope for that region. To eliminate noise between the elements and isolated isotopes (ex. ^{7}Be) upper and lower limits are imposed on the element/isotope range. These limits are user chosen to be the point where the Gaussian visually begins to become greater than the baseline (which may or may not be zero). This prescription is repeated for every isotope/element identified in a given detector. For elements where there is no isotopic bands/Gaussians visible, the isotope that is the most naturally abundant is assigned and is flagged as negative. Once the particle is identified, its energy is calibrated.

Table IV shows the effect of the confidence cut described above for select isotopes. This table represents the percentage of those isotopes which meet the 95% identification confidence out of those which are generally identified as the isotope. It also includes the percentage as a function of center-of-mass angle. While every value is different, and there appears to be no systematic trend, it is suggested that the following things be kept in mind when evaluating the validity of this method. The overlap of the identification Gaussians is dependent on the two isotopes in question. For those which are the most neutron-poor and neutron-rich isotopes (ex. ^{11}C and ^{14}C) there is only one overlapping Gaussian which causes contamination from the adjacent isotope. If there is both a neutron-poor and neutron-rich adjacent isotopes to the one in question (ex, ^{12}C), there are two sources of contamination. Also, the perceived contamination is also a function of the Gaussian overlap. Gaussians which have a small height (or large width) in comparison to an adjacent one, have the potential to have more overlap and thus contamination from the larger (or wider) Gaussian. Also the reader is reminded that if isotopic identification could not be achieved for a given element, the entire element band was labeled as the most probable isotope based on natural abundances and flagged as negative. This effect is large for oxygen

and is seen with the low percentage of identified isotopes for ^{16}O.

TABLE IV.: The isotopic yield before and after a 95% confidence cut. The values represent the isotopically identified isotope with a 95% confidence as a percentage of those identified using the method described in text. The first column is for all center-of-mass angles, while the following four columns are for center-of-mass angles in 45° increments.

Isotope	all θ (%)	$0° - 45°$ (%)	$45° - 90°$(%)	$90° - 135°$(%)	$135° - 180°$(%)
^{3}He	55.73 ± 0.05	49.71 ± 0.09	58.29 ± 0.08	58.94 ± 0.08	49.12 ± 0.12
^{4}He	66.05 ± 0.02	66.90 ± 0.04	67.88 ± 0.03	66.69 ± 0.03	61.90 ± 0.03
^{6}He	54.22 ± 0.13	58.02 ± 0.45	54.54 ± 0.25	54.00 ± 0.20	52.80 ± 0.26
^{6}Li	63.50 ± 0.08	62.34 ± 0.18	65.67 ± 0.16	64.47 ± 0.15	59.65 ± 0.19
^{7}Li	56.21 ± 0.07	55.90 ± 0.14	56.77 ± 0.12	57.19 ± 0.12	54.07 ± 0.15
^{8}Li	47.82 ± 0.11	39.80 ± 0.29	47.40 ± 0.21	51.07 ± 0.17	45.88 ± 0.22
^{7}Be	70.58 ± 0.14	72.57 ± 0.28	72.83 ± 0.25	69.27 ± 0.24	65.26 ± 0.35
^{9}Be	61.10 ± 0.14	60.72 ± 0.32	62.64 ± 0.28	62.01 ± 0.25	57.99 ± 0.30
^{10}Be	55.95 ± 0.19	54.88 ± 0.43	58.41 ± 0.37	57.42 ± 0.32	50.63 ± 0.40
^{10}B	58.67 ± 0.14	56.68 ± 0.28	91.00 ± 0.27	59.90 ± 0.26	55.50 ± 0.32
^{11}B	58.03 ± 0.11	56.34 ± 0.24	59.48 ± 0.22	59.16 ± 0.21	55.96 ± 0.26
^{12}B	44.15 ± 0.26	41.68 ± 0.56	46.48 ± 0.52	46.49 ± 0.45	39.37 ± 0.55
^{11}C	49.77 ± 0.19	47.58 ± 0.33	52.30 ± 0.35	51.71 ± 0.38	45.62 ± 0.47
^{12}C	46.70 ± 0.09	44.43 ± 0.17	49.73 ± 0.18	45.56 ± 0.17	47.17 ± 0.24
^{13}C	45.32 ± 0.13	43.09 ± 0.24	46.69 ± 0.24	46.56 ± 0.25	44.47 ± 0.30
^{14}C	43.52 ± 0.22	42.43 ± 0.44	45.72 ± 0.43	45.62 ± 0.43	37.84 ± 0.49
^{13}N	39.67 ± 0.32	37.32 ± 0.56	42.80 ± 0.62	42.37 ± 0.70	34.18 ± 0.75
^{14}N	26.15 ± 0.09	24.52 ± 0.15	28.88 ± 0.17	24.36 ± 0.16	27.44 ± 0.23

Table IV continued

Isotope	all θ(%)	$0^\circ - 45^\circ$ (%)	$45^\circ - 90^\circ$(%)	$90^\circ - 135^\circ$(%)	$135^\circ - 180^\circ$(%)
^{15}N	53.46 ± 0.16	51.95 ± 0.31	53.82 ± 0.29	54.43 ± 0.32	53.72 ± 0.40
^{16}N	37.39 ± 0.35	36.47 ± 0.68	39.16 ± 0.64	39.34 ± 0.72	32.43 ± 0.79
^{15}O	55.45 ± 0.47	55.42 ± 0.86	55.54 ± 0.81	55.01 ± 0.97	56.13 ± 1.33
^{16}O	14.94 ± 0.05	12.16 ± 0.08	16.78 ± 0.10	16.95 ± 0.12	14.40 ± 0.14
^{17}O	33.16 ± 0.27	32.92 ± 0.51	33.55 ± 0.46	33.81 ± 0.54	31.48 ± 0.69
^{18}O	34.95 ± 0.41	34.76 ± 0.79	35.46 ± 0.73	35.07 ± 0.81	28.97 ± 0.96

C. Energy Calibration

1. Silicon Calibration

At the beginning, middle, and end of the experiment a ^{228}Th α source was placed in front of FAUST. This allowed for known low energy peaks to be detected in the silicon detectors. These α peaks, along with punch-in values for higher elements and beam spots in forward angles allowed for each silicon detector to be energy calibrated. A punch-in is defined as the point where a given particle has enough energy to completely pass through the silicon detector and is first seen, or "punched-in" to the CsI(Tl). The values for the punch-in points was taken from the Orsay tables [88]. Although the average silicon detector is 300 μm in thickness, the actual thickness was used for each individual silicon detector for calculating the punch-in value. Table V provides the α energy peaks used for the experiment along with their values after a given thickness of mylar.

TABLE V.: ^{228}Th α energy peaks. For each of the six peaks, the original energy plus the energy after a given thickness of mylar is shown.

		Energy (MeV) after given thickness of mylar			
peak	E (MeV)	0.833 mg/cm^3	2.535 mg/cm^3	3.368 mg/cm^3	4.778 mg/cm^3
1	5.423	4.703	2.801	1.947	–
2	5.686	4.995	3.260	2.457	–
3	6.051	5.390	3.774	3.095	–
4	6.288	5.648	4.078	3.475	1.208
5	6.778	6.174	4.719	4.201	2.372
6	8.784	8.281	7.171	6.861	5.604

TABLE VI.: The detector number, silicon thickness and the values used for calibration of the silicon detector. Please see Table V to reference the peak number to the energy value seen in the silicon detector. Please see text for mylar discussion. Detectors listed as NA are those with no signal or an unusable signal while those listed as silicon saturated are discussed separately.

Detector #	Thickness (μm)	Points Used in Silicon Calibration
1	310	peak 5, peak 6, beam spot
2	310	peak 5, peak 6, beam spot
3	311	peak 5, peak 6, beam spot
4	306	NA
5	311	^{4}He, ^{7}Li, ^{9}Be, ^{11}B, ^{12}C,^{14}N, ^{16}O, ^{20}Ne
6	311	peak 5, peak 6, beam spot

Table VI continued

Detector #	Thickness (μm)	Points Used in Silicon Calibration
7	307	peak 5, peak 6, beam spot
8	311	peak 5, peak 6, beam spot
9	306	NA
10	311	peak 1, peak 2, peak 4, peak 5, peak 6, beam spot
11	301	NA
12	305	silicon saturated
13	304	peak 1, peak 2, peak 4, peak 5, peak 6
14	304	peak 1, peak 2, peak 4, peak 5, peak 6, beam spot
15	311	peak 1, peak 2, peak 4, peak 5, peak 6
16	304	NA
17	312	peak 1, peak 2, peak 4, peak 5, peak 6, beam spot
18	301	peak1, peak 2, peak 4, peak 5, peak 6, beam spot
19	306	peak 2, peak 4, peak 5, peak 6, beam spot
20	306	peak 1, peak 2, peak 4, peak 5, peak 6, beam spot
21	311	silicon saturated
22	313	peak 1, peak 2, peak 4, peak 5, peak 6, peak 6 no mylar, ^{4}He, ^{7}Li
23	308	peak 1, peak 2, peak 4, peak 5, peak 6, peak 6 C+E mylar
24	301	peak 1, peak 2, peak 4, peak 5, peak 6
25	301	peak 1, peak 2, peak 4, peak 5, peak 6
26	298	peak 1, peak 2, peak 3, peak 4, peak 5, peak 6 C + E mylar, peak6 C mylar

Table VI continued

Detector #	Thickness (μm)	Points Used in Silicon Calibration
27	301	peak 1, peak 2, peak 3, peak 4, peak 5, peak 6 C + E mylar, peak6 C mylar
28	306	peak 1, peak 2, peak 3, peak 4, peak 5, peak 6 C + E mylar, peak6 C mylar
29	311	peak 1, peak 2, peak 4, peak 5, peak 6, ^{11}B
30	311	peak 1, peak 2, peak 4, peak 5, peak 6, ^{11}B
31	305	peak 1, peak 2, peak 4, peak 5, peak 6
32	311	peak 1, peak 2, peak 4, peak 5, peak 6, ^{11}B, ^{12}C
33	308	peak 1, peak 2, peak 4, peak 5, peak 6, ^{12}C
34	310	peak 1, peak 2, peak 3, peak 4, peak 5, peak 6, ^{12}C
35	311	peak 1, peak 2, peak 3, peak 4, peak 5, peak 6, ^{11}B
36	307	NA
37	298	silicon saturated
38	298	silicon saturated
39	298	silicon saturated
40	298	peak 1, peak 2, peak 3, peak 4, peak 5, peak 6, ^{9}Be
41	298	NA
42	306	peak 1, peak 2, peak 3, peak 4, peak 5, peak 6, ^{9}Be
43	306	peak 1, peak 2, peak 3, peak 4, peak 5, peak 6, ^{9}Be
44	298	peak 1, peak 2, peak 3, peak 4, peak 5, peak 6
45	310	peak 1, peak 2, peak 3, peak 4, peak 5, peak 6
46	300	peak 1, peak 2, peak 3, peak 4, peak 5, peak 6, ^{9}Be

Table VI continued

Detector #	Thickness (μm)	Points Used in Silicon Calibration
47	306	silicon saturated
48	306	peak 1, peak 2, peak 3, peak 4, peak 5, peak 6, ^{9}Be
49	308	peak 1, peak 2, peak 4, peak 5, peak 6, ^{9}Be
50	300	peak 1, peak 2, peak 3, peak 4, peak 5, peak 6, ^{9}Be
51	300	peak 1, peak 2, peak 3, peak 4, peak 5, peak 6
52	300	peak 1, peak 2, peak 5, peak 6 w/mylar & peak 1, peak 4, peak 5, peak 6 no mylar
53	311	silicon saturated
54	311	silicon saturated
55	302	silicon saturated
56	311	silicon saturated
57	298	NA
58	298	silicon saturated
59	306	silicon saturated
60	310	silicon saturated
61	298	silicon saturated
62	306	silicon saturated
63	298	silicon saturated
64	302	silicon saturated
65	302	silicon saturated
66	302	silicon saturated
67	301	silicon saturated

Table VI continued

Detector #	Thickness (μm)	Points Used in Silicon Calibration
68	301	NA

Table VI provides the detector number, silicon thickness, and values that were used for silicon calibration (α energy peaks, beam spot and/or element Si punch-through). Please reference Table V for the peak number and its energy value seen in the silicon detector. Some silicon detectors experienced saturation in the signal which needed to be unfolded. Discussion of this will occur in the next section. Detectors that had no signal or have an unusable signal are marked as NA.

When measuring particle types that are similar in size, such as protons and alphas, a silicon detector responds linearly when relating the deposited energy and the pulse height. To have an energy calibration be as precise as possible, it is always best to calibrate the detector with the given radiation type(s) such as gammas, light charged particles, heavy elements, etc. [89] This is the reasoning for the variety of types of points used in the silicon calibration as described in Table VI. To compensate for detectors that only had the ^{228}Th α peaks the resulting calibrated energy spectrum was compared to the energy spectrum from detectors which had multiple sources for calibration to determine the accuracy of the energy calibration. An example of this procedure will be demonstrated with the silicon calibration for detector 42. In the top panel of Figure 11 we see the ^{228}Th α spectrum and in the bottom panel of Figure 11 the 2 dimensional plot of Si vs. CsI(Tl) is shown. The points used in the silicon calibration for detector 42 are the 6 peaks in the α spectrum and the punch-through

value for ^{9}Be. The energies for the α peaks are given in Table V while the punch-in values are constructed from the Orsay tables for ^{9}Be. Only ^{9}Be was chosen for detector 42 for the following reasons: the Orsay tables directly give the punch-through value and the punch-through value could be clearly chosen on the Si vs. CsI(Tl) plot. These energy values along with their subsequent Si channel number are plotted in Figure 12. The black points are the calibration points. To these points a best fit straight line is determined which fits the equation $E_{Si} = m * channel_{Si} + \text{offset}$, represented by the red line in Figure 12. This relates the channel number recorded by the computer to the energy deposited in the silicon.

As discussed above, some silicon detectors signals are saturated. The saturation is a non-linear compression of the signal to fit the range of the ADC. It is unclear why this presented itself in some detectors and not others. Table VI notes which silicon detectors were saturated during the experiment while Figure 13 shows an example of this saturation.

As shown, the isotopic and elemental bands are seen to perform a 'back bending' behavior once you are above Si channel 2000. To correct for this behavior the following technique was used. The α peaks are taken along with as many isotopic punch-in values that can be inferred from the 2-D spectrum. The punch-in is defined as the point at which a particle passes through the silicon detector and is first seen in the CsI(Tl) detector. The energy for each punch-in is derived from the Orsay tables [88]. All energies have been corrected for the loss of energy through the corresponding mylar. The equation to unfold the silicon energy needs to account for the linear portion and the saturation portion of the range presented. For each point that lies in the "normal" region of the spectrum (Si channels less than 2000 in the example detector), the five ^{228}Th α peaks, p, t, ^{4}He, and ^{7}Li, are used and the calibration is done as described above. Then, each point above the saturation point, ^{9}Be, ^{11}Be, and

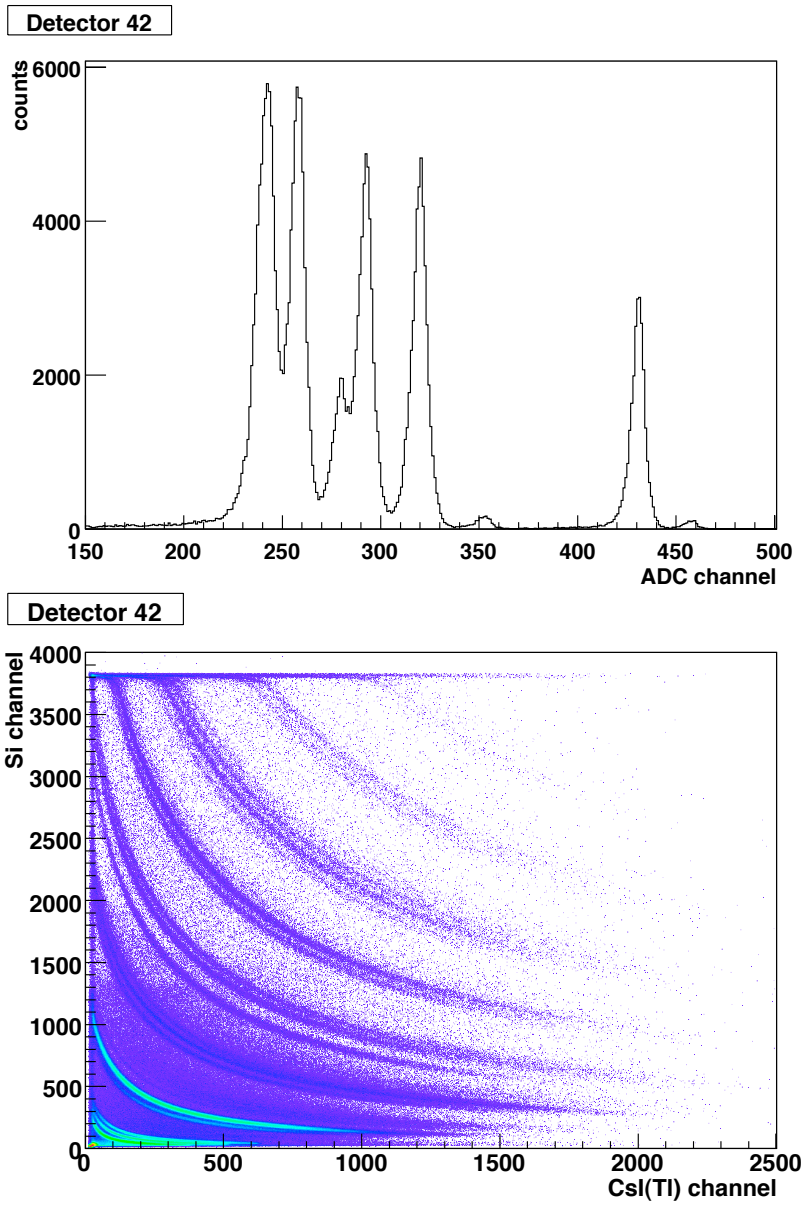

FIG. 11.: Top panel, silicon calibration points from ^{228}Th for detector 42. Bottom panel, silicon channel vs. Cs(Tl) channel spectrum. The ^{9}Be punch-in occurs at channel 3800.

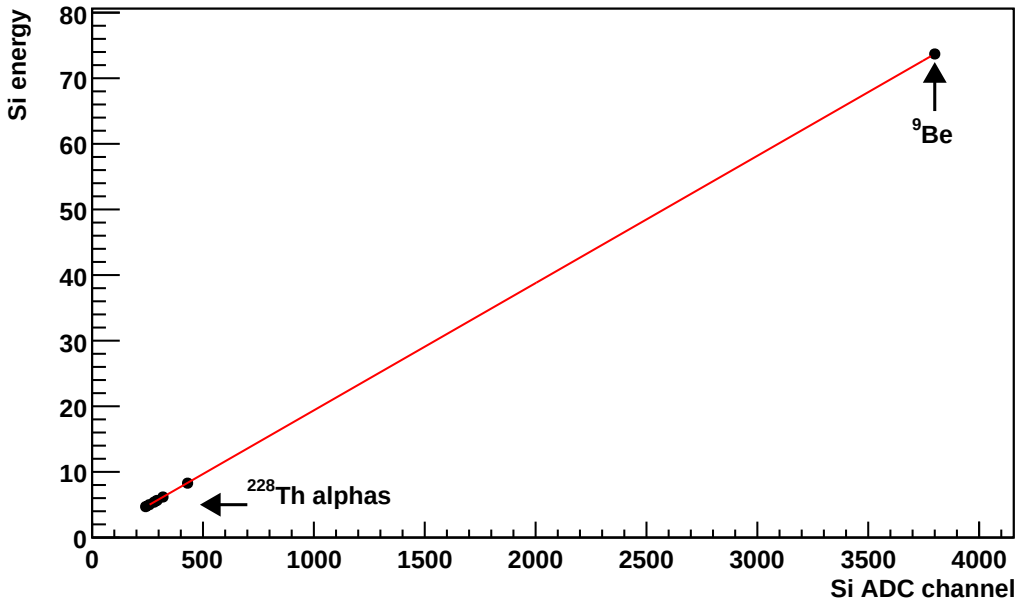

FIG. 12.: Si calibration energy vs. Si channel number. The data is represented by black points and the red line is the best fit straight line of the form $y = mx + b$.

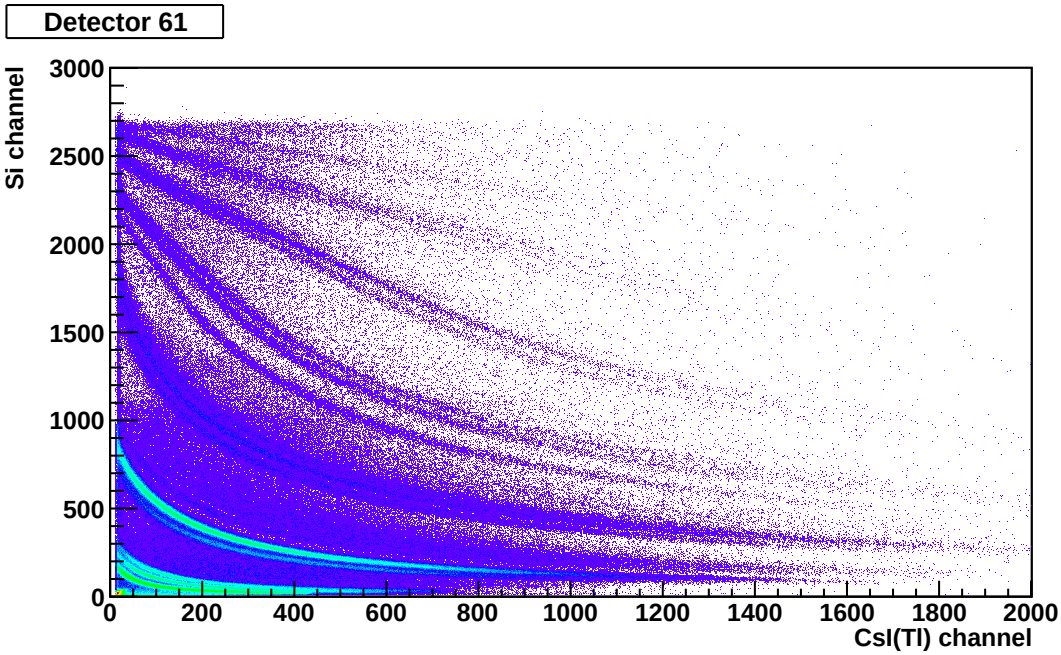

FIG. 13.: An example of a silicon saturated detector. As shown, the isotopic and elemental bands are seen to perform a 'back bending' behavior above Si channel 2000.

^{12}C, is graphed with the uncorrected silicon energy vs. actual energy from the Orsay tables and an exponential curve of the form

$$E_{Si,Orsay} = ce^{(a)(E_{Si,uncorr})} \tag{2.1}$$

is fit to the saturation data. Using the saturated and the unsaturated portions of the equation, the energy formula then becomes

$$E_{Si,corr} = E_{Si,uncorr} + ce^{(a)(E_{Si,uncorr})} \tag{2.2}$$

In equations 2.1 and 2.2 a & c are fitting parameters.

Equation 2.2 allows for very small, if any, corrections to be made at low silicon channel values, but allows for much larger corrections at the higher silicon channel values. To check the validity of the fit, a corrected energy versus the energy taken from the Orsay tables is plotted for detector 61 (Figure 14). The closed black points are the corrected experimental energy points, the open blue squares are the uncorrected experimental energy values, and the red line represents the best fit straight line through the corrected energy data. By looking at the fit and slope of this line we can determine the accuracy of this method. In an example case, the slope was found to be 1.0025 and the R^2 value is 0.999 which indicates an excellent fit.

2. Cesium Iodide Calibration

To calibrate a CsI(Tl) crystal it is necessary to find an expression that relates the light output given by the crystal, the energy of the incident particle, and the recorded channel number. There are many formalisms derived from the Birks formula

$$\frac{dL}{dx} = \frac{S(dE/dx)}{1 + [kB(dE/dx)]} \tag{2.3}$$

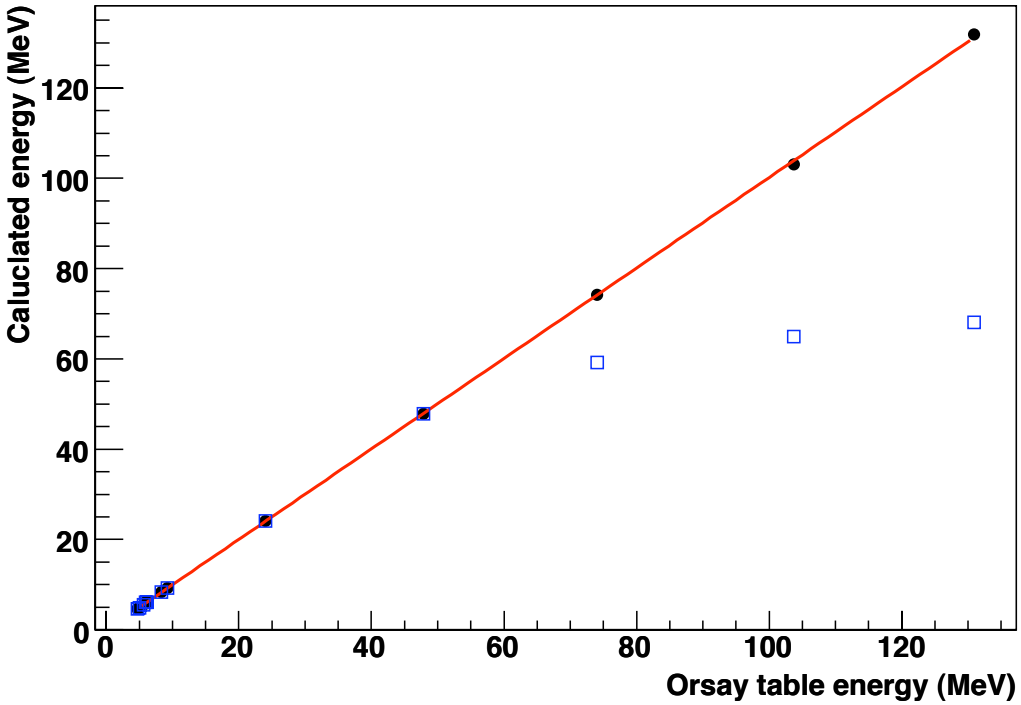

FIG. 14.: The comparison between the original calibration and the correction made to the saturated silicon detector 61. The closed black points are the corrected experimental energy points, the open blue squares are the uncorrected experimental energy values, and the red line represents the best fit straight line through the corrected energy data.

that relate the light output per unit length to the energy of a given particle [90–96]. In the Birks formula, equation 2.3, S is the scintillation efficiency and kB is the Birks constant. Due to the nature of the electronics we have a channel number which is proportional to the light output. It would be more convenient to find a method that relates the energy of the incident particle to the channel number. Methods derived from the Birks formula cannot be analytically inverted to relate $E = F(L, Z, A)$ where L is the light output, Z is the charge of the particle and A is the mass of the particle in question. It was found that by fitting a variety of data through the Birks equation, an equation that relates the energy as a function of light output, Z, and A was found [97]. This equation,

$$\epsilon = al + bln(1 + cl) \tag{2.4}$$

has 3 fitting parameters a, b, and c which are fit for each Z and A while l is related to the total light output. This form is not practical for multi-detector arrays which can identify many Z and A values and was generalized to

$$E(L, Z, A) = aAZ^2L + (b + cAZ^2)L^{1-d\sqrt{AZ^2}} \tag{2.5}$$

which includes dependencies on Z and A [98].

In Equation 2.5, L is related to the slow portion of the light output signal, A and Z are the mass and charge of the particle in question and $a - d$ are fitting constants. For the data presented in this work, this form could not be fit simultaneously over the entire Z range for $Z \leq 3$ while fitting $Z > 3$, therefore a modified equation for different Z ranges had to be explored and developed similar to reference [99]. For $Z > 3$ the incident energy is parameterized as a recast of the Larochelle equation shown in equation 2.5

$$E(L,Z,A) = aAZ^2L + b(1+cAZ^2)L^{1-d\sqrt{AZ^2}} \tag{2.6}$$

For Z = 2-3,

$$E(L,Z,A) = a\sqrt{AZ^2}L + b(1+cAZ^2)L^{1-d\sqrt{AZ^2}}. \tag{2.7}$$

In equations 2.6 and 2.7, L is the CsI(Tl) channel number recorded by the computer (this value is directly related to the slow portion of the light output signal), A and Z are the mass and charge of the particle in question and $a-d$ are fit parameters. Calibration for $Z = 1$ isotopes was done separately and will be discussed in a later section. In equations 2.5, 2.6, and 2.7 there is a linear term and a power term, both with AZ^2 dependence. The four fitting parameters, $a-d$, are allowed to vary but must remain positive. The parameters a, b, and c depend on the electronic gain and the scintillation efficiency. Parameter a effects the linear portion of the power term and is important for small Z and higher energies. Parameters b and c, which weight the power term, help account for low Z values and lower energies. Parameter d is responsible for the transition between the linear and non-linear portions of the equations [98]. Parameter L, in our case, will be the experimental channel number recorded, as the channel number is proportional to the slow portion of the light output signal.

To arrive at the parameters a-d, an n-line calibration method coupled to predictions from the Orsay tables was used. For each element used in a fit, the data from the Orsay tables was plotted as the energy deposited in the Si detector vs. Energy deposited in the CsI(Tl). To this graph, an equation with the form

$$E_{CsI} = \frac{c_1}{c_2 * E_{Si}} + c_3 \tag{2.8}$$

was fitted to the resulting curve. The values of c_1, c_2, and c_3 are fitting parameters. From this, for a given silicon energy (E_{Si}), the energy deposited in the CsI(Tl) (E_{CsI}) can be determined. From here, n-lines are drawn for a given range on the raw Si channel vs. CsI(Tl) channel spectrum (an example of this figure was given in Figure 11 . For $Z = 2 - 3$, lines were drawn on ^{4}He and ^{7}Li. For $Z > 3$, lines were drawn on ^{9}Be, ^{12}C, ^{14}N and the highest Z where a clear isotope line could be drawn. In some cases, the highest line drawn was ^{20}Ne. If possible, the beam spot was recorded as well. For each (x, y) channel point, the silicon channel was calibrated to give its corresponding energy value. This silicon energy value was then placed into equation 2.8 to obtain the corresponding Orsay CsI(Tl) energy value. This energy value is then compared to the picked CsI(Tl) channel value. A second curve of the CsI(Tl) energy is derived from equation 2.6 or equation 2.7 vs. picked CsI(Tl) channel number is constructed. Parameters $a - d$ are allowed to vary until the χ^2, which compares the fit between the two curves described above, is minimized. The χ^2 term is constructed by comparing the Orsay CsI(Tl) energy values to the CsI(Tl) calibration equation energy values.

Once the CsI(Tl) energy is found the total particle energy, E_{total}, is found by

$$E_{total} = E_{CsI} + E_{Si} + E_{mylar} \tag{2.9}$$

3. Calibration of $Z = 1$ Particles

Calibration of $Z = 1$ particles occurred separately from other particle types. This occurred as the energy deposited in the CsI(Tl) could not be defined over the entire energy range by any available method. However, the thickness of of the CsI(Tl) allows for $Z = 1$ particles to punch-through. The punch-through is defined as the point where a particle passes through the entire thickness of the CsI(Tl) and the

values of this point can be found in Table VII.

TABLE VII.: Z = 1 punch-through energy for the CsI(Tl).

Particle Type	Punch-through 3 cm (MeV)	Punch-through 2.26 cm (MeV)
proton	95	81
deuteron	130	110
triton	153	130.5

All detector telescopes exhibit punch-through behavior for $Z = 1$ particles. In addition to this punch-through value, the punch-in value can be determined as well. This punch-in value is defined as the point where the particle of interest passes through the silicon detector and first deposits into the CsI(Tl). With both the punch-in and punch-through values, the spectrum was scaled to match these points. Scaling involved two processes, a shift and a stretch. The shift allows, for example, points that go from 0 -100 to then go from 50 - 150 without changing the range or the shape. A stretch involves, for example, points that go from 0 - 100 to result in points that go from 0 -200, in effect elongating the shape. To accomplish this, the following equations were used.

$$y = mx + b \tag{2.10}$$

where

$$m = \frac{\text{shift destination} - \text{stretch destination}}{\text{shift point} - \text{stretch point}}$$

$$b = \text{shift destination} - m * \text{shift point}$$

In equation 2.10, the shift point is defined as the point where you want a shift to start and shift destination is where you want the shift point to end. The stretch point is the point where you would like a stretch to begin and the stretch destination is where the stretch is to end.

4. Final Energy Spectra

Once the particle identification and energy calibration occurs the final energy spectra can be generated. For the final energy spectra a lower and upper energy threshold is placed on each isotope in each detector. These thresholds are to remove extraneous noise and ADC pedestals. After calibration and the threshold cuts the particle Z, A, detector hit, and Energy are recorded in a physics tape. Example energy spectra of the detectors at 20.06° are given for protons, ^{4}He, and ^{12}C in Figures 15, 16, and 17 respectively. These energy spectra are normalized to the area under the curve. A feature seen in the ^{12}C spectra, is that detector 38 and 40 start at a lower energy than the rest of the detectors at 20.06°. This is due to the fact that the gain on the silicon detector amplifier was set to lower values for detector 38 and 40. In return this allowed for the entire carbon energy spectra to be recorded. In the other detectors at 20.06°, the higher gain prevented the entire energy spectra being recorded by the computer and only the higher energy values are obtained.

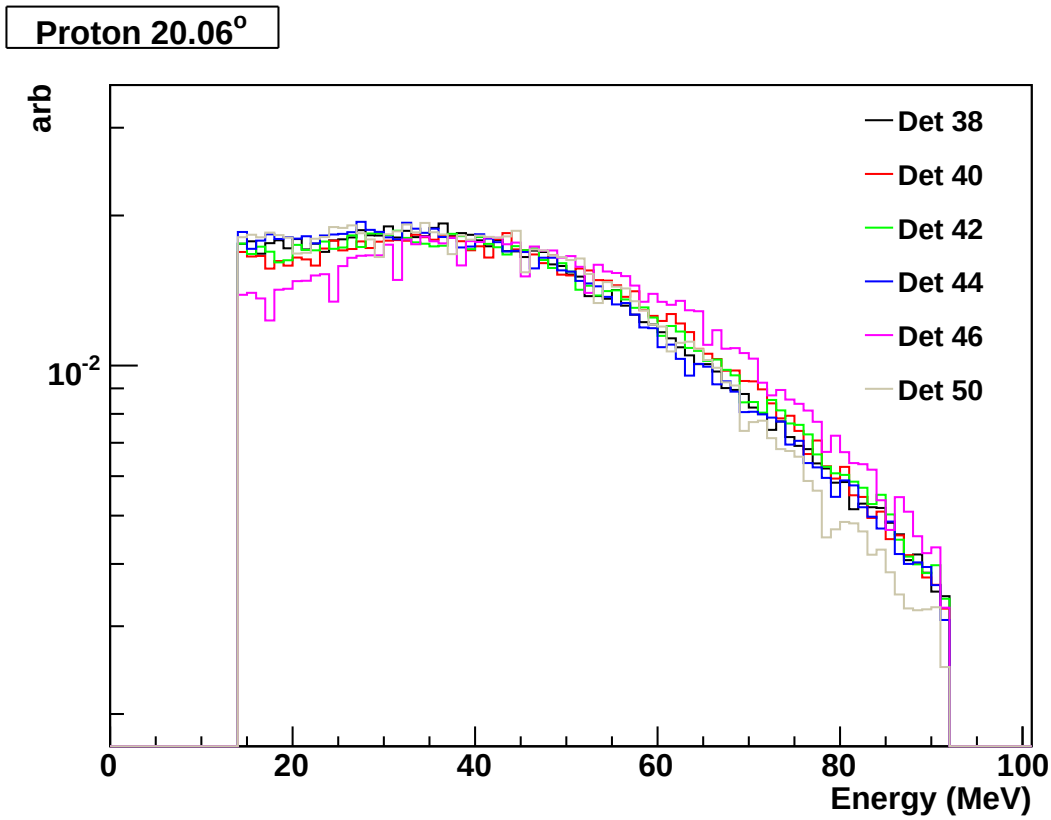

FIG. 15.: Energy spectra for protons at 20.06°. These spectra have been normalized to the area under the curve.

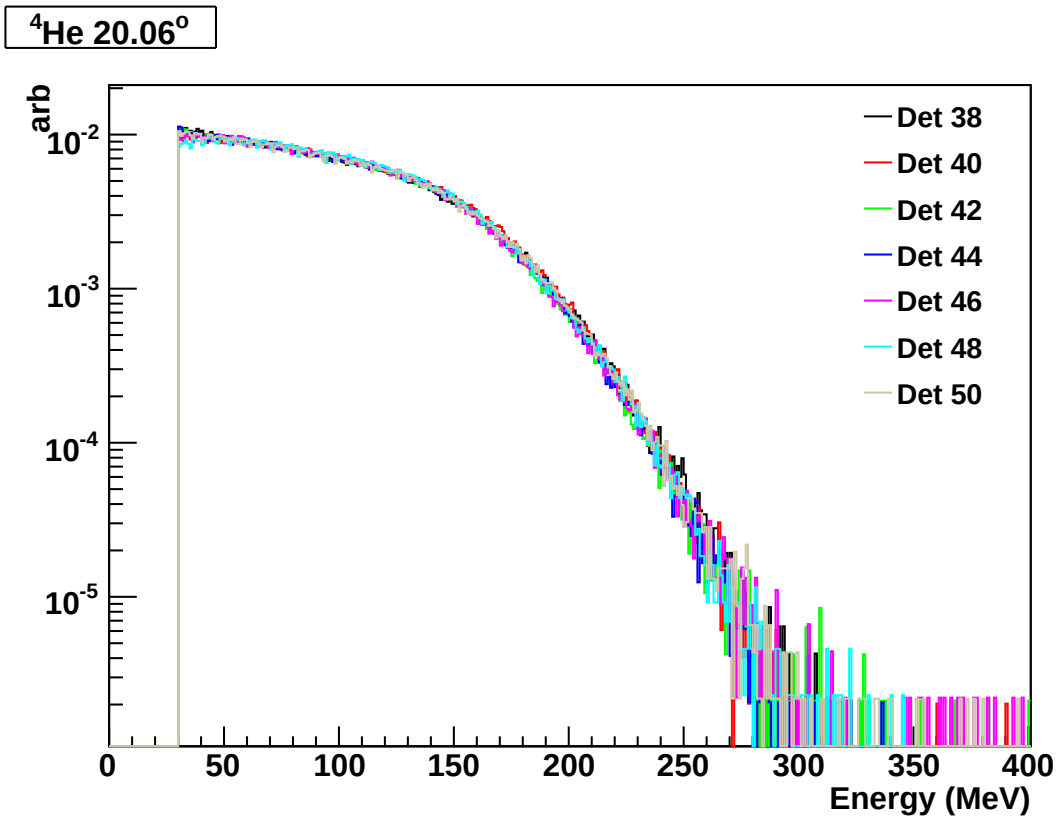

FIG. 16.: Energy spectra for ^{4}He at 20.06°. These spectra have been normalized to the area under the curve.

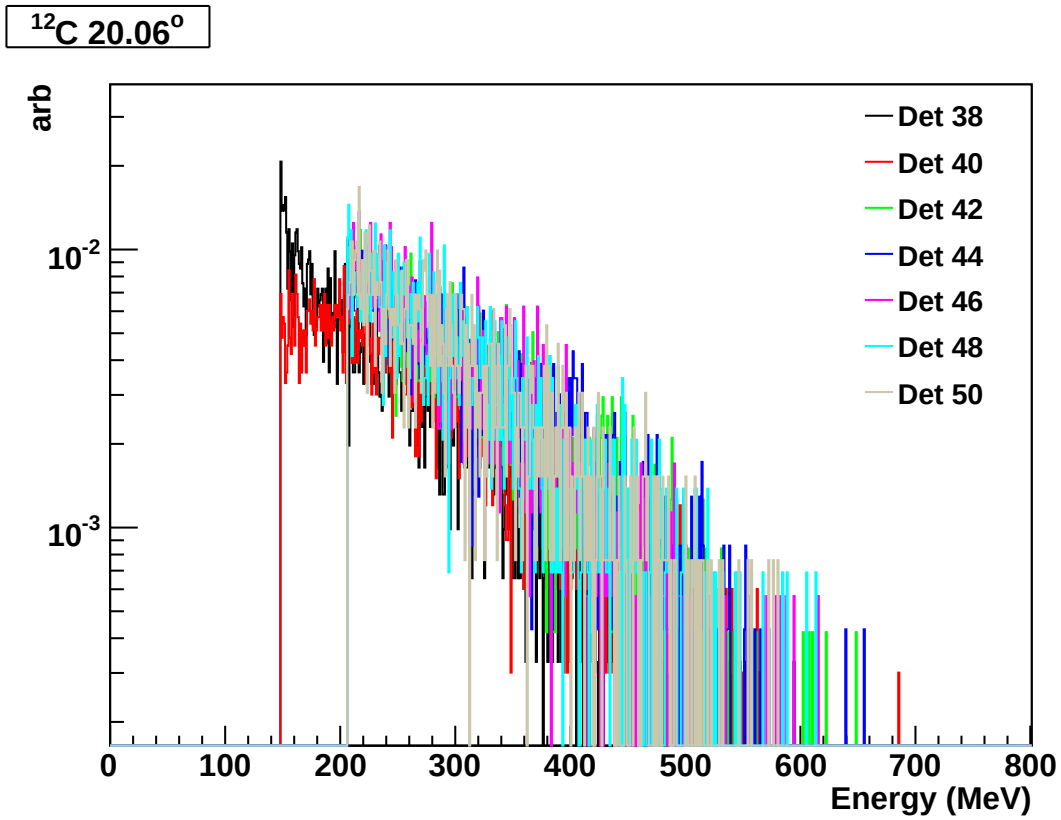

FIG. 17.: Energy spectra for ^{12}C at 20.06°. These spectra have been normalized to the area under the curve. The discrepancy in the lower energy portion of the spectrum for Det 38 and Det 40 is due to the fact that the gain was set such that the entire energy range was captured. This was not true for the rest of the detectors at this angle.

CHAPTER III

SOURCE DEFINITION AND EVENT RECONSTRUCTION

To study decay modes of nuclei, it is particularly important to have a well defined source. It is important for this study to have well defined projectile-like, or quasi-projectile, source. To do this, an event reconstruction is necessary on an event-by-event basis. Because of the detector thresholds discussed in the previous chapter, low energy particles are not detected. Many of these low energy particles originate from target-like and mid-velocity sources. However, it is still important to ensure that the particles detected come from a projectile-like or quasi-projectile source. The essential requirement in selecting a quasi-projectile source is that the summed charge of the fragments detected equals that of the beam (Eq. 3.1). This requirement has been shown in previously [100, 101] to be an excellent method of defining a quasi-projectile source within the FAUST array.

$$\Sigma Z_{frag} = Z_{beam}. \tag{3.1}$$

This requirement is broad in comparison to previous studies [4, 102], however, it is appropriate as FAUST has higher thresholds due to the use of silicon as the first detector in the detector telescope. Even though previous works show that this cut is appropriate in isolating quasi-projectile sources [100], this study requires that the mass of the particles in an event be known, therefore, it is required that all fragments in an event be isotopically identified. In addition it was chosen to use only events where the Z of all fragments was ≤ 8. This choice was made due to the incomplete coverage for heavier elements within FAUST. Additionally, this allows for a preferential selection of multifragmentation events.

The first observable examines the reconstructed velocity of the source. A projectile-

like source should retain a velocity similar to the velocity of the beam. Figure 18 shows the velocity of the reconstructed quasi-projectile. The blue line represents the beam velocity, 0.31c. As shown, the peak in the velocity distribution is slightly lower than that of the beam velocity indicating that the source selection is projectile-like. Contamination from particles from target or mid-velocity sources would populate a low velocity tail. As the shape of the curve is sharply peaked with no low or high velocity tails and is fairly symmetric, it is concluded that there is no large contamination component from pre-equilibrium, mid-velocity or target sources.

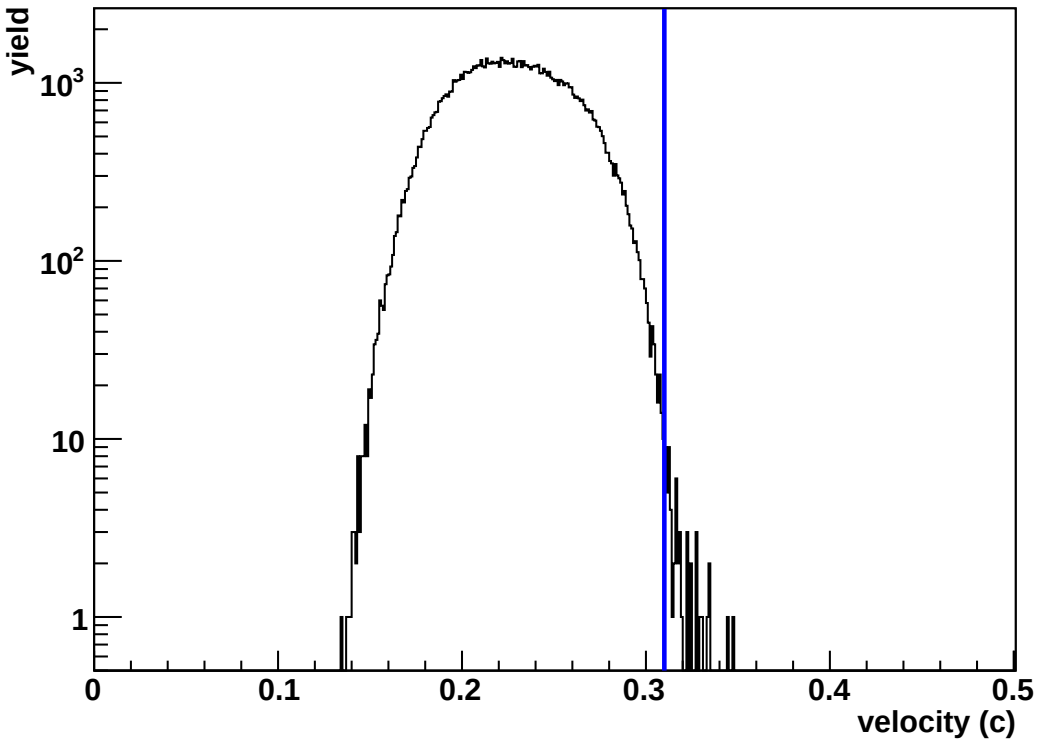

FIG. 18.: The velocity in units c of the quasi-projectile. The blue line represents the beam velocity on 0.31c.

The second observable to confirm that a clean source is obtained is a parallel ve-

locity (v_{par}) vs. perpendicular velocity (v_{perp}) plot. The velocity of each fragment was transformed to the center-of-mass of the quasi-projectile. In this frame, the center-of-mass coordinate system was rotated such that the parallel vector direction (z-axis) coincides with the vector direction of the quasi-projectile. A graphical representation of this frame is presented in Figure 19. Looking at the v_{par} vs. v_{perp} for $Z = 1$, $Z = 2$, and $Z > 3$ in this rotated, quasi-projectile frame can provide information about the emitting source. Figure 20 shows the parallel velocity vs. perpendicular velocity for $Z = 2$ in the left panel and $Z > 3$ in the right panel in the rotated, quasi-projectile frame. In both of these cases, the quasi-projecile source is isolated in space and by the circular shape, is emitting isotropically. If multiple sources were present one would possibly see a second round shape to the left of the PLS representing the target-like source (TLS); this is not present. If mid-velocity or neck emission were present the particles attributed to this region would appear to the left of the PLS shown and "connect" to a TLS if one were present.

For $Z = 1$ particles, the v_{par} vs. v_{perp} for each isotope is shown in Figure 21. As shown, the $Z = 1$ isotopes do not show the same symmetry as those found in Figure 20. There is a symmetric, central concentration, but a non-symmetric component appearing to emit in the forward direction of lesser intensity. Because of the forward peaking dramatically seen in the proton v_{par} vs. v_{perp} plot in the left pane of Figure 21 and to a lesser extent in the deuteron v_{par} vs. v_{perp} there is a concern that there is pre-equilibrium emission contaminating the quasi-projectile source. However, because FAUST has shallow CsI(Tl) crystals in all rings there is a high energy punch-through value for $Z = 1$ particles(see Table VII for values). This high energy punch-through affects the appearance of the V_{par} vs. v_{perp} plot.

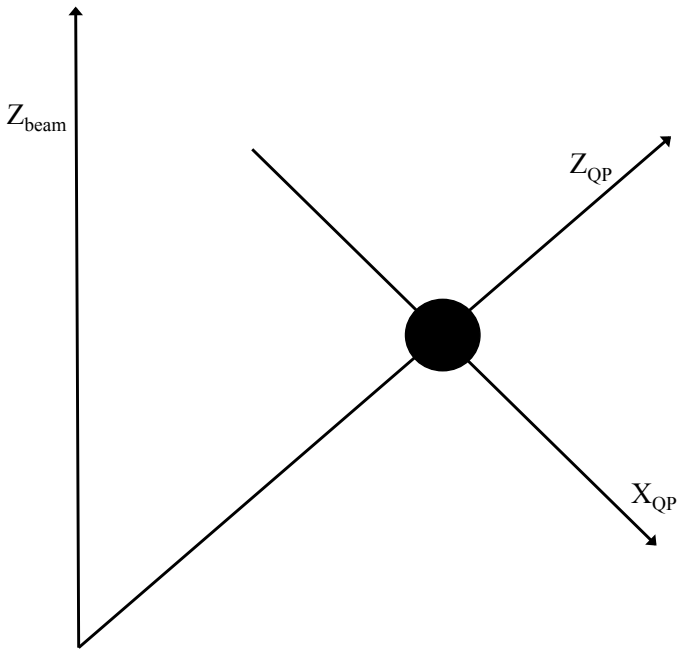

FIG. 19.: A graphical representation of the rotated center-of-mass, or quasi-projectile, coordinate system. The frame is rotated such that the parallel vector direction (z-axis) coincides with the vector direction of the quasi-projectile.

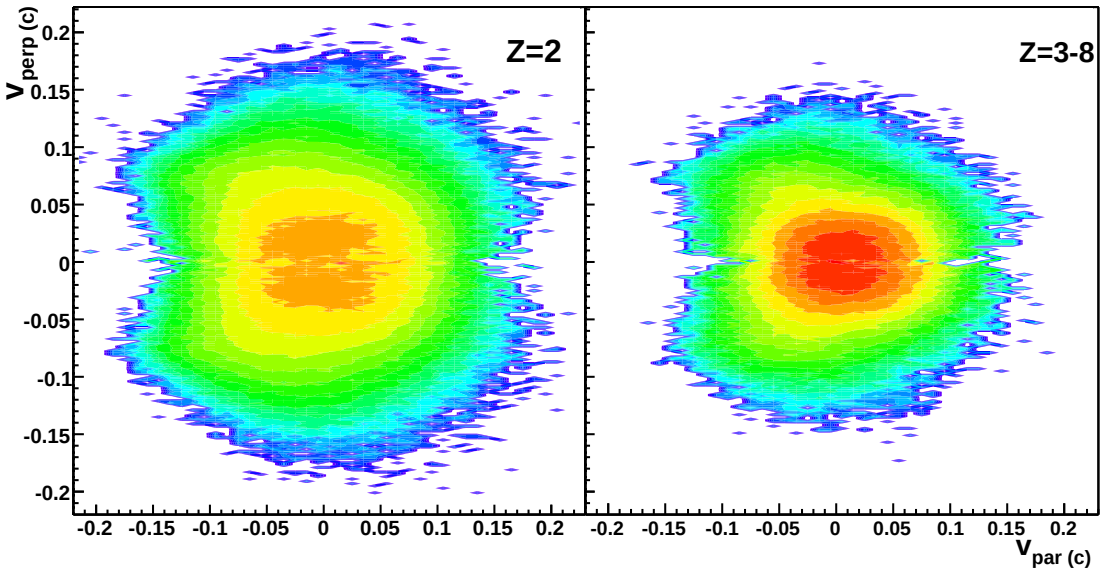

FIG. 20.: Left panel: A v_{par} vs. v_{perp} plot for $Z = 2$ atoms. As shown, the figure is fairly spherical indicating that the source emitting these particles is emitting isotropically and by the shape being fairly isolated, the source is isolated in space. Right panel: A v_{par} vs. v_{perp} plot for $Z = 3 - 8$ atoms. As shown the figure is spherical which indicates that the source is emitting particles isotropically and by the shape being fairly isolated, the source is isolated in space.

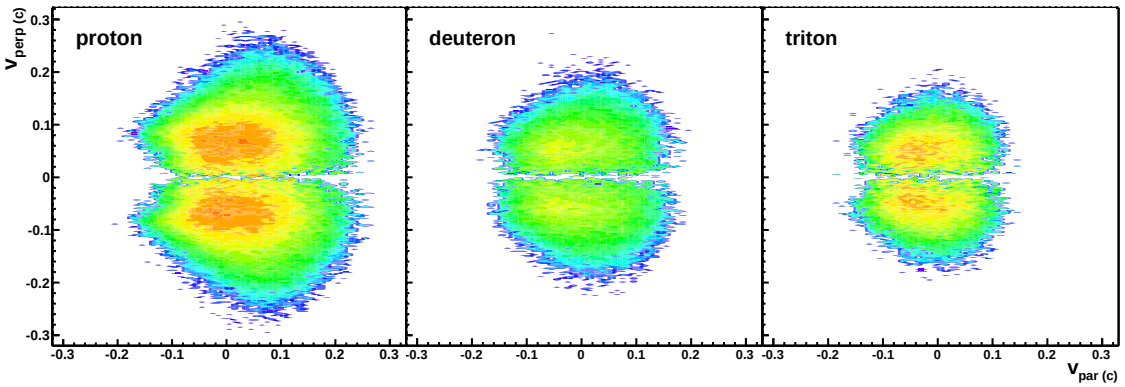

FIG. 21.: Left panel: The v_{par} vs. v_{perp} plot for protons. Middle panel: the v_{par} vs. v_{perp} plot for deuterons. Right panel: The v_{par} vs. v_{perp} plot for tritons.

Using the laboratory frame is an easy way to examine the punch-through of the CsI(Tl) effect on the $Z = 1$ particles. Figure 22 shows the effect on placing an energy cut on the protons. The energy chosen was 81 MeV which corresponds to the energy punch-through of the shortest CsI(Tl). When there is no proton energy cut, the parallel velocity extends to slightly higher values than when the proton energy cut is placed. This is more evident in the laboratory frame (top row of Figure 22) than for those in the quasi-projectile frame (bottom row of Figure 22). This shows that the different energy punch-through values are playing a part in the elongation of shape of the v_{par} vs. v_{perp} plots. The hard diagonal cut off seen is a consequence of the detector geometry.

Looking at the v_{par} of the source in the quasi-projectile (QP) frame directly as in Figure 23, the effect of the proton energy cut can be seen more clearly. As shown, the left panel is the proton v_{par} , the middle panel is the proton v_{par} with the energy cut of 81 MeV applied, and the right panel is the two overlaid where the red curve represents the proton v_{par} with the 81 MeV energy cut applied. As one can see, the v_{par} with the energy cut applied deviates at the high v_{par} values. This difference is directly due to the energy difference in the punch-through values. The effects that this punch-through should be minimal as it only affects the $Z = 1$ isotopes and at maximum, only imparts ≈ 0.5 MeV total to the source excitation energy.

A third way to characterize the source is using a Dalitz plot [103]. Using a Dalitz plot, it is possible to determine how particles are moving in space. From the shape of the Dalitz plot, how equilibrated, on average, a source is. One defines the following coordinates in a Cartesian frame [104]:

$$x = \frac{(\lambda_2 - \lambda_3)}{\sqrt{3}} \tag{3.2}$$

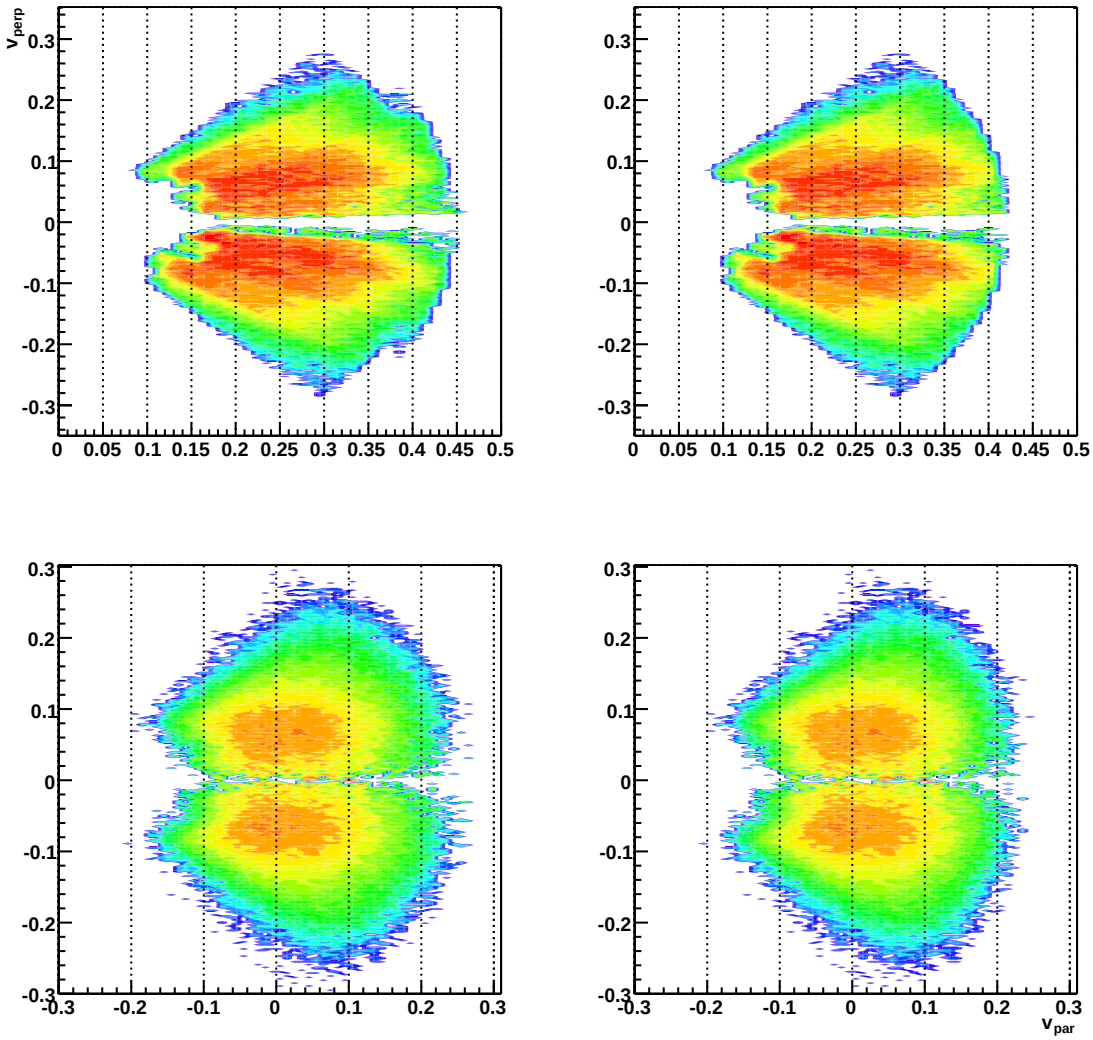

FIG. 22.: Top left: The v_{par} vs. v_{perp} plot for protons in the laboratory frame. Top right: The v_{par} vs. v_{perp} plot for protons with an energy cut for protons that excludes those that are higher than 81 MeV in energy. Bottom left: same as top left but in the quasi-projectile frame. Bottom right: Same as top right but in the quasi-projectile frame.

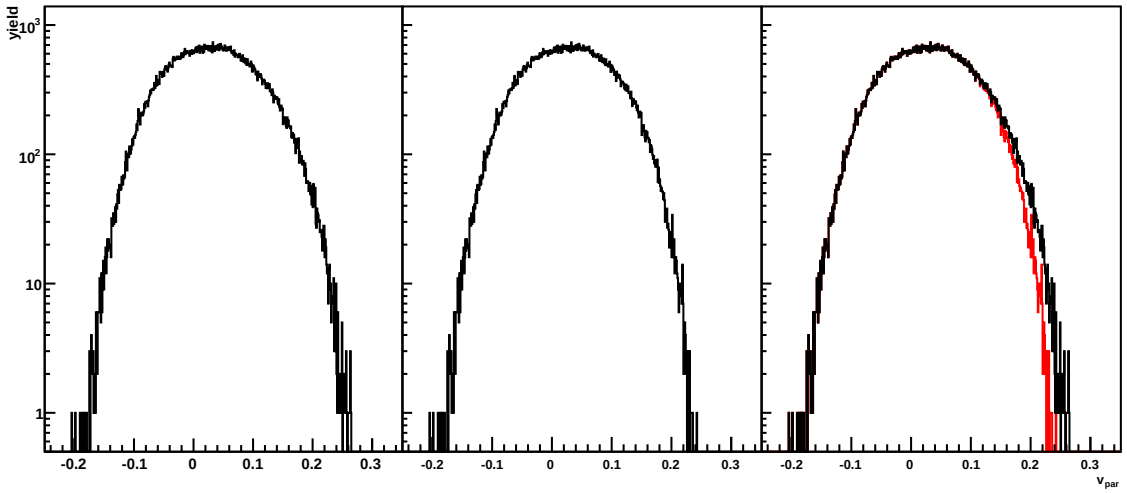

FIG. 23.: Left panel: The v_{par} plot for protons in the quasi-projectile frame. Middle panel: The v_{par} lot for for protons in the quasi-projectile frame with an upper energy threshold of 81 MeV applied. Right panel: An overlay of the previous two plot highlighting the effect of the different depths of the CsI(Tl) crystal. The black line represents the parallel velocity of protons with no energy cut while the red curve represents the parallel velocity where the 81 MeV energy cut has been placed on the data.

$$y = \lambda_1 - \frac{1}{3}(\lambda_1 + \lambda_2 + \lambda_3)$$

where

$$\lambda_1 = \mathbf{P}_z$$

$$\lambda_2 = \mathbf{P}_x$$

$$\lambda_3 = \mathbf{P}_y$$

for a momentum derived Dalitz plot. Using this method the y-axis represents the momentum in the Z-direction, negative x-values correspond to momentum in the Y-direction, and positive x-values correspond to momentum in the X-direction. Figure 24 shows a round, isolated source, centered about zero, which is generated from the above method showing a symmetric momentum splitting. It is generally accepted that an equilibrated source will, on average, emit particles isotropically, therefore, the round isolated source depicted in Figure 24 is consistent with a fairly equilibrated quasi-projectile source.

In conclusion, an excellent definition of a source is when the sum of the collected charge is equal to that of the beam, all fragments must be isotopically identified, and the event contains only $Z = 1 - 8$ fragments. It is well isolated in space and has minimal contamination from target and mid-velocity sources. Also the source is emitting fairly isotropically as seen from the momentum derived Dalitz plot as well as the particle v_{par} vs. v_{perp} plots. This defined source will be the basis for the further analysis of this work.

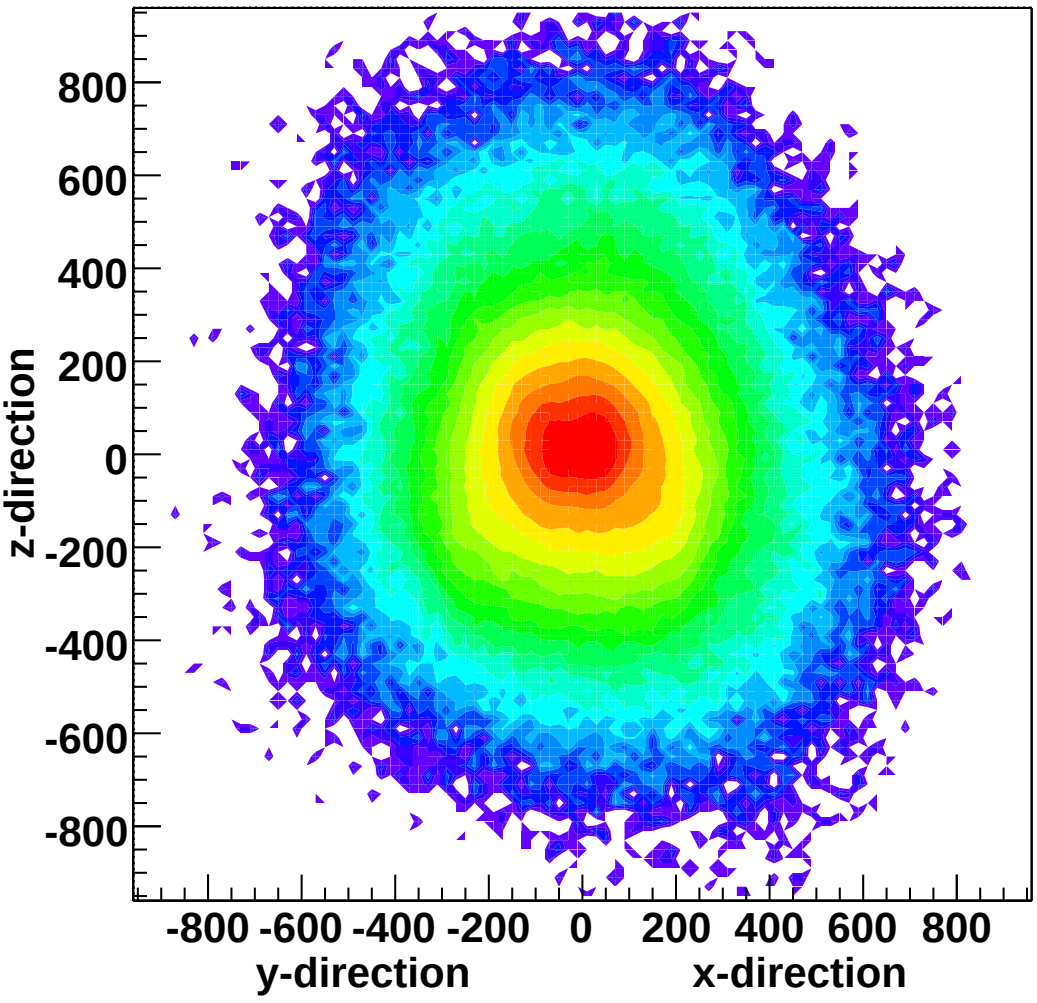

FIG. 24.: A momentum derived Dalitz plot. As shown, the plot is round and isolated indicating that the momentum is symmetrically splitting as would be seen by an average equilibrated source.

CHAPTER IV

THEORETICAL MODELS AND THE FAUST FILTER

The calculations in this dissertation are based on a two-staged Monte Carlo approach. The dynamical, interaction stage of the collision is described by the deep-inelastic transfer (DIT) code which simulates stochastic nucleon exchange in peripheral and semi-peripheral collisions. This nucleon exchange is allowed to happen because an interaction window, defined by the potential barriers of the nuclei, is opened as the projectile and target begin to interact [10]. The transfer of nucleons in the nuclear mean field of the projectile-target system can effectively describe the transport of charge, mass, linear and angular momentum, and the energy [46, 105]. These conclusions by Randrup arose from experiments in the late 1970's that showed that damped nuclear collisions at low energies, just below the Fermi energy domain, showed a binary character and the composition of the projectile and target remained relatively unchanged [106]. DIT produces a hot nuclear system which then needs to expand and break-up into fragments.

The statistical multifragmentation model (SMM) is the model chosen to expand and break-up the hot nuclear system created by DIT. SMM is based upon the assumption that a statistical equilibrium exists between the produced fragments in a low-density freeze-out volume [37]. All breakup channels, or partitions, are composed of nucleons, excited fragments are considered, and the conservation of mass, charge, momentum, and energy are taken into account. The formation of a compound nucleus is included as one of the channels. This inclusion allows for a smooth transition from evaporation and fission decays at low excitation energies [107] to multifragmentation at high excitation energies. The system is allowed to expand to a defined freeze-out volume and then the breakup occurs. Once the breakup occurs, the fragments are

allowed to propagate independently in their mutual Coulomb field and are allowed to undergo secondary decays. The de-excitation of the hot primary fragments proceeds via evaporation, fission or Fermi-breakup [108].

The version of SMM used in this dissertation [109] is based on generating a Markov chain of partitions which is representative of the whole partition ensemble. Individual partitions are generated and selected into a chain by applying the Metropolis algorithm and taking into account that fragments with the same mass, A, and charge, Z, are indistinguishable. This method is highly efficient and as a result the Coulomb interaction energy for each spatial configuration of primary fragments at break-up can be directly calculated. Influence of the target Coulomb energy on multifragmentation of the projectile can also be taken into account. It is believed that for relatively small systems the Markov-chain SMM is a better choice for analysis of the nuclear multifragmentation data concerning the isospin degree of freedom, where an angular momentum may be important. In addition to the details found in Reference [109], the liquid drop parameters have been smoothed to help with the evaporation in the low excitation energy region and the Fermi break-up also has been adjusted to allow for better mass distributions, i.e. larger widths of masses are being populated [110] to better represent the experimental data.

Before investigating the data for specifics of multifragmentation, the analysis of more basic observables will show that the DIT model combined with the SMM decay code gives a reasonable description of the experimental data. The experimental excitation energy for the isotopically identified quasi-projectile (QP) source is shown in Figure 25. This figure shows a two dimensional representation of the excitation energy calculated by DIT versus the reconstructed excitation energy derived from SMM on an event by event basis for isotopically identified QPs from unfiltered theoretical data. The black straight line is representative of an $x = y$ line. While the trend between

the input excitation energy and the reconstructed excitation energy is linear, there is a slightly lower value for the reconstructed energy coming from SMM when compared to the DIT E* for the event. This is due to other methods of energy dissipation such as internal excitation energy that is unaccounted for in the de-excitation process.

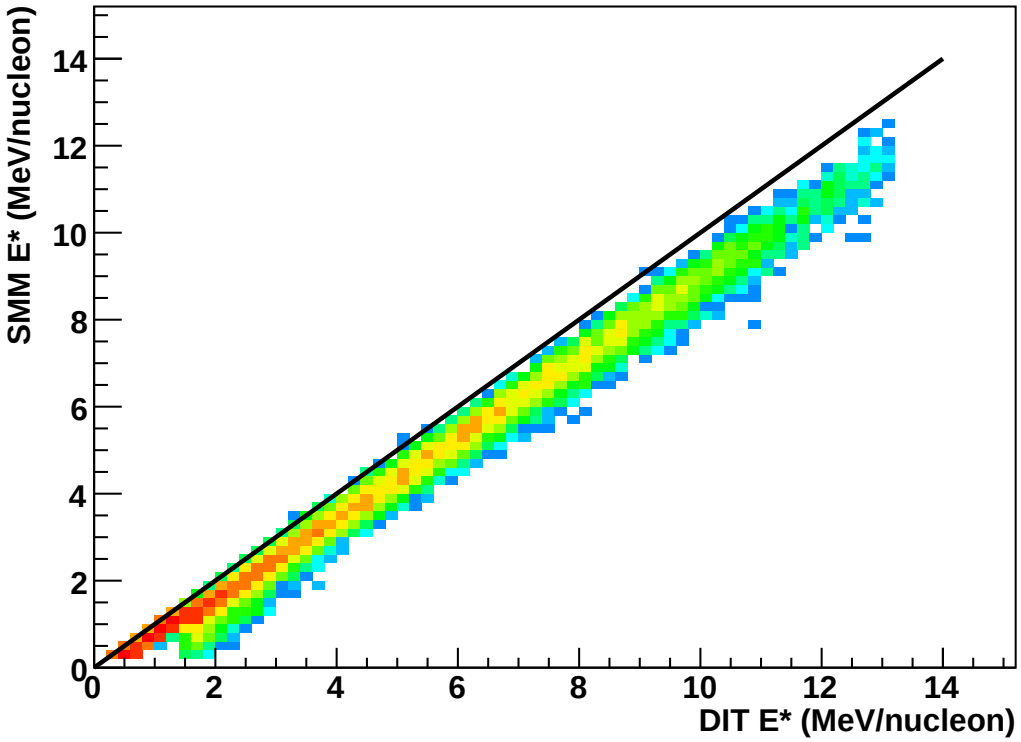

FIG. 25.: A two dimensional representation of the excitation energy calculated by DIT versus the reconstructed excitation energy from SMM on an event by event basis for isotopically identified QPs for unfiltered theoretical data. The black straight line is representative of an $x = y$ line.

When comparing in Figure 26 the one dimensional spectra for the DIT excitation energy to the reconstructed SMM excitation energy for unfiltered theoretical data, there is good agreement in magnitude and shape. A small deviation occurs at high

excitation energies.

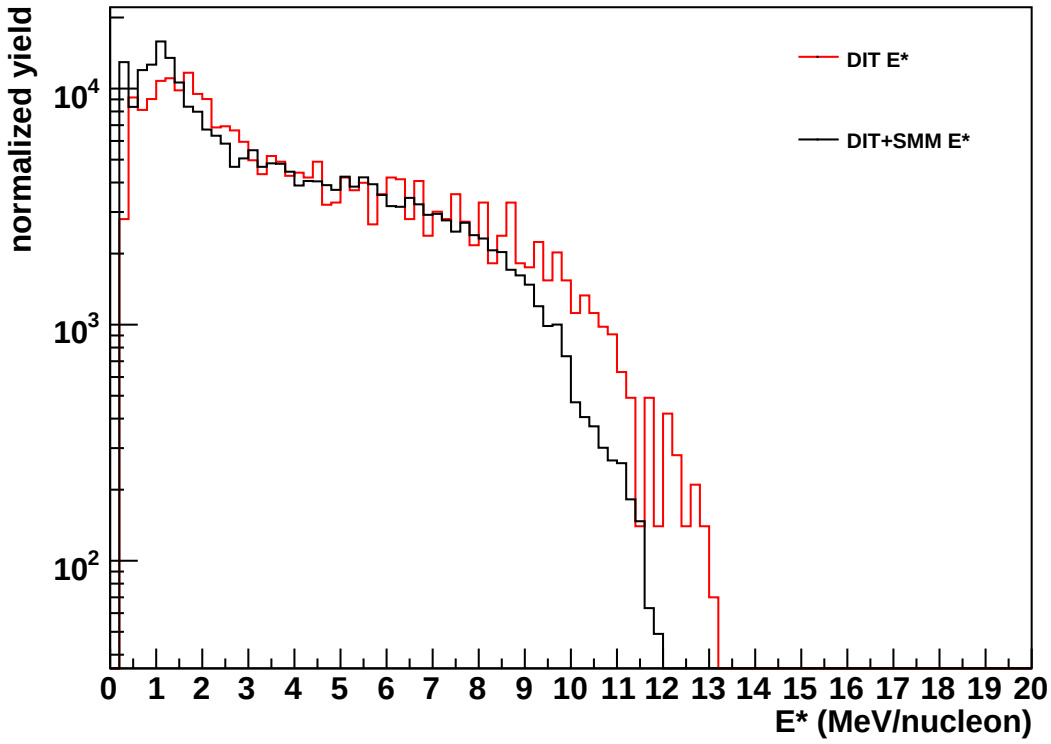

FIG. 26.: A comparison of the DIT excitation energy (red) to the reconstructed excitation energy for unfiltered theoretical data (black).

To compare with experimental data, the simulated data was ran through a software representation of the FAUST array. The FAUST filter takes into account the geometry of the FAUST array, the energy thresholds of each element and isotope by detector telescope, as well as the elemental and isotopic identification by detector telescope as determined by experimental data. The theoretical data does not have any type of isotopic confidence cut like the experimental data, since the isotopic identity is known from the calculation. However, if an entire element in the experiment is tagged as negative, for a detector telescope the FAUST filter flags those elements

from the theoretical calculation as having a negative mass. Filtering the theoretical data allows the DIT+SMM theoretical calculation to be seen and processed the exact same way as the experimental data.

Once the DIT+SMM theoretical calculation has been filtered comparisons to the experimental data can be made. Figure 27 compares the reconstructed excitation energy from the theoretical calculation to the experimental data for the isotopically reconstructed QP for the system ^{32}S + ^{112}Sn at 45 MeV/nucleon. As shown, the DIT+SMM does a decent job in matching the experimental data. The DIT+SMM produces an excitation energy spectrum that is similar in shape to the experimental data. However, the theoretical calculation produces more low energy events than the experimental data. The E* for the theoretical calculation is, on average, lower than the experimental data. The high energy tails have similar slopes but the theoretical calculation has a slightly lower production within this region.

As the multifragmentation channel dominates at excitation energies above $3-4$ MeV/nucleon, the excitation energy spectrum that matches fairly well. By normalizing the comparison between the DIT+SMM calculation and the experimental data for the system ^{32}S + ^{112}Sn to the region above 4 MeV/nucleon, Figure 28 is constructed. As shown, the low energy region does not match well, but the multifragmentation region, predicted by DIT+SMM, matches quite well.

The experimental charged particle multiplicity (M_{cp}), for isotopically identified events in shown in Figure 29. The spectra are normalized to the total yield. This shows that the theoretical data does not reproduce the experimental data in the low multiplicity region. This is not unexpected as SMM is known to not reproduce evaporation and fission mechanisms well which dominate at low excitation energies which generally produce low multiplicity events.

When placing the energy cut indicative of where multifragmentation becomes

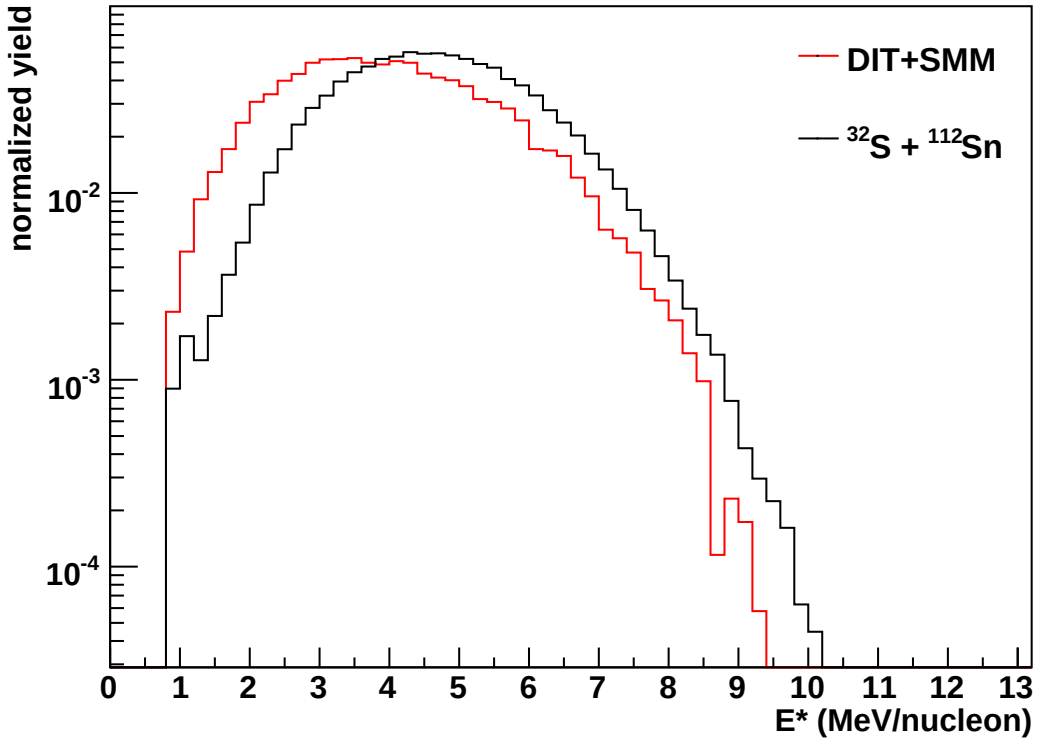

FIG. 27.: The comparison of the reconstructed excitation energy from DIT + SMM (red) to the experimental data for the system ^{32}S + ^{112}Sn at 45 MeV/nucleon (black). The spectra are normalized to the area under the curve.

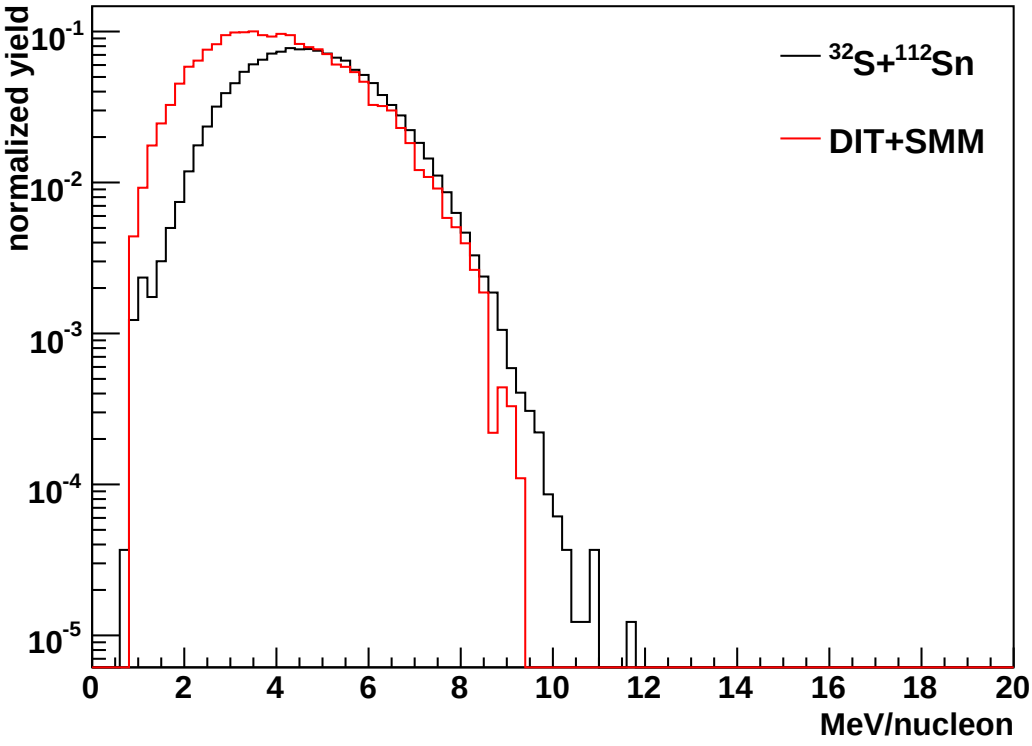

FIG. 28.: The comparison of the reconstructed excitation energy from DIT + SMM (red) to the experimental data for the system ^{32}S + ^{112}Sn at 45 MeV/nucleon (black). The spectra are normalized to the area under the curve where E* > 4 MeV/nucleon.

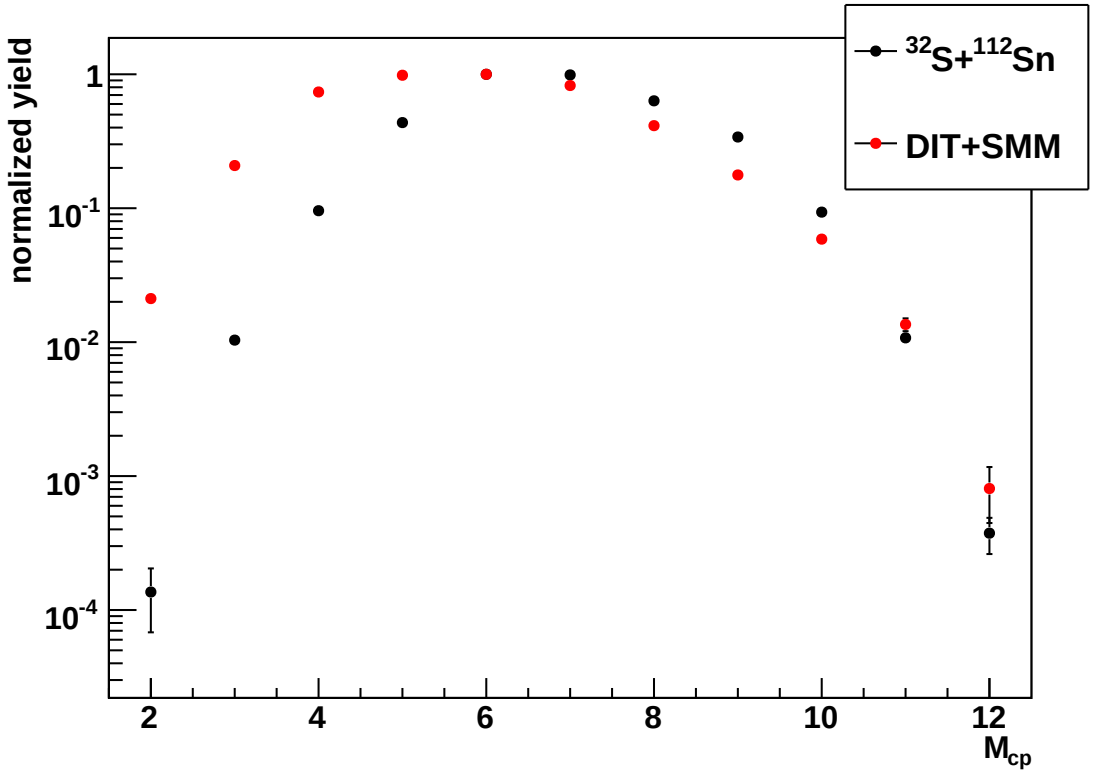

FIG. 29.: The charged particle multiplicity, M_{cp}, for the isotopically defined quasi-projectile source.

the dominant decay mechanism of E* > 4 MeV/nucleon, Figure 29 becomes Figure 30. Each spectra in Figure 30 is normalized to the total yield. Once the energy cut is placed on both the theoretical calculation and the experimental data they produce very similar multiplicity distributions. Again, this suggests that the experimental data is primarily undergoing multifragmentation within this energy region.

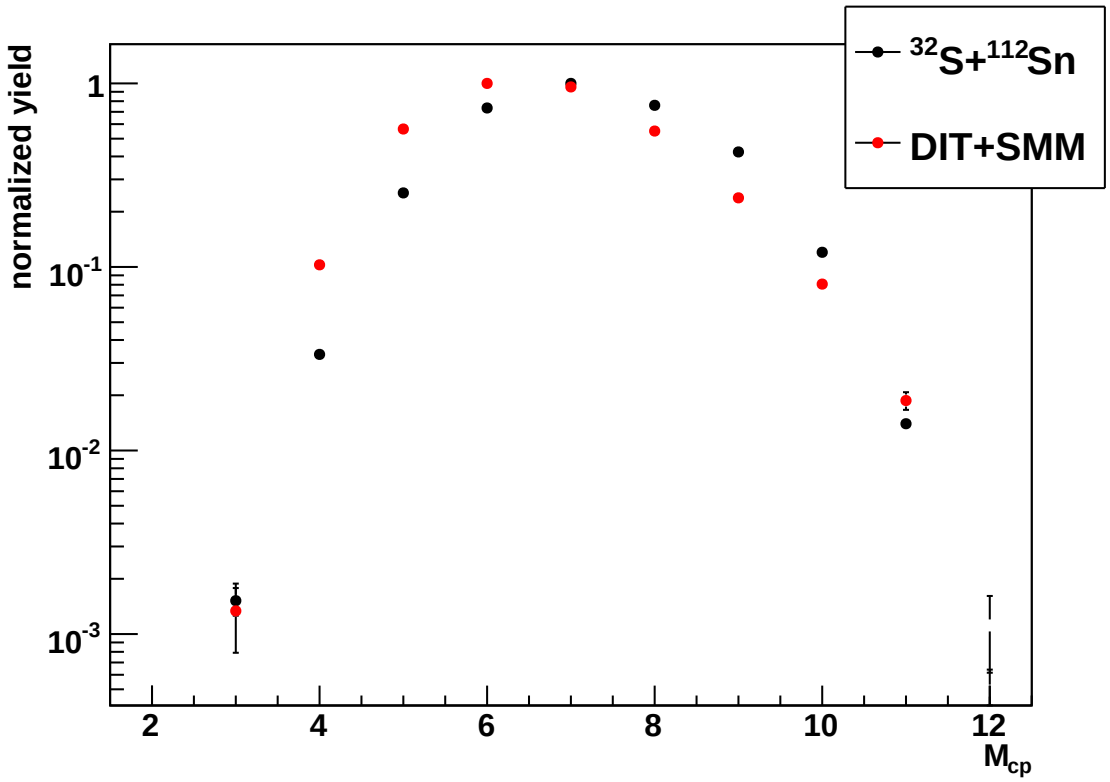

FIG. 30.: The charged particle multiplicity, M_{cp}, for the isotopically defined quasi-projectile source with an energy cut for events greater than 4 MeV/nucleon.

Another basic observable is the width of the source N/Z distribution of the ^{32}S + ^{112}Sn at 45 MeV/nucleon system. Figure 31 presents the QP N/Z distribution for all excitation energies. Both the experimental and theoretical data are normalized to the total number of quasi-projectiles produced. As shown the experimental

distribution is wider than the DIT+SMM theoretical calculation. This is due to the experimental data producing more neutron-rich sources than predicted theoretically. It is interesting to note that production of neutron-poor sources is similar between the experimental data and the theoretical calculations. When placing the E* > 4 MeV/nucleon on the system and looking at the N/Z ratio again one arrives at Figure 32. This figure shows that the experimental data still produces more neutron-rich sources than the theoretical calculation. Again the neutron-poor sources have reasonable agreement.

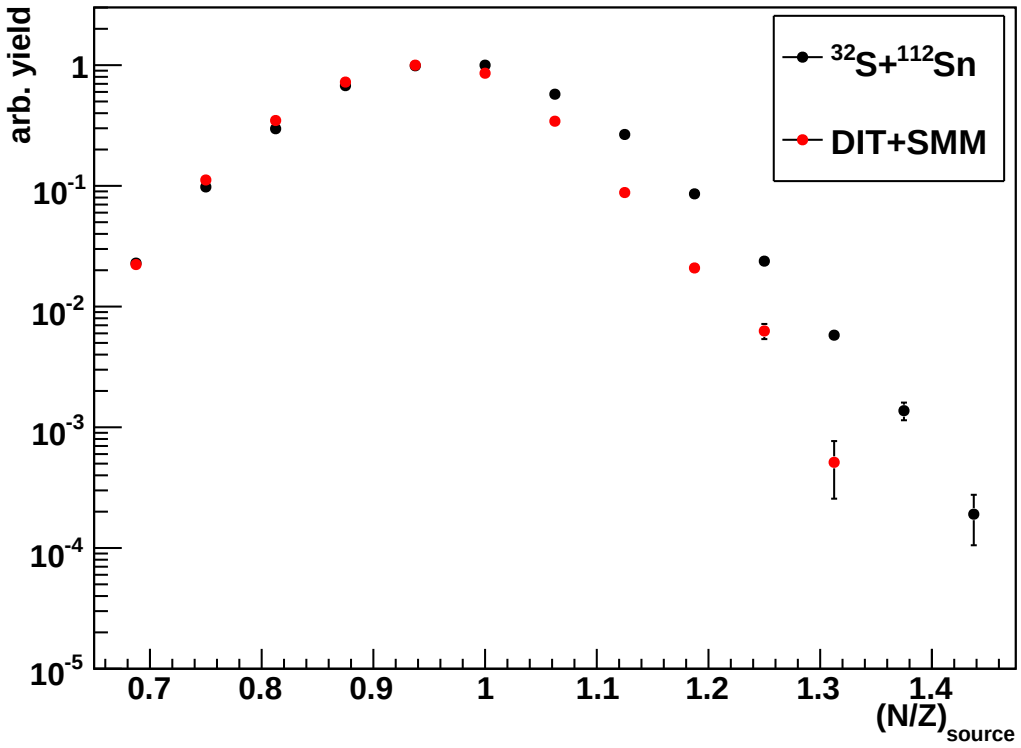

FIG. 31.: The QP N/Z distribution for the ^{32}S + ^{112}Sn at 45 MeV/nucleon system. As shown the experimental distribution (black) has a wider distribution than the DIT+SMM theoretical calculation (red).

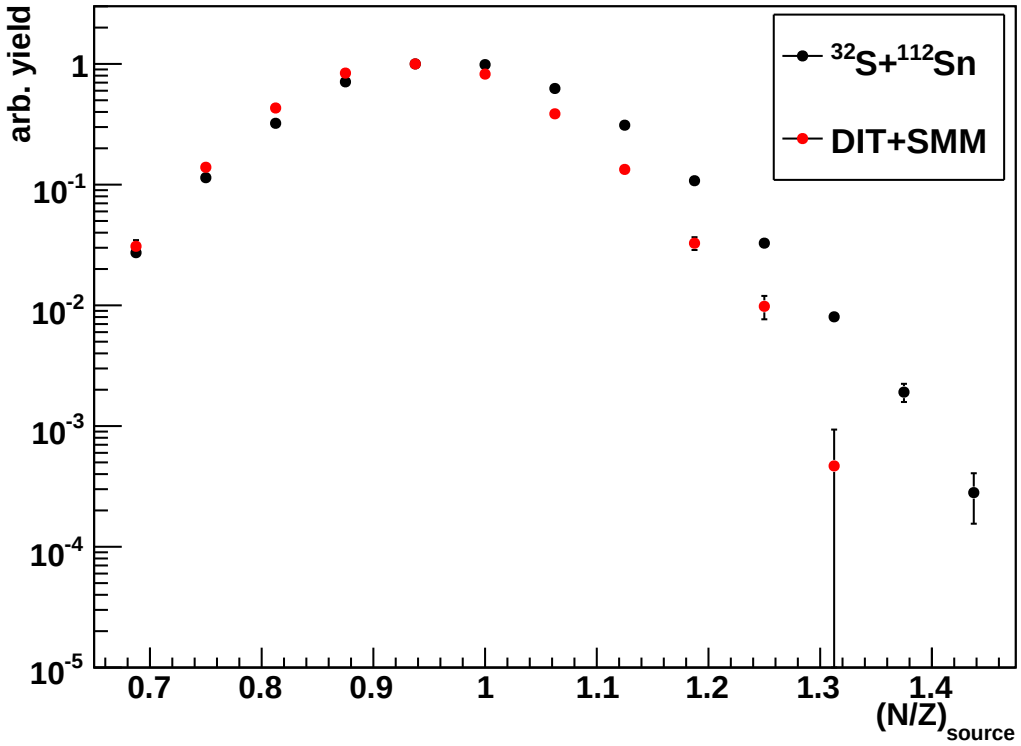

FIG. 32.: The QP N/Z distribution for the ^{32}S + ^{112}Sn at 45 MeV/nucleon system with an E* > 4 MeV/nucleon cut placed upon the source. As shown the experimental distribution (black) has a wider width than the DIT+SMM theoretical calculation (red).

Further observables are discussed in detail in subsequent chapters as they are of great interest to the topics of this dissertation. However with the general observables it is established that for the defined quasi-projectile source when an excitation energy cut of greater than 4 MeV/nucleon are primarily undergoing multifragmentation as shown by its comparison to the DIT+SMM theoretical model.

CHAPTER V

ISOSPIN DEPENDENCE OF FRAGMENTATION

Many studies have been done to study the fragmentation of an excited nucleus [1–37]. One of the main assumptions in many of these studies is the fragmenting source is an average of all sources produced in the reaction. In some studies the source is well constrained [100, 101] but others have many sources of multiple Z and A [60, 61, 111]. This averaging among multiple sources has the possibility of masking trends in the fragmentation yields that are N/Z dependent. With the source definition, as defined in Chapter II, it is possible to probe how the fragmentation of sources evolves within the addition of neutrons by moving from neutron-poor to neutron-rich sulfur sources.

A projectile-like source (PLS) as defined in Chapter III for the reaction ^{32}S + ^{112}Sn at 45 MeV/nucleon consists of an event where the sum of the fragment charge is equal to $Z = 16$, all particles in an event are isotopically identified with 95% confidence, and all fragments in an event are $Z = 1 - 8$. This is done for several reasons. First, there is an uneven geometrical coverage of high Z fragments within the FAUST array. Second, there is an uncertainty of lower excitation events produced within the DIT+SMM framework. These events generate the majority of the larger Z fragments. Third, by selecting events where only fragments of $Z = 1 - 8$ are present it preferentially selects on multifragmentation events. With the reconstructed Z of the source held to that of the beam ($Z = 16$) the mass range of $A = 27$ to $A = 37$ are produced with reasonable statistics. Figure 33 presents the mass distribution of the source where the reconstructed $Z = 16$.

The mass distribution shown in Figure 33 contains all source excitation energies. Figure 34 shows the mass distribution by source excitation energy. There are five excitation energy ranges, $2 - 3$ MeV/nucleon (black circles), $3 - 4$ MeV/nucleon (red

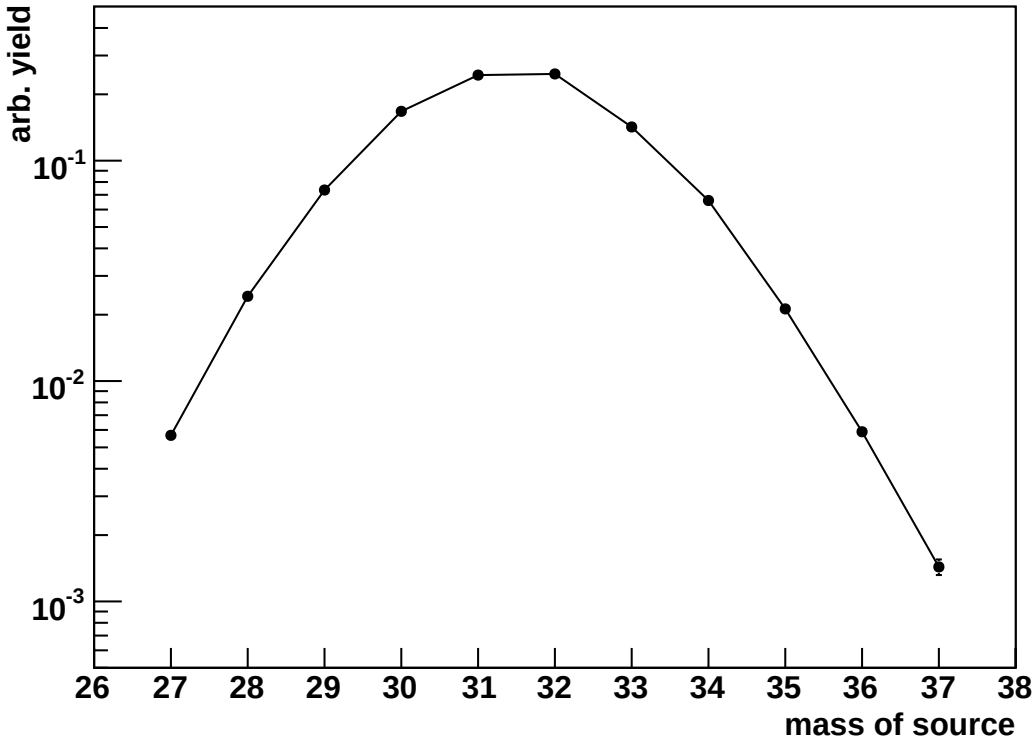

FIG. 33.: The mass distribution of the $\Sigma Z_{frag} = 16$ sources where all fragments in the event are isotopically identified.

squares), $4 - 5$ MeV/nucleon (green triangles), $5 - 6$ MeV/nucleon (blue inverted triangles), $6 - 8$ MeV/nucleon (pink stars). The normalized yield is defined as the yield of each source mass for each excitation energy bin divided by the total number of PLS in each excitation energy bin. This allows for direct comparison of the width of distribution between the different excitation energy bins. As demonstrated in Figure 34 the width of the distribution widens as the system increases in energy. There is an increase in the number of both neutron-poor and neutron-rich sources. This indicates that the increase of the source excitation energy allows for a greater mass range to be populated.

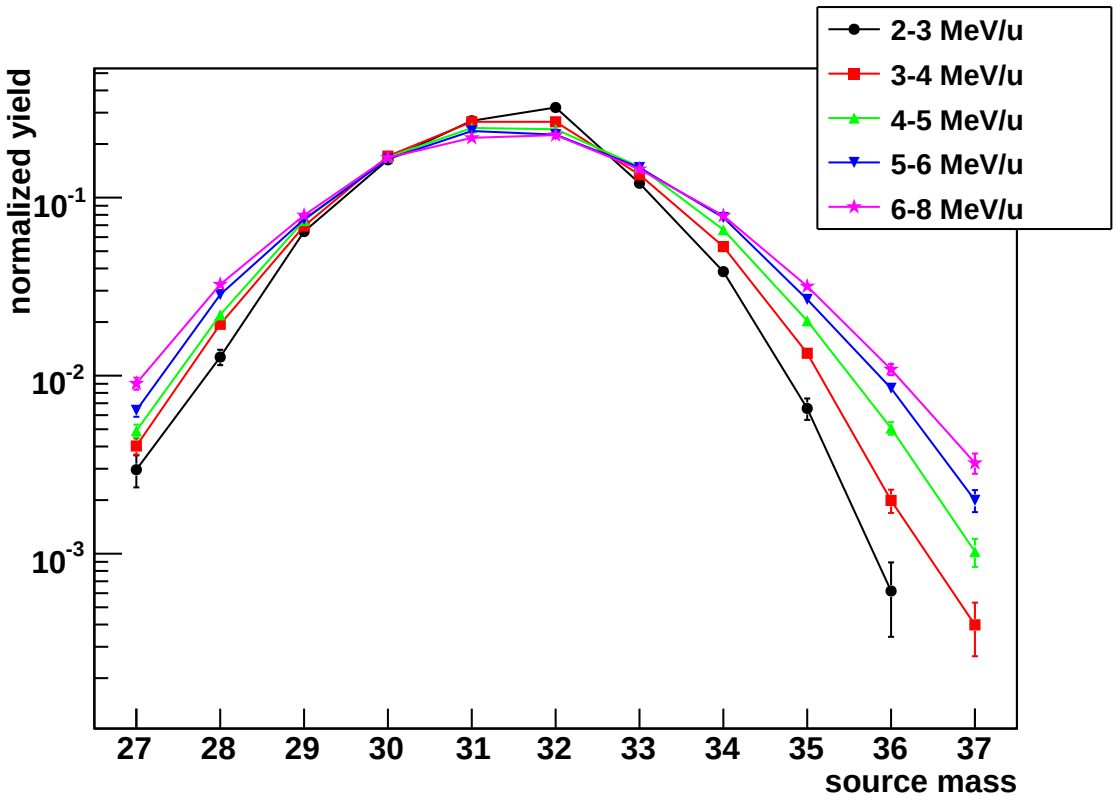

FIG. 34.: The source mass distrubution, where $Z_{sum} = 16$, for the ^{32}S + ^{112}Sn at 45 MeV/nucleon system. There are five excitation energy ranges, $2-3$ MeV/nucleon (black circles), $3-4$ MeV/nucleon (red squares), $4-5$ MeV/nucleon (green triangles), $5-6$ MeV/nucleon (blue inverted triangles), and $6-8$ MeV/nucleon (pink stars). The normalized yield is defined as the yield of each source mass for each excitation energy bin divided by the total number of PLS in each excitation energy bin. This allows for direct comparison between the different excitation energy bins.

The sources of ^{27}S to ^{37}S produce a wide range of isospins as shown in Table VIII. For this work the isospin is defined as $T_z = 2Z - A$. Looking at the charge distribution as a function of isospin, there is an evolutionary trend shown in Figure 35. In this figure, eleven sources are represented from top left (^{27}S) to bottom right (^{37}S). The yield of each element has been normalized to the total source yield for each source mass. This allows for comparisons to be made between sources. For the most neutron-poor source, ^{27}S, there is a strong odd-even behavior. As the neutron content of the source increases, the charge distribution begins to take on an exponential or power law like character.

The trend where the odd-even nature of the charge distribution is correlated to the source isospin has been noted in another study [112]. In this study the examination of the elemental cross sections where $T_z = 0$ and $T_z = -2$ shows the $T_z = 0$ having a greater odd-even behavior when compared to that of $T_z = -2$. The $T_z = -2$ case produces a rapid roughly exponential drop-off. However, this previous study was only able to postulate on the extent of their observation. For the study presented in this work, the ability to identify a wide range of sources, and thus isospin, has been able to show there is a systematic dampening of the odd-even effect as one moves from neutron-poor to neutron-rich sources.

TABLE VIII.: Isospin values for the various quasi-projectile sources.

source	^{27}S	^{28}S	^{29}S	^{30}S	^{31}S	^{32}S	^{33}S	^{34}S	^{35}S	^{36}S	^{37}S
T_z	5	4	3	2	1	0	-1	-2	-3	-4	-5

To explore this observation further the sources ^{30}S, ^{32}S, and ^{34}S from the reaction ^{32}S + ^{112}Sn at 45 MeV/nucleon will be explored along with comparisons to DIT+SMM

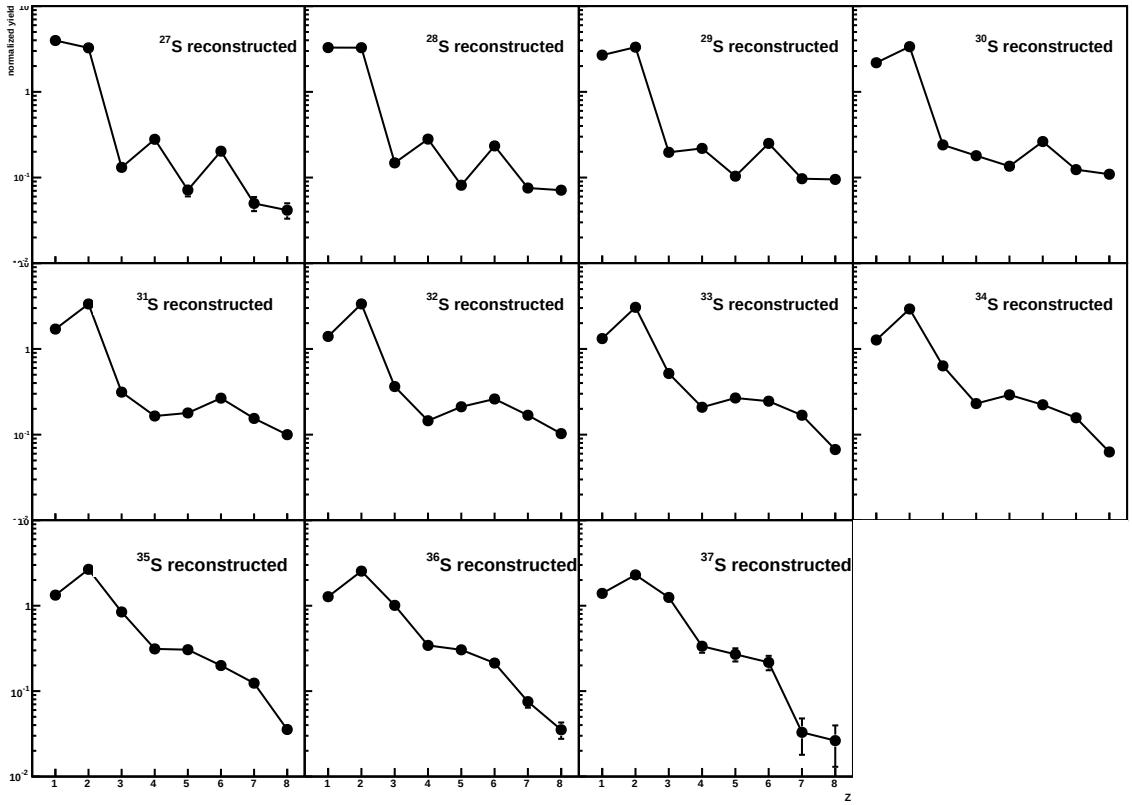

FIG. 35.: The charge (Z) distributions for $Z = 1 - 8$ for the reconstructed sources $^{27-37}$S from the reaction ^{32}S + ^{112}Sn at 45 MeV/nucleon. The yield of each element has been normalized to the total source yield for each source mass.

calculations. Figure 36 shows the experimental charge distribution, in circles, for the ^{30}S (left column) and ^{34}S (right column) sources for the energy bins of $2-3$ MeV/nucleon, $3-4$ MeV/nucleon, $4-5$ MeV/nucleon, $5-6$ MeV/nucleon, and $6-8$ MeV/nucleon. The DIT+SMM calculation where $\gamma = 25$ MeV is represented by squares and for $\gamma = 8$ MeV is represented by triangles, where γ is the symmetry energy coefficient. Each point is normalized to the total number of reconstructed quasi-projectiles produced for each source in a given energy bin. In both cases, the experimental charge distribution changes shape with the increase of the source excitation energy. For the ^{30}S case there is a more pronounced odd-even effect for the lowest energy bins than the ^{34}S case. In both cases, the shape evolves with energy to produce a more exponential behavior of the given Z range. Both the $\gamma = 25$ MeV and $\gamma = 8$ MeV DIT+SMM calculations produce similar results which deviate more at the low excitation energies than the high excitation energies. However, the calculation is able to grossly produce the behaviors in the Z distribution as a function of both the source identity as well as the source energy regardless of the γ value.

One can look deeper at the fragmentation pattern by looking at the average N/Z, $< N/Z >$, vs. Z. for the sources. Figure 37 shows this distribution. In this figure again, the experimental data is represented by circles and the DIT+SMM is represented by red squares ($\gamma = 25$ MeV) and blue triangles ($\gamma = 8$ MeV). The top panel is the ^{30}S, middle panel is ^{32}S, and bottom panel is for the ^{34}S source. As the source mass increases from ^{30}S to ^{34}S it is shown that the $< N/Z >$ vs. Z signal moves from a strong odd-even behavior in the ^{30}S to a more flat distribution for the ^{34}S source. In all cases the theoretical distribution, regardless of the γ value, does produce a reasonable estimate of the observed system behavior. It is to be noted that for the ^{34}S source, the DIT+SMM calculations do not reduce the odd-even behavior enough to match the experimental data. Expanding these observations of the $< N/Z >$ vs.

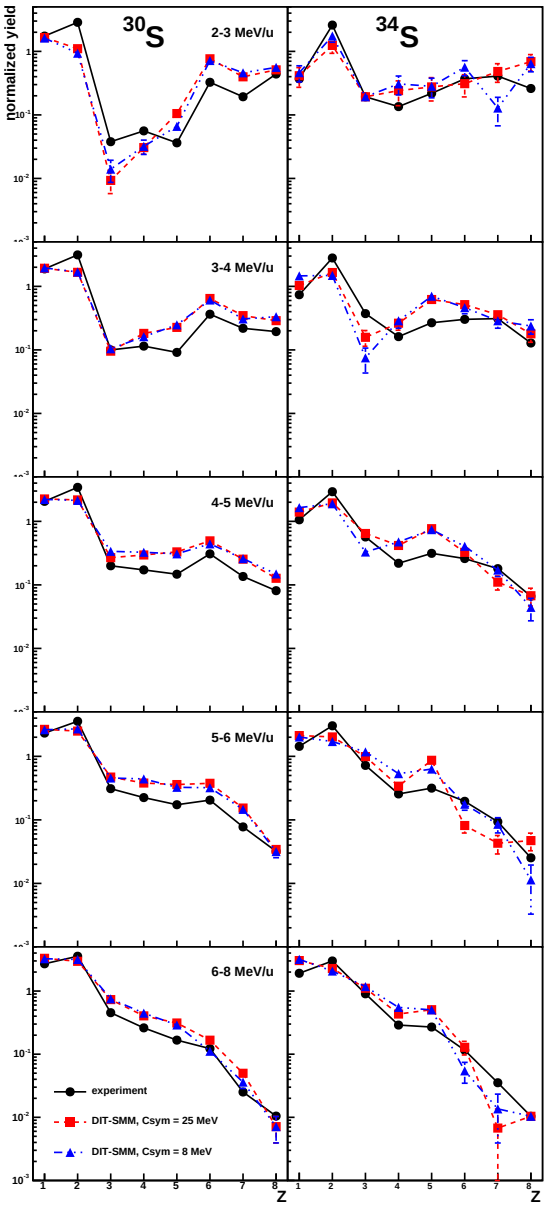

FIG. 36.: The charge distribution for the sources ^{30}S (left column) and ^{34}S (right column) for the reaction ^{32}S + ^{112}Sn at 45 MeV/nucleon. Five excitation energy bins are represented: $2-3$ MeV/nucleon, $3-4$ MeV/nucleon, $4-5$ MeV/nucleon, $5-6$ MeV/nucleon, and $6-8$ MeV/nucleon. Each point has been normalized to the total number of reconstructed quasi-projectile produced for each source in the given energy bin. The DIT+SMM calcuation for $\gamma = 25$ MeV is represented by red squares and for $\gamma = 8$ MeV is represented by blue triangles.

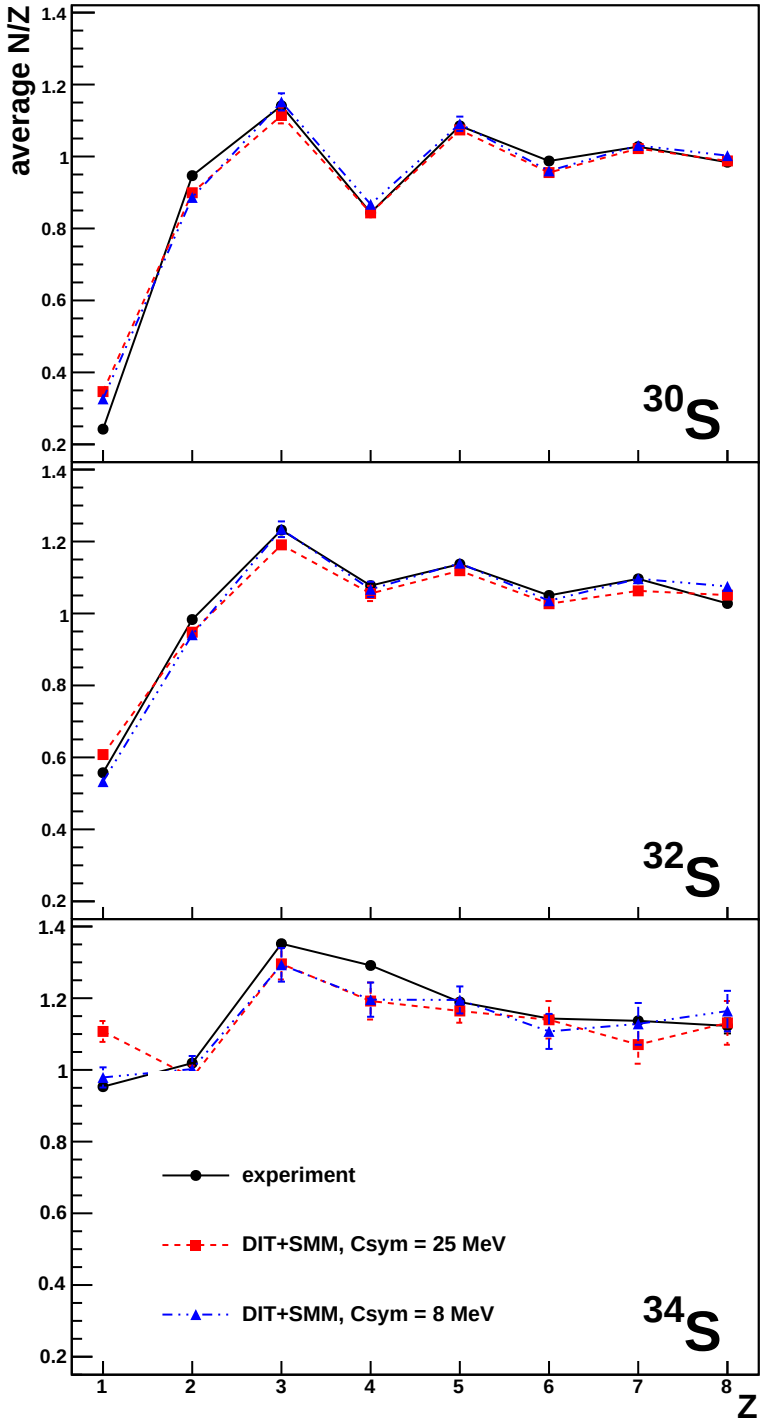

FIG. 37.: The $< N/Z >$ vs. Z distribution for three sources: ^{30}S, ^{32}S, and ^{34}S. The data is represented by circles. The DIT+SMM calculation for $\gamma = 25$ MeV is represented by red squares and for $\gamma = 8$ MeV is represented by blue triangles.

Z observable to include excitation energy is presented in Figure 38.

In Figure 38 each column represents a source, ^{30}S, ^{32}S, ^{34}S, and each row represents a given energy range: low (0-4 MeV/nucleon), mid(4-6 MeV/nucleon), and high ($>$ 6 MeV/nucleon). Once again, the data is represented by circles and the two DIT+SMM calculations are represented, $\gamma = 25$ MeV in red squares and $\gamma = 8$ MeV in blue triangles. Please note that if a point is not represented on the graph, the yield for the given Z is very low if not zero. For the neutron-poor source of ^{30}S each energy bin contains a strong odd-even effect. As the system increases in neutron content, the odd-even effect dampens. In each of the three sources, the increase of excitation energy does not appreciably affect the odd-even (or lack there of) character of the $< N/Z >$ vs. Z observable. The calculations for both γ values reproduce the data reasonably well. It is to be noted that for the ^{30}S high energy bins, only the $\gamma = 25$ DIT+SMM calculation reproduces the entire range of the observable. For the high energy case, the calculation does not produce $Z = 8$ isotopes. Also for the ^{34}S source, the calculations still produce a slight odd-even behavior that is stronger than what is present in the experimental data.

By comparing Figures 37 and 38, it can be concluded that the $< N/Z >$ vs. Z observable is dominated by the N/Z of the emitting source and the source excitation energy has little to no effect. Again, this observable is indepedent of the γ value.

To more fully understand the $< N/Z >$ dependence, a look at the mass distributions of each element will be necessary. Figures 39 and 40 show this mass distribution for $Z = 3 - 6$ and $Z = 7 - 8$ respectively. The yield of each isotope is normalized to the total number of each element produced for a given source. As expected, the more neutron-rich source produces more neutron-rich fragments. When examining the experimental data along with the DIT+SMM calculation there are two main trends - one with $Z = 3 - 6$ represented by Figure 39 and one with $Z = 7 - 8$ represented by

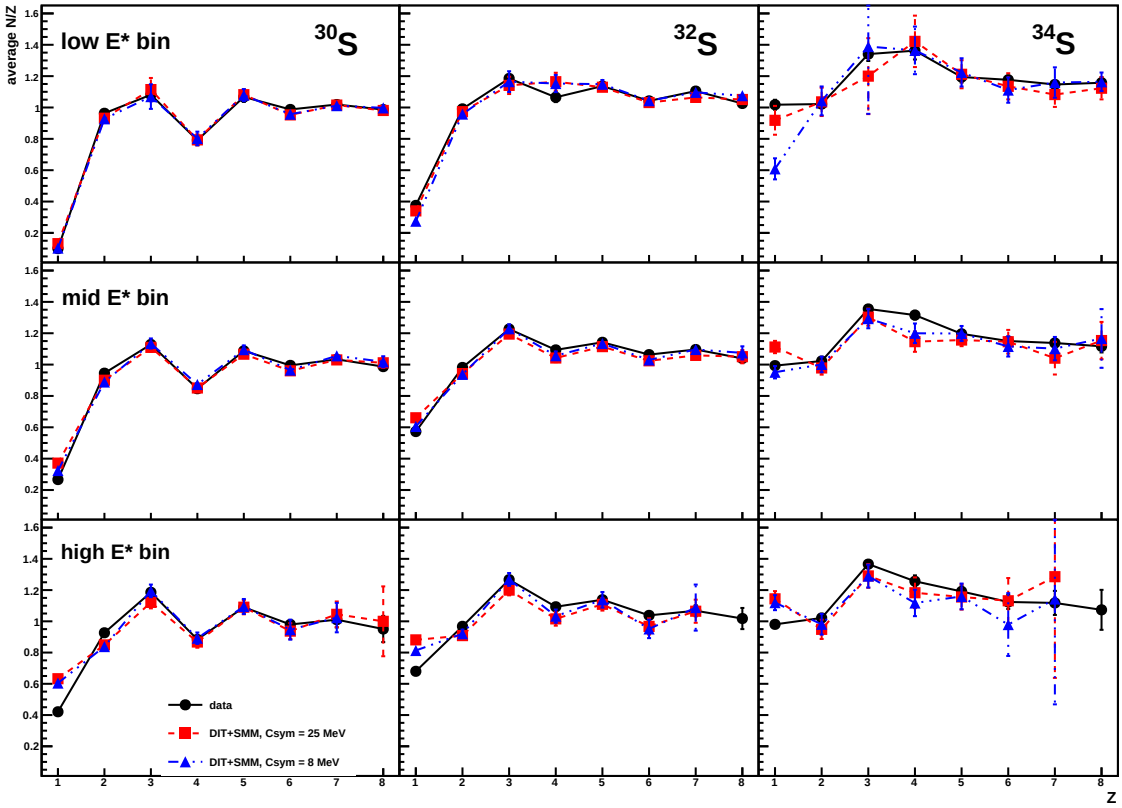

FIG. 38.: The evolution of $< N/Z >$ vs. Z for three different source excitation energy bins: low $(0-4$ MeV/nucleon), mid $(4-6$ MeV/nucleon, and high $(> 6$ MeV/nucleon. The left column is the for the ^{30}S, the middle column is for the ^{32}S source, and the right column is for the ^{34}S. The rows from top to bottom represent the source excitation energy of low, mid, and high. The experimental data is given by black circles. The DIT+SMM calculation for $\gamma - 25$ MeV is represented by red squares and for $\gamma = 8$ MeV is represented by blue triangles.

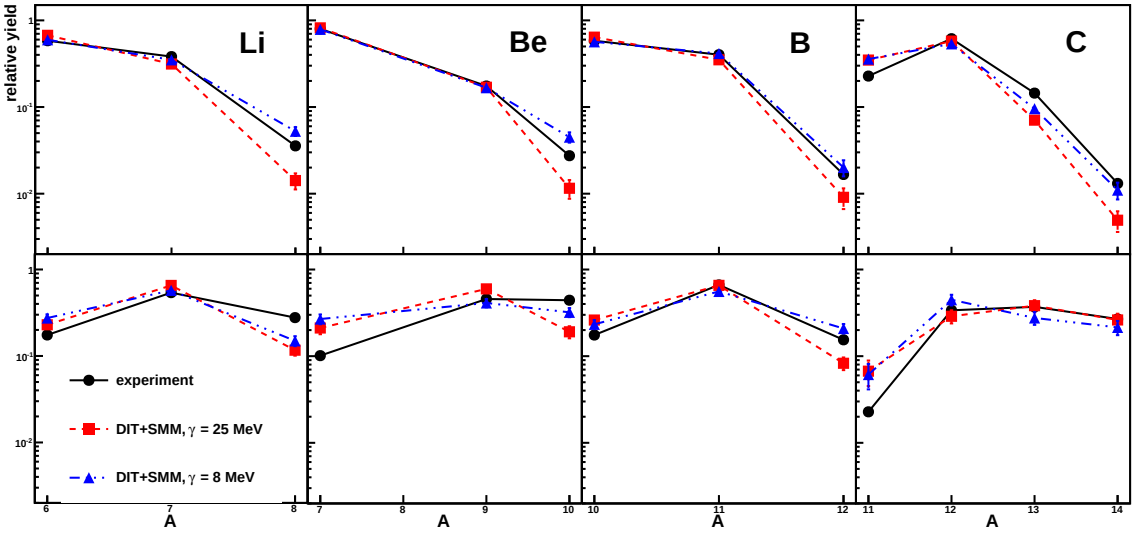

FIG. 39.: The mass distribution for each $Z = 3-6$ for ^{30}S (top line) and ^{34}S (bottom line). The experimental data is represented by black circles and the DIT+SMM calculations are represented by red squares ($\gamma = 25$ MeV) and blue triangles ($\gamma = 8$ MeV). The yield of each isotope is normalized to the total number of each element produced for a given source.

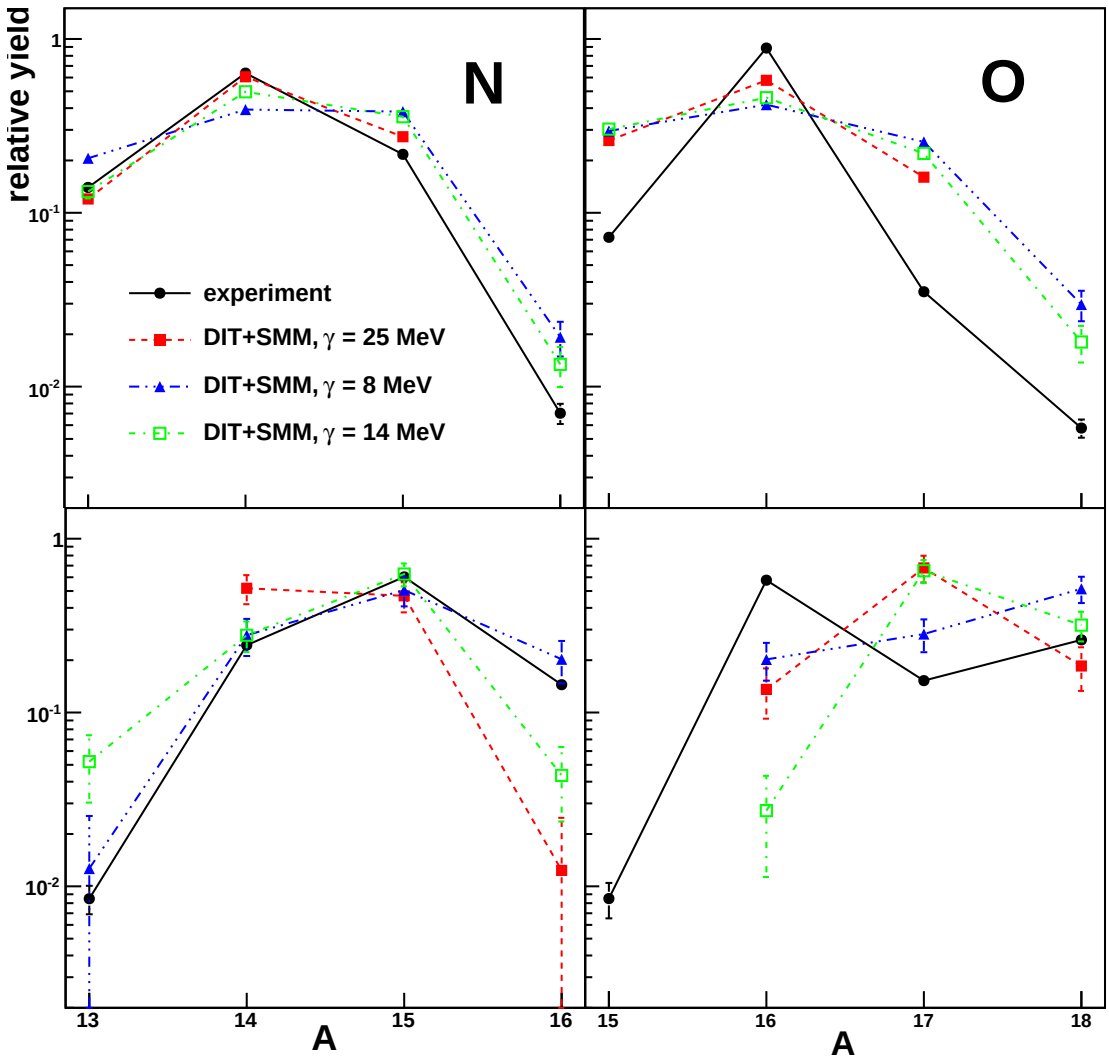

FIG. 40.: The mass distribution for $Z = 7-8$ for ^{30}S (top line) and ^{34}S (bottom line). The experimental data is represented by black circles. Three DIT+SMM calculations are represented in this figure: $\gamma = 25$ MeV (red squares), $\gamma = 8$ MeV (blue triangles), and $\gamma = 14$ MeV (green open squares). The yield of each isotope is normalized to the total number of each element produced for a given source.

Figure 40.

Focusing first on $Z = 3-6$, the two γ values of 25 MeV and 8 MeV do reasonably well in reproducing the data trends with the data usually lying in between the two calculations. For the neutron-rich source, ^{34}S, both calculations over produce the neutron-poor isotopes in all cases. Regardless, the average trend for each element is produced. For the $Z = 7 - 8$, the $\gamma = 25$ MeV cannot reproduce the experimental trend. It does not reproduce the shape nor the yields. For the $\gamma = 8$ MeV calculation, the calculation does better at representing the experimental data for $Z = 7 - 8$ for both sources and trends begin to emerge. The calculation where $\gamma = 14$ MeV was also placed on the $Z = 7 - 8$ mass distribution to illustrate that the value of γ must be lowered outside of commonly used values [113–116]. This observation clearly shows that the symmetry energy is very important for the generation of the $Z = 7 - 8$ isotopes in the ^{32}S+^{112}Sn system.

In the past, it has been customary to use the triton to helium-3 ratio to probe characteristics of the fragmenting source [117–121]. Figure 41 presents the triton to helium-3 ratio (Y_{3H}/Y_{3He}) as a function of source excitation energy for ^{30}S, ^{32}S, and ^{34}S.

There are five source excitation bins, $2 - 3$ MeV/nucleon, $3 - 4$ MeV/nucleon, $4-5$ MeV/nucleon, $5-6$ MeV/nucleon, and $6-8$ MeV/nucleon. The point correlating to each energy bin is placed at the value of the lowest energy in each bin. Please note the y-axis scale changes for each panel in Figure 41. As shown the Y_{3H}/Y_{3He} yield ratio as a function of source excitation energy is drastically different as one moves from neutron-poor sources (^{30}S) to neutron-rich sources (^{34}S). For the neutron-poor ^{30}S source, the ratio is small with a slight increasing trend. For the symmetric ^{32}S source, the value is flat, slightly above one, after the lowest energy bin. One the neutron-rich source ^{34}S is reached,the trend is decreasing exponentially from a very

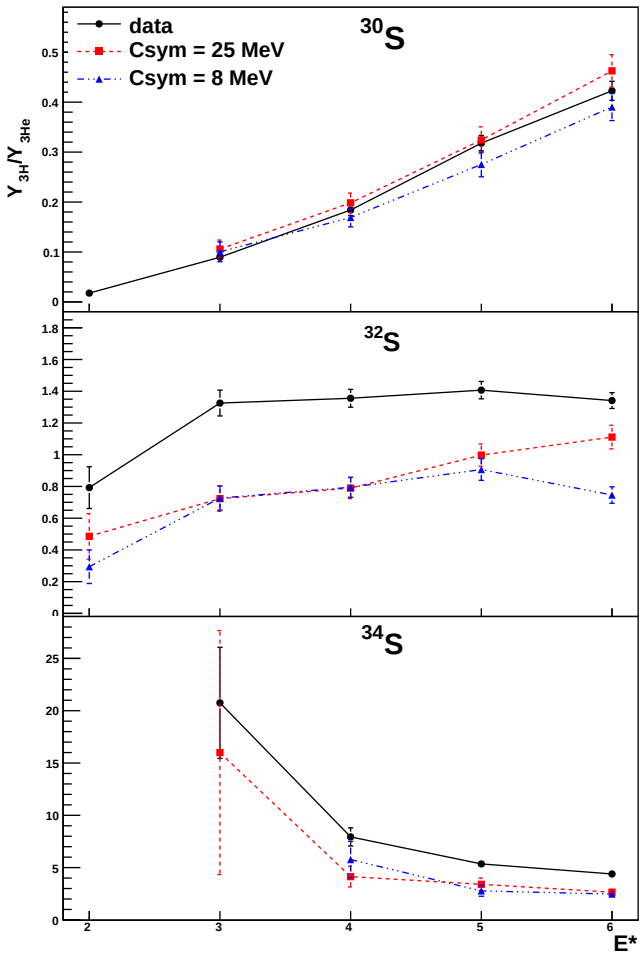

FIG. 41.: The Y_{3H}/Y_{3He} ratio as a function of source excitation energy. There are five source excitation energy bins: $2-3$ MeV/nucleon, $3-4$ MeV/nucleon, $4-5$ MeV/nucleon, $5-6$ MeV/nucleon, and $6-8$ MeV/nucleon. The point correlating to each source excitation energy bin is placed at the value of the lowest energy in each bin. The circles represent the experimental data and the squares and triangles represent the DIT+SMM calculations at $\gamma = 25$ MeV and $\gamma = 8$ MeV respectively. From top to bottom the source neutron content increases from ^{30}S to ^{34}S. The reader is cautioned to note that the y-axis in each panel is different so the trends can be more easily shown.

high ratio value at the low excitation energy bins. While the DIT+SMM calculations are not able to reproduce the value of the ratio, it is quite able to reproduce the trends seen from the neutron-poor to the neutron-rich sources.

In summary, experimental data from isotopically identified quasi-projectiles show a dependence on the fragmentation pattern on the mass, charge and source excitation energy depending on the neutron content of the source. This behavior is grossly predicted by the DIT+SMM picture, which suggest that the decay is highly statistical in nature, however, discrepancies in fragment mass still exist especially in the neutron-rich sources. The differences shown in the mass distributions between ^{30}S and ^{34}S seem to indicate that the neutron content of the hot primary fragments may depend on the symmetry energy, but not the de-excitation process itself. This is due to the observation of the $Z = 7 - 8$ isotope yields which show a greater sensitivity to the value of γ while the $Z = 3-6$ isotope yields are relatively unaffected by the value of γ. A natural explanation of this phenomenon is due to secondary de-excitation via the Fermi break-up, which is mainly responsible for the yields for $Z = 3 - 6$ isotopes. It is clear that the symmetry energy is correlated with the neutron content of the source and is less dependent on the source excitation energy. This observation demonstrates that a simple explanation of decreasing the symmetry energy as a reduction of fragment density due to expansion of hot fragments may not work. Other explanations such as effects of surface symmetry energy cannot be justified in this framework as the data uses the same fragments from both neutron-poor and neutron-rich sources. It is possible that the 95% confidence cut on the experimental data could be biasing the results, however, this is not the case. Appendix B shows examples of graphs presented in the chapter, but with no confidence cut placed on the isotopes. The cut shows little to no change on the results presented in this chapter. These findings are of importance in calculations and to our understanding in the intricacies of nucleonic

partitioning within an equilibrated system.

CHAPTER VI

COULOMB PROXIMITY

It has been predicted using the SMM model that the fragment partitions and kinematic characteristics of fragments can change in the presence of an external Coulomb field [122]. From the study in reference [122] it has been theoretically suggested that the presence of this external Coulomb field produces a spatial anisotropy at both low and high excitation energies. To create this spatial anisotropy, the Coulomb field is postulated to allow the system to preferentially break-up into a configuration comprised of a large fragment and many smaller fragments. By preferentially breaking into a large fragment and many smaller fragments, the fragments can arrange themselves in such a fashion as to minimize the Coulomb barrier. To arrive at the minimum Coulomb barrier, the small fragments will tend to position themselves between the largest fragment and the source responsible for the external Coulomb field.

A direct result of the spatial anisotropy is an anisotropy in the fragment velocities after Coulomb acceleration. This velocity anisotropy causes the intermediate mass fragments (IMFs) to preferentially emit towards the direction of the second source, while the largest fragments will be preferentially emitted away from the second source. This anisotropy in the velocities has been shown using the statistical multifragmentation model (SMM) [122]. By looking at the parallel velocities of fragments from a well defined source, this model described an asymmetric parallel velocity distribution as a direct result from the presence of an external Coulomb field.

The parallel velocity spectra from the reaction of ^{32}S + ^{112}Sn at 45 MeV/nucleon show a clear velocity anisotropy present from many isotopes. As an example, the parallel velocity spectrum for ^{7}Li is given in Figure 42. In this figure, because the system was converted to the frame of the emitting source, zero represents the center of the

emitting source. Values that are in the positive direction represent particles that are being emitted away from the target while negative values are particles being emitted towards the target. It is clear from the ^{7}Li spectrum that there is a distinct anisotropy present between the positive (forward) and negative (backward) components with a preferential emission in the backwards direction. The emissions in the positive direction are particles being emitted away from the target while those in the negative direction are those emitted towards the target.

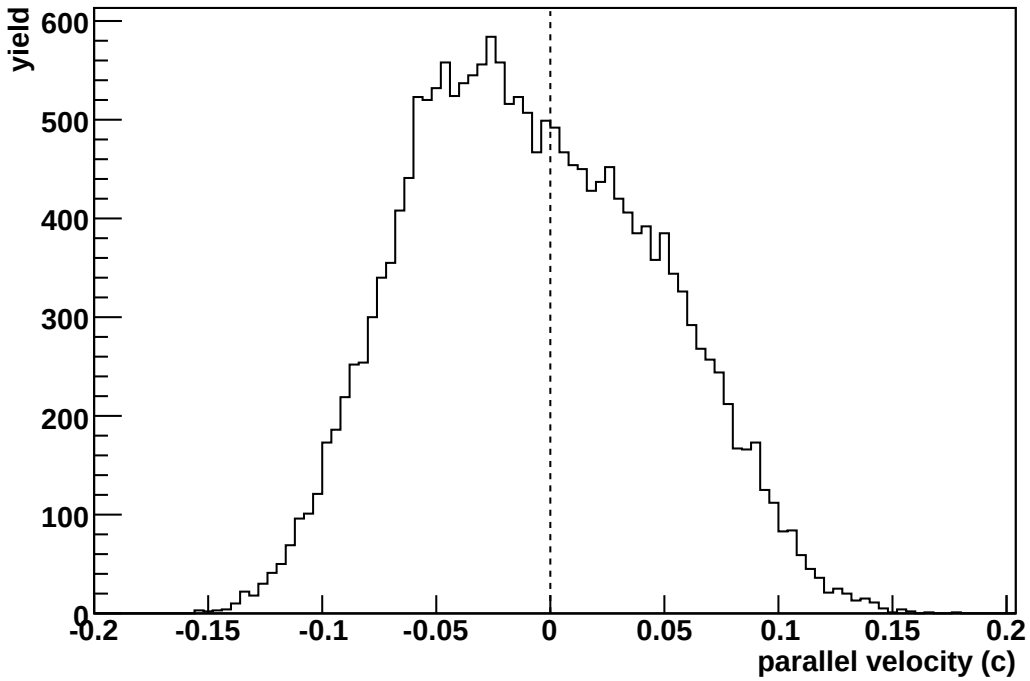

FIG. 42.: The parallel velocity spectrum for ^{7}Li in the frame of the emitting source. The dotted line at zero is to aid the reader.

In an attempt to quantify the above phenomena, a simple integration can be performed. The total number of fragments emitted in the positive or forward direction

is compared to those emitted in the negative or backward direction. The ratio of forward emitted particles to backward emitted particles is taken

$$R_{front/back} = \frac{Y_{front}}{Y_{back}} \tag{6.1}$$

The ratio for each isotope for $Z = 2 - 6$ is provided in Table IX. For these ratios, the larger the number, the more forward emitted the particle is. If this ratio is greater than one, then the isotope is preferentially emitted in the forward direction.

These ratios show that there is an elemental trend as well as an isotopic trend present. On average, as Z increases the ratio values for the isotopes become larger indicating more forward emission. Once $Z = 6$ is reached, all isotopes have a ratio greater than one. This average trend supports the idea that the larger the element in an event the more likely it is to be emitted away from the target. In contrast the lower the Z of the element the more likely it is to be emitted towards the target.

There is also a clear isotopic trend within each element. As isotope mass increases, the ratio decreases, indicating that the heavier particles are being emitted more in the backwards direction. To fully explain this phenomenon, not only does an external Coulomb field need to be present, but the angular momentum must be taken into account. In SMM calculations, when adding the angular momentum the N/Z ratios of the IMFs increase. This increase in the N/Z ratio becomes larger for the IMFs that are closer to the target. The experimental data shows that the fragments with the largest N/Z are preferentially emitted towards the target, not just for the IMFs but for all Z values.

In an attempt to describe the observations that the largest N/Z is preferentially emitted towards the target as well as the larger the Z the more forward emitting the particles, DIT+SMM calculations were performed. It has been postulated that the distance between the sources is an important factor in the resulting anisotropy due to

TABLE IX.: The ratio of forward emitted particles to backward emitted particles. Values less than one show greater emission in the backwards direction.

isotope	$R_{front/back}$
^{3}He	1.10 ± 0.01
^{4}He	0.80 ± 0.00
^{6}He	0.46 ± 0.02
^{6}Li	0.76 ± 0.01
^{7}Li	0.75 ± 0.01
^{8}Li	0.37 ± 0.01
^{7}Be	1.10 ± 0.02
^{9}Be	0.66 ± 0.02
^{10}Be	0.59 ± 0.02
^{10}B	0.97 ± 0.02
^{11}B	0.85 ± 0.01
^{12}B	0.68 ± 0.04
^{13}B	0.14 ± 0.06
^{11}C	1.65 ± 0.05
^{12}C	1.60 ± 0.03
^{13}C	1.40 ± 0.03
^{14}C	1.26 ± 0.06

TABLE X.: The ratio of forward emitted particles to backward emitted particles for DIT+SMM calculations performed at 20 fm, 40 fm, and 60 fm. In addition, the last column represents the DIT+SMM calculation with no target (external Coulomb field) present during de-excitation.

isotope	20 fm	40 fm	60 fm	no target
^{3}He	1.02 ± 0.02	0.99 ± 0.03	0.98 ± 0.02	0.95 ± 0.03
^{4}He	0.93 ± 0.01	0.94 ± 0.01	0.95 ± 0.01	0.90 ± 0.02
^{6}He	0.88 ± 0.10	1.35 ± 0.21	0.61 ± 0.08	1.13 ± 0.23
^{6}Li	0.85 ± 0.02	0.89 ± 0.03	0.94 ± 0.02	0.79 ± 0.04
^{7}Li	0.86 ± 0.03	0.86 ± 0.03	0.89 ± 0.03	0.84 ± 0.05
^{8}Li	0.61 ± 0.07	0.71 ± 0.08	0.90 ± 0.09	0.95 ± 0.17
^{7}Be	0.98 ± 0.03	0.97 ± 0.04	1.05 ± 0.03	0.90 ± 0.05
^{9}Be	0.78 ± 0.04	0.87 ± 0.05	0.78 ± 0.04	0.71 ± 0.06
^{10}Be	0.50 ± 0.05	0.75 ± 0.10	0.87 ± 0.08	0.74 ± 0.12
^{10}B	0.87 ± 0.03	0.92 ± 0.03	0.99 ± 0.03	0.86 ± 0.05
^{11}B	0.86 ± 0.03	0.84 ± 0.03	0.94 ± 0.03	1.01 ± 0.05
^{12}B	0.88 ± 0.10	1.06 ± 0.14	0.54 ± 0.07	0.76 ± 0.16
^{13}B	NA	NA	NA	NA
^{11}C	1.08 ± 0.04	0.95 ± 0.04	1.00 ± 0.04	0.86 ± 0.06
^{12}C	1.03 ± 0.02	0.97 ± 0.03	0.93 ± 0.02	0.87 ± 0.04
^{13}C	1.03 ± 0.05	0.94 ± 0.05	0.95 ± 0.04	0.81 ± 0.06
^{14}C	0.80 ± 0.12	1.03 ± 0.17	0.77 ± 0.10	1.08 ± 0.24

the fact that distance is related to the strength of the Coulomb field. To account for this, the DIT+SMM calculations were performed at distances of 20 fm, 40 fm, and 60 fm. In addition, calculations were performed where no target, which provides the external Coulomb field, was present during the de-excitation.

Using the ratio method described above, the results for the calculations are presented in Table X. When assessing these values it must be remembered that the theoretical calculation has been filtered to match the experimental set-up. Once the theoretical calculation has gone through the FAUST filter, it is reconstructed and treated in the same manner as the experimental data. First looking at the ratio for the isotopes present from the no target calculation, the average ratio value is at or slightly below one for most isotopes. To ensure that the center-of-mass for the emitting source is preserved, the parallel momentum distribution for all particles is plotted, see Figure 43. As the center-of-mass of the emitting source is calculated in momentum space it is important to make assessments to how valid the reconstruction is by looking at the momentum. As shown, the parallel momentum distribution has a forward to backward ratio of 0.99 ± 0.02 which indicates that the center-of-mass of the emitting system is calculated correctly and the distribution of all particles is nearly symmetric in the parallel direction about the center of the source.

For the three distances, many ratio values are different than the no external Coulomb field (no target) case. Therefore, the Coulomb field is affecting the distribution. In many cases, there is a slight decrease in the ratio as one increases isotope mass within each specified distance. Even though many of the values of the calculation do not match the experimental data (Table IX), the indicated trends do follow the above stated experimental trends as well as previously published calculations [122].

For the IMF's (Li and Be), as the distance between the target and projectile increases, the ratio value tends to increase, favoring a forward emission direction.

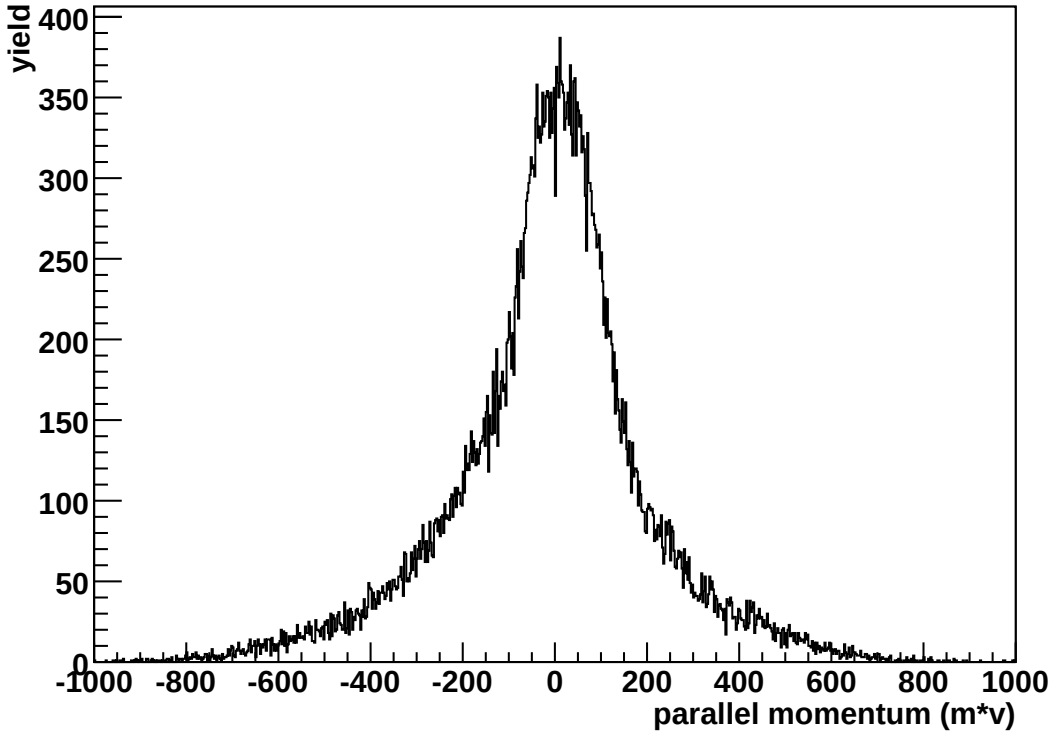

FIG. 43.: The parallel momentum for all particles emitted from a ^{32}S system where no external Coulomb field is present during the de-excitation. The $R_{front/back} = 0.99 \pm 0.02$.

This is especially true for the neutron-rich isotope. This is unexpected as previous calculations have suggested that the larger distances between the target and projectile prefer to fill the mid-rapidity region, i.e., the area between the target and projectile [122]. The increasing value that is demonstrated by the calculations show that there is an increase in the forward emission direction as the distance increases. However for $Z = 6$ the larger the distance, the more the fragments are emitted in the backward direction. This can easily explained by the larger distances lead to a lower Coulomb field. This has diminished effect in pushing the heavy fragment away from the target.

It is unlikely the source selection is the main reason for the discrepancy between the observation presented in the above paragraph and the previously published work [122]. A very likely explanation for this variation is source size. All previous theoretical studies have been done with an Au + Au system leading to a source that is six times larger than the sources studied in this work. One must also consider the source N/Z as well, as previous chapters have shown the the fragment yields are correlated to this value. This source N/Z ratio may also have additional impact on the anisotropy. This is an important factor to consider as the system present here produces many neutron-poor sources in comparison to the neutron-rich Au + Au system used in previous studies.

It has been generally assumed that a parallel velocity plot should have a symmetric, Gaussian-like distribution. However, many of the isotopes in the experimental data presented in this work have a parallel velocity that does not follow this assumption. Again looking at the parallel velocity spectrum in Figure 42, there are visually two components; one in the forward (positive) direction and one in the backward (negative) direction. To produce a fit to this data, it was chosen to fit a Gaussian distribution to the forward component and an additional Gaussian distribution to the backward component. The sum of these Gaussian distributions produce a reasonable

fit to the entire parallel velocity spectrum. An example of this fit is given for ^{7}Li in Figure 44.

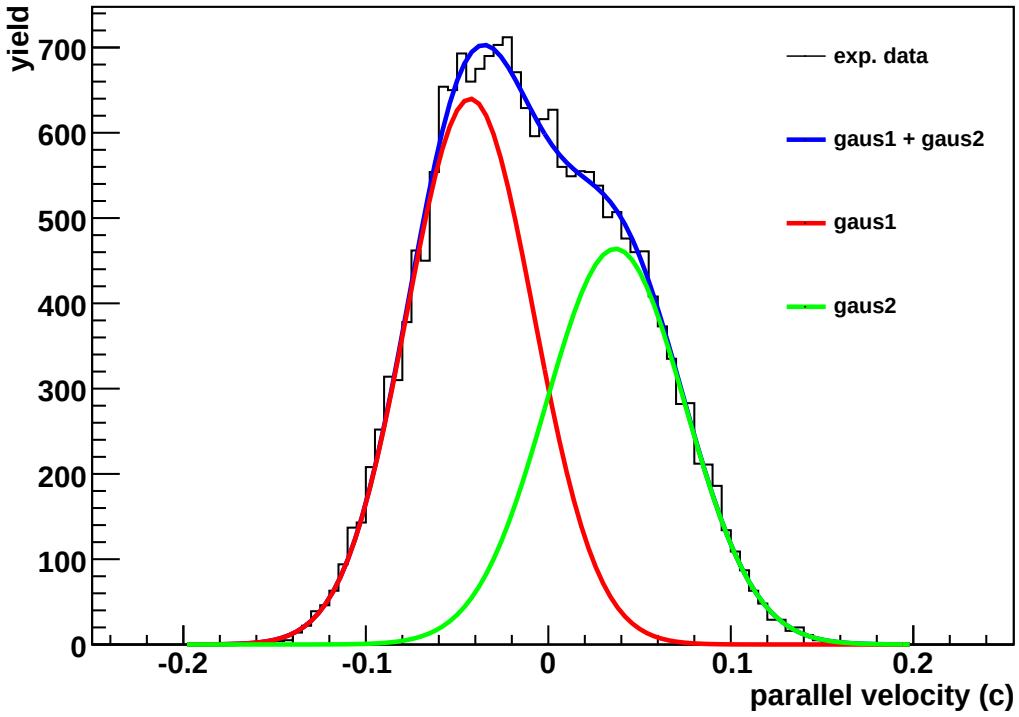

FIG. 44.: The parallel velocity for ^{7}Li with the corresponding Gaussian fits. The experimental data is represented by the black histogram, the red and green lines represent the negative (gaus1) and forward (gaus2) fitting Gaussians respectively. Finally the blue line represents the sum of gaus1 and gaus2.

Using the assumption that each parallel velocity spectrum is a sum of two Gaussians to the $Z = 2 - 6$ elements, it is found that the two Gaussian method fits the experimental data reasonably well. However, this does not provide a unique solution in desrcibing the parallel velocity distributions. The reader is referred to appendix C for further assessment of this method.

Using the parallel velocities, there is a clear anisotropy present in the particle emission within the experimental data. Using a simple ratio between the yield of forward emitting particles to backward emitting particles, it is found that the more neutron-rich an isotope, the more likely it is to be emitted in the backward direction. Also, the larger the Z of the emitting fragment, the more forward emitting the particle tends to be. This is postulated to be a direct result of the presence of an external Coulomb field. Using the DIT+SMM theoretical model, the anisotropy is found to change as a function of the distance between the target and projectile. As there is a measurable effect in the parallel velocity spectrum which changes as a function of the distance from the target, it is plausible that this signal could be a potential experimental probe to the break-up distance of the projectile from the target.

CHAPTER VII

KINETIC ENERGY SPECTRA

It has been shown in previous works that the average kinetic energy for both central and mid-peripheral collisions show the highest average kinetic energy for the most neutron poor isotopes [60, 61]. While previous works have focused on much heavier systems such as ^{112}Sn + ^{112}Sn and ^{114}Cd + ^{92}Mo, they show similar trends. For the ^{112}Sn + ^{112}Sn study [61], they state the neutron-poor isotopes are significantly more energetic than those of neutron-rich isotopes of the same element. They postulate that this is a direct consequence that the neutron-poor isotopes are emitted earlier than their neutron-rich counterparts during the decay process. For the ^{114}Cd + ^{92}Mo study [60], the usage of the average transverse kinetic energy is used to minimize the contamination from other sources, but the average transverse kinetic energy also shows that for isotopically identified fragments, the neutron-poor isotopes exhibit larger average transverse kinetic energies than heavier isotopes of the same element. These works have been done with specific angular or parallel velocity cuts to try to reduce pre-equilibrium and/or neck emission. It will be shown in this work that specific angular or parallel velocity cuts place constraints on the resulting system that affect average kinetic energy trends.

To study the kinetic energy trends for this work, the spectrum of He, Li, and C isotopes for the ^{32}S + ^{112}Sn at 45 MeV/nucleon system will be studied. These spectrum are representative of the three systems ^{32}Sn + ^{112,124}Sn, ^{nat}Au at 45 MeV/nucleon. The spectrum show that there are distinct differences for each isotope. The He, shown in Figure 45, and Li, shown in Figure 46 show similar trends. The most neutron-poor isotope in each (^{3}He and ^{6}Li) have a softer energy spectra than their neutron-rich counterparts. The peak for the neutron-rich isotope appears at a higher energy and

the slope of the tail region is smaller. For the C isotopes, in Figure 47, the energy spectrum for each isotope are very similar and any differences between the peak and the tail regions are not clear.

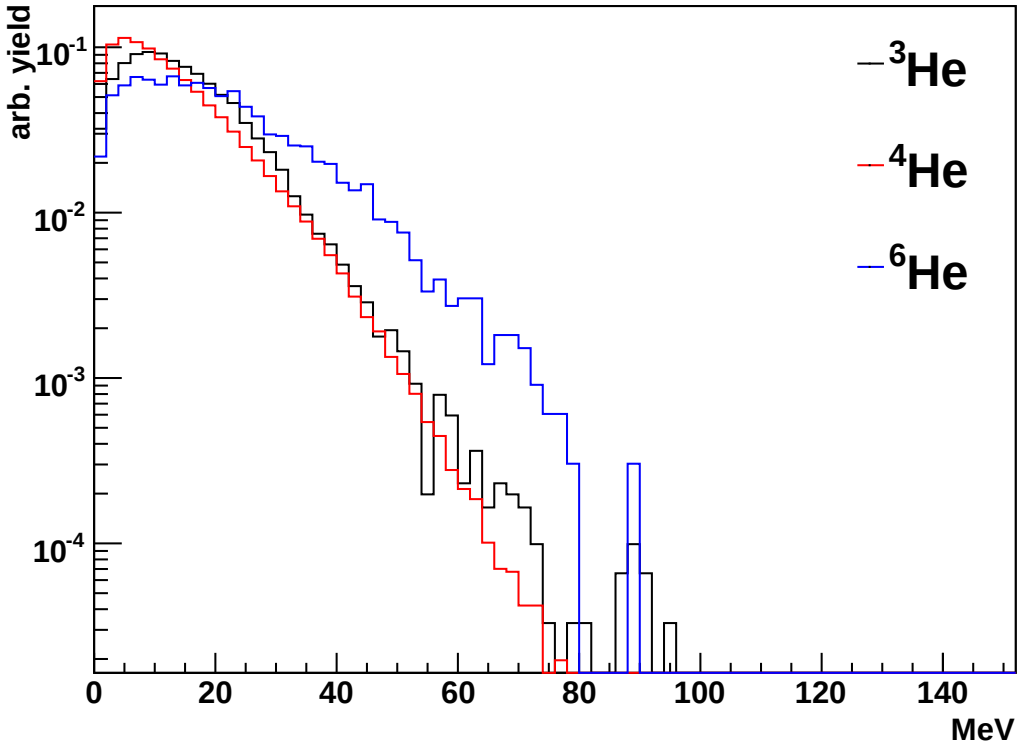

FIG. 45.: The energy spectra for helium isotopes from the reaction ^{32}S + ^{112}Sn at 45 MeV/nucleon. The colors black, red, and blue represent ^{3}He, ^{4}He, and ^{6}He respectively. The spectra have been normalized to the total yield of each isotope.

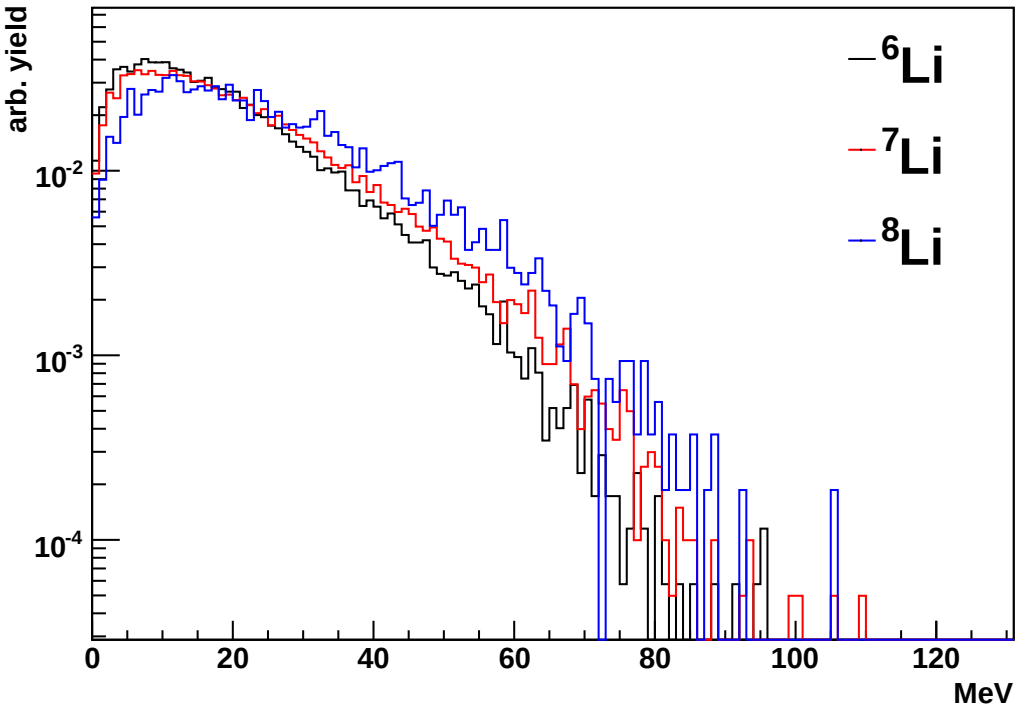

FIG. 46.: The energy spectra for lithium isotopes from the reaction ^{32}S + ^{112}Sn at 45 MeV/nucleon. The colors black, red, and blue represent ^{6}Li, ^{7} Li, and ^{8}Li respectively. The spectra have been normalized to the total yield of each isotope.

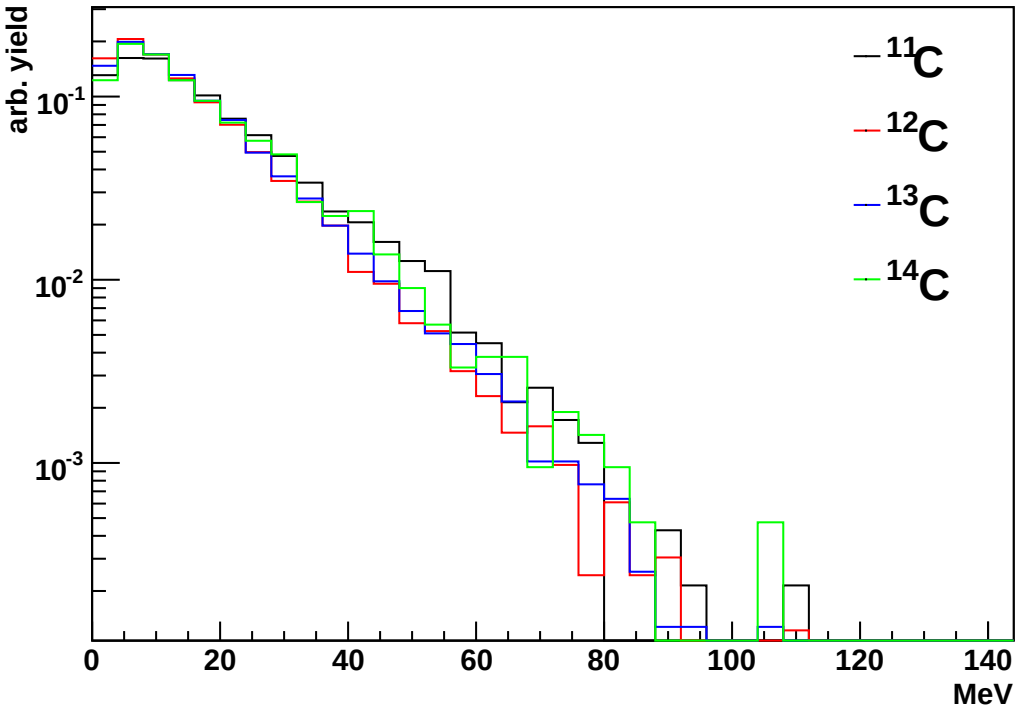

FIG. 47.: The energy spectra for carbon isotopes from the reaction $^{32}S + ^{112}Sn$ at 45 MeV/nucleon. The colors black, red, blue and green represent ^{11}C, ^{12}C, ^{13}C, and ^{14}C respectively. The spectra have been normalized to the total yield of each isotope.

Table XI presents the extracted average energy for each isotope of He, Li, and C for the three targets. For both He and Li, with the exception of ^{4}He, there is an increase in the average kinetic energy as one increases fragment mass for all three targets. For Carbon, there is an increase in the average kinetic energy as one increases from ^{12}C - ^{14}C. ^{11}C exhibits the highest average kinetic energy for the C isotopes. It is not unreasonable for the C isotopes to behave slightly differently than the He and Li isotopes as C is most likely the largest fragment in a given event and represents almost 40% of the source mass.

The trends presented in Table XI are different for the He and Li than those in previous works [60, 61] where it was seen that the neutron-poor isotope has a higher average kinetic energy than its neutron-rich counterparts. For carbon, the difference between the work shown in this dissertation and those previously published is similar. The neutron-poor isotope of ^{11}C has a greater average kinetic energy but for the $^{12-14}$C the trends are different. The average kinetic energy vs. carbon mass is more of a parabolic shape with the ^{11}C and ^{14}C have similar average kinetic energies. This trend is different than the Liu et. al. case [61] and for the central and mid-peripheral cases where the sources were cut on their velocity in the ^{114}Cd + ^{92}Mo system [60]. In the ^{114}Cd + ^{92}Mo system [60] when a fragment selection is made based on its angle of emission, there is a flattening of the average transverse kinetic energy for the carbon isotopes. As discussed, in the previous studies [60, 61], the experimental data only represents a given angular or parallel velocity cut. Because an isolated source has been identified for this work, all angles and parallel velocities are considered. This averaging could be obscuring differences based on the angle as shown in the previous works.

To explore this possibility, angular cuts have been placed on the ^{112}Sn system. Four θ bins have been placed on the data: $0-45^{\circ}$, $45-90^{\circ}$, $90-135^{\circ}$, and $135-180^{\circ}$

TABLE XI.: The average kinetic energy in MeV for He, Li, and C isotopes from reconstructed quasi-projectiles.

isotope	^{112}Sn (MeV)	^{124}Sn (MeV)	^{nat}Au (MeV)
^{3}He	14.95 ± 0.06	14.26 ± 0.05	15.44 ± 0.07
^{4}He	12.70 ± 0.02	12.07 ± 0.01	13.49 ± 0.02
^{6}He	20.46 ± 0.24	20.80 ± 0.23	22.26 ± 0.25
^{6}Li	18.08 ± 0.10	17.14 ± 0.09	19.34 ± 0.12
^{7}Li	20.16 ± 0.10	19.41 ± 0.09	21.62 ± 0.11
^{8}Li	24.13 ± 0.22	23.34 ± 0.21	26.21 ± 0.24
^{11}C	17.19 ± 0.21	16.05 ± 0.18	19.90 ± 0.29
^{12}C	14.42 ± 0.10	13.32 ± 0.08	16.43 ± 0.12
^{13}C	14.97 ± 0.14	14.42 ± 0.12	16.74 ± 0.16
^{14}C	16.35 ± 0.14	15.59 ± 0.12	18.42 ± 0.16

all in the quasi-projectile frame. This allows for the angular dependencies of particle types to be quantified. The average kinetic energy by angular cut are shown in Table XII. There is a clear dependence on the average kinetic energy based on its angle of emission. It is hard to extract global trends, but it is possible to make a few statements about the system.

Beginning with the He isotopes, ^{4}He in all cases is lower in energy than the other He isotopes. This is most likely due to its high binding energy as well as it has multiple production pathways. For angles $< 90^{\circ}$ both ^{3}He and ^{6}He have similar mean kinetic energies, but for angles $> 90^{\circ}$ there is an increase in the average kinetic energy as the mass of the isotope increases from ^{3}He to ^{6}He. For Li, a very similar trend is seen. For angles $< 45^{\circ}$ the values for all isotopes are similar. For angles $> 45^{\circ}$ there is an increase in the average kinetic energy as the mass of the isotope increases. For C isotopes, at angles $< 90^{\circ}$ there is a decrease in the average kinetic energy as the mass of the isotope increases. For angles $> 90^{\circ}$ the trend is reversed and again, the average kinetic energy increases as the mass of the isotope increases. It is not surprising that the trends for C is different than for He and Li as C is most likely the largest fragment in a given event. It is also worthy to note the spread in the energy between the neutron-poor and neutron-rich isotopes by angular bin. For He and Li, at the most forward angular bin, the spread is small. As the angle of emission increases the difference between the two also increases. Using Li as an example, the spread from ^{6}Li to ^{8}Li is 0% for the most forward angles while for the $135 - 180^{\circ}$ angle bin the spread is over 50%. This trend is reversed for the C isotopes with the most forward angles having a large difference in energy while the most backwards emissions are closer in energy.

Differences, such as those described above, between particle type and angle of emission show that there is an angular dependence on the average kinetic energy of

particles from an emitting source. Care needs to be taken when describing source properties from only a portion of the spatial distribution. It is possible that these differences are due to the presence of the external Coulomb field during de-excitation, however this is not the case. Table XIII shows the average kinetic energy for each of the theta bins described above for the DIT+SMM calculation where there is no external Coulomb field present during the de-excitation process. In Table XIII the calculation has been placed through the FAUST filter. By looking that the trends present in Table XIII it is evident that there is an angular dependence of the average kinetic energy on the angle of emission. As there is no external Coulomb field present, it is clear that the external Coulomb field is not the cause of the change in the average kinetic energy by angle of emission.

One must also be vigilant in ensuring that the detector array is not introducing the changes in the average kinetic energy. Table XIV shows the average kinetic energy for the four theta bins for the DIT+SMM calculation with no external Coulomb field and no filtering. When looking at Table XIV there are changes in the average kinetic energy by element, isotope, and theta just as in the experimental data. It can be concluded that the changes in the average kinetic energy by theta cannot be attributed to the FAUST filter and an external Coulomb field. It is postulated that this phenomena is attributed to the presence of angular momentum, which is perpendicular to the z-axis, in the SMM theoretical calculation. The angular momentum allows for an enhancement in the emission of isotopes in the forward/backward direction. The angular momentum allows for a few MeV of kinetic energy to be added to the fragments which translates into the observable which we see as changes in the average kinetic energy based on the angle of emission [123].

Subsequently, Table XV shows a DIT+SMM calculation for the ^{32}S + ^{112}Sn at 45 MeV/nucleon reaction. In this calculation the break-up was allowed to occur at

a time of 50 fm/c from the projectiles interaction with the target. By comparing the trends present in Table XIII and Table XV it is evident that the presence of the external Coulomb field produces changes in the average kinetic energy values than those from no external Coulomb field. However, the differences between the external Coulomb field and the no external Coulomb field calculations are not uniform between the isotopes and elements. Regardless of the magnitude of the average kinetic energy, there is an angular dependence on the average kinetic energy of particles from an emitting source. It can be concluded that this trend is independent of the presence of an external Coulomb field during the de-excitation process.

Directly comparing the experimental data (Table XII) to that of the DIT+SMM calculation with an external Coulomb field during de-excitation (Table XV) it can be seen that many of the same effects are present in the theoretical calculation as in the experimental data described above. However, the DIT+SMM is not able to reproduce the average kinetic energy values in many instances and the trends within each element are not as strong as the experimental data.

Another method of looking at this trend is to look at the dependence of the average kinetic energy on the source N/Z. Table XVI displays the average kinetic energy of each isotope for three reconstructed sources, ^{30}S, ^{32}S, and ^{34}S, for the system ^{32}S + ^{112}Sn at 45 MeV/nucleon. When comparing for each isotope across the sources masses, the general trend that emerges is that there is an increase in the average kinetic energy as one increases the source mass. The largest increases occur within the C isotopes. For the most neutron-rich isotopes present it is noted that the error bars are large due to low statistics. There is a dependence of the average kinetic energy on the source mass which is independent of the filter and the presence of the external Coulomb field. Previous systems [60,61] use very neutron-rich systems which skews the produced sources towards the neutron rich side. The systems studied in this

TABLE XII.: Average kinetic energy for He, Li, and C isotopes for four different theta bins.

isotope	theta bin 1 $0-45^\circ$	theta bin 2 $45-90^\circ$	theta bin 3 $90-135^\circ$	theta bin 4 $135-180^\circ$
^{3}He	17.54 ± 0.19	15.45 ± 0.13	14.39 ± 0.11	14.79 ± 0.21
^{4}He	13.12 ± 0.04	11.16 ± 0.03	13.38 ± 0.03	17.09 ± 0.05
^{6}He	17.59 ± 0.84	15.67 ± 0.44	21.21 ± 0.35	28.89 ± 0.48
^{6}Li	21.18 ± 0.29	16.16 ± 0.22	18.95 ± 0.19	22.14 ± 0.32
^{7}Li	22.09 ± 0.25	16.83 ± 0.19	20.71 ± 0.17	26.57 ± 0.24
^{8}Li	21.24 ± 0.81	20.02 ± 0.48	25.31 ± 0.31	32.58 ± 0.50
^{11}C	26.31 ± 0.57	15.17 ± 0.38	16.77 ± 0.49	15.95 ± 0.71
^{12}C	21.20 ± 0.22	13.12 ± 0.17	14.09 ± 0.23	14.43 ± 0.31
^{13}C	20.76 ± 0.31	13.23 ± 0.23	15.46 ± 0.30	17.29 ± 0.42
^{14}C	21.32 ± 0.31	13.91 ± 0.43	19.91 ± 0.55	18.55 ± 0.80

TABLE XIII.: The average kinetic energy for He, Li and C isotopes from reconstructed quasi-projectiles from the DIT+SMM calculation where no external Coulomb field is present during de-excitation.

isotope	theta bin 1 $0-45°$	theta bin 2 $45-90°$	theta bin 3 $90-135°$	theta bin 4 $135-180°$
^{3}He	13.65 ± 0.43	14.12 ± 0.28	13.12 ± 0.25	12.63 ± 0.37
^{4}He	12.84 ± 0.22	13.28 ± 0.14	13.18 ± 0.14	12.73 ± 0.18
^{6}He	17.62 ± 3.25	19.16 ± 1.16	17.38 ± 2.20	13.13 ± 3.68
^{6}Li	16.05 ± 0.65	17.03 ± 0.45	17.90 ± 0.45	17.14 ± 0.58
^{7}Li	16.91 ± 0.73	16.44 ± 0.56	18.52 ± 0.53	18.48 ± 0.72
^{8}Li	15.64 ± 2.04	20.94 ± 1.55	17.70 ± 1.38	25.46 ± 2.33
^{11}C	17.20 ± 1.02	17.42 ± 0.59	20.50 ± 0.65	18.77 ± 0.83
^{12}C	13.56 ± 0.46	15.30 ± 0.35	15.32 ± 0.34	14.35 ± 0.46
^{13}C	17.94 ± 1.16	17.34 ± 0.77	18.86 ± 0.69	17.32 ± 0.82
^{14}C	23.20 ± 1.16	18.55 ± 1.55	19.60 ± 1.84	17.93 ± 1.41

TABLE XIV.: Average kinetic energy for He, Li, and C for four different theta bins for the DIT+SMM calculation with no external Coulomb field and unfiltered.

isotope	theta bin 1 $0-45°$	theta bin 2 $45-90°$	theta bin 3 $90-135°$	theta bin 4 $135-180°$
^{3}He	13.32 ± 0.15	13.15 ± 0.10	13.65 ± 0.11	15.82 ± 0.20
^{4}He	13.36 ± 0.09	12.88 ± 0.06	13.25 ± 0.07	14.36 ± 0.10
^{6}He	15.80 ± 0.77	17.05 ± 0.57	16.81 ± 0.61	19.13 ± 0.95
^{6}Li	17.40 ± 0.25	15.61 ± 0.17	15.92 ± 0.16	18.24 ± 0.31
^{7}Li	17.44 ± 0.26	16.34 ± 0.18	16.29 ± 0.18	18.53 ± 0.30
^{8}Li	16.65 ± 0.72	16.08 ± 0.53	17.61 ± 0.54	18.24 ± 0.94
^{11}C	16.46 ± 0.39	15.63 ± 0.28	16.57 ± 0.32	16.56 ± 0.38
^{12}C	13.33 ± 0.21	13.00 ± 0.16	12.73 ± 0.15	13.97 ± 0.22
^{13}C	15.66 ± 0.40	15.52 ± 0.30	15.95 ± 0.34	15.23 ± 0.40
^{14}C	18.65 ± 0.40	17.31 ± 0.81	17.31 ± 1.08	17.51 ± 0.98

TABLE XV.: The average kinetic energy for He, Li and C isotopes from reconstructed quasi-projectiles from the DIT+SMM calculation where the ^{112}Sn target is present. This calculation was done at a break-up time of 50 fm/c and is filtered using the FAUST filter.

isotope	theta bin 1 $0-45°$	theta bin 2 $45-90°$	theta bin 3 $90-135°$	theta bin 4 $135-180°$
^{3}He	13.46 ± 0.25	13.57 ± 0.16	12.59 ± 0.14	11.67 ± 0.21
^{4}He	11.76 ± 0.11	12.37 ± 0.07	12.76 ± 0.07	12.56 ± 0.10
^{6}He	14.80 ± 1.12	16.21 ± 0.90	17.55 ± 1.03	20.30 ± 1.16
^{6}Li	15.10 ± 0.41	16.55 ± 0.26	18.15 ± 0.25	15.73 ± 0.30
^{7}Li	15.46 ± 0.44	17.16 ± 0.30	18.48 ± 0.27	18.10 ± 0.38
^{8}Li	20.04 ± 1.39	22.98 ± 0.99	18.65 ± 0.77	20.35 ± 1.01
^{11}C	17.05 ± 0.42	18.20 ± 0.28	19.11 ± 0.30	19.09 ± 0.46
^{12}C	14.29 ± 0.21	15.83 ± 0.17	15.93 ± 0.18	14.84 ± 0.24
^{13}C	15.06 ± 0.46	16.64 ± 0.36	17.88 ± 0.33	16.87 ± 0.45
^{14}C	14.84 ± 0.46	21.59 ± 1.03	16.19 ± 0.93	16.37 ± 1.37

work produce similar amounts of neutron-poor and neutron-rich sources. This could change the results as the behaviors of neutron-poor systems are not well understood.

TABLE XVI.: Average kinetic energy for He, Li, and C isotopes by reconstructed source mass.

isotope	^{30}S	^{32}S	^{34}S
^{3}He	14.55 ± 0.11	15.35 ± 0.15	15.83 ± 0.42
^{4}He	12.43 ± 0.04	12.68 ± 0.03	13.44 ± 0.07
^{6}He	21.85 ± 1.52	19.74 ± 0.58	20.68 ± 0.49
^{6}Li	17.04 ± 0.24	18.30 ± 0.20	19.71 ± 0.45
^{7}Li	18.60 ± 0.32	19.94 ± 0.20	21.87 ± 0.28
^{8}Li	23.56 ± 1.25	22.76 ± 0.49	24.40 ± 0.47
^{11}C	16.66 ± 0.40	19.99 ± 0.68	18.90 ± 2.00
^{12}C	13.04 ± 0.19	14.82 ± 0.18	17.92 ± 0.61
^{13}C	12.30 ± 0.36	14.80 ± 0.27	18.35 ± 0.55
^{14}C	13.35 ± 1.27	13.33 ± 0.48	17.87 ± 0.63

Since the average kinetic energy is comprised of two components in the energy spectra, the peak and the tail, it is of interest to extract out the parameters of these to determine if there is a trend within one of the components that is a driving factor for what is seen. In an attempt to quantify the differences between the kinetic energy spectra a Maxwellian distribution for surface emission is used [124–126]. The slope parameter from the Maxwellian distribution has most widely been used to calculate the nuclear temperature. This method follows from the Maxwell-Boltzmann relation

$$Yield \propto \exp^{-E_{kin}/kT} \tag{7.1}$$

where E is the center-of-mass kinetic energy, k is the Boltzmann constant, and T is the apparent temperature. Expanding this relation to include the Coulomb barrier one arrives at the equation

$$Yield \propto (E_{kin} - B) \exp^{(-(E_{kin}-B)/T_{app})} \tag{7.2}$$

where E_{kin} is the center-of-mass kinetic energy of the particles, B is the Coulomb barrier, and T_{app} is the apparent temperature. The parameters B and T_{app} are determined by fitting the data with formula 7.2. While this method is widely used to extract out information about the source temperature, this work is only concerned with the value as a means of comparison and no attempts will be made to make statesments to correlate the value of the T_{app} value presented in this dissertation and the nuclear temperature.

Examples of the fit of the Maxwellian distribution in equation 7.1 to the experimental kinetic energy spectrum of Li and C are given in Figure 48 and 49 respectively. In both of these figures it is shown that the Maxwellian distribution gives a reasonable fit to the experimental data. From these fits the parameters B and T_{app} are extracted. Table XVII gives the parameters for the three targets, ^{112,124}Sn and ^{nat}Au for comparison.

The Coulomb barrier parameter, B, within a given element and target, one can see the changes between the isotopes are small. This is indicative of the fragments being formed in similar environments. The largest changes come within the T_{app} parameter. For both the helium and lithium isotopes for all three targets, there is a stark increase in the temperature as one increases the mass. For carbon, the trend

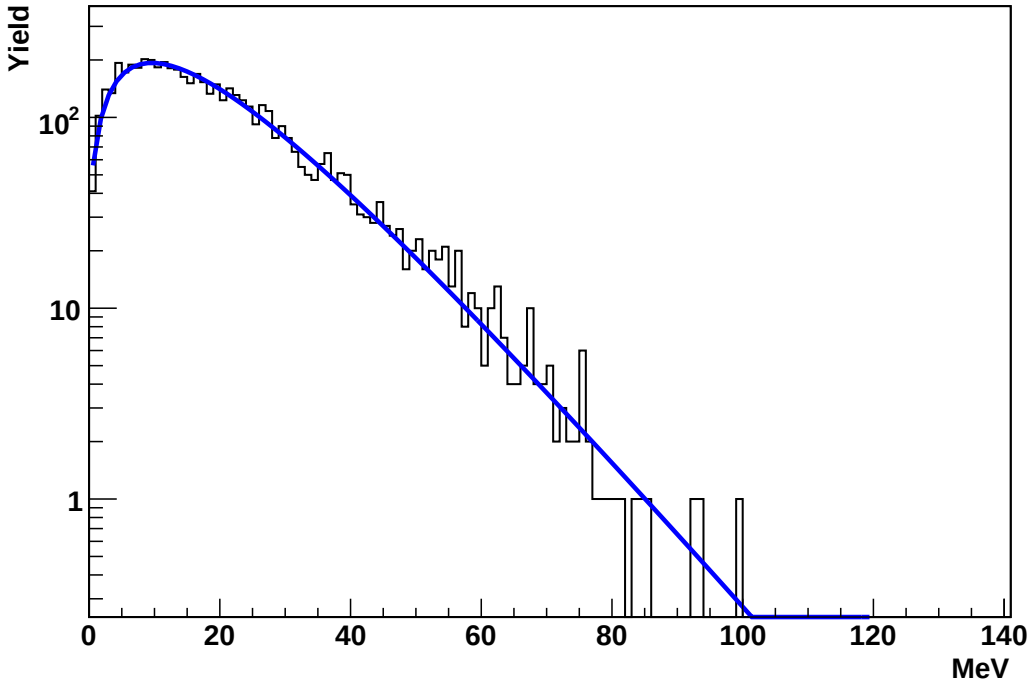

FIG. 48.: The kinetic energy spectrum for ^{7}Li in black. The Maxwellian fit as described in Equation 7.2 is presented in blue.

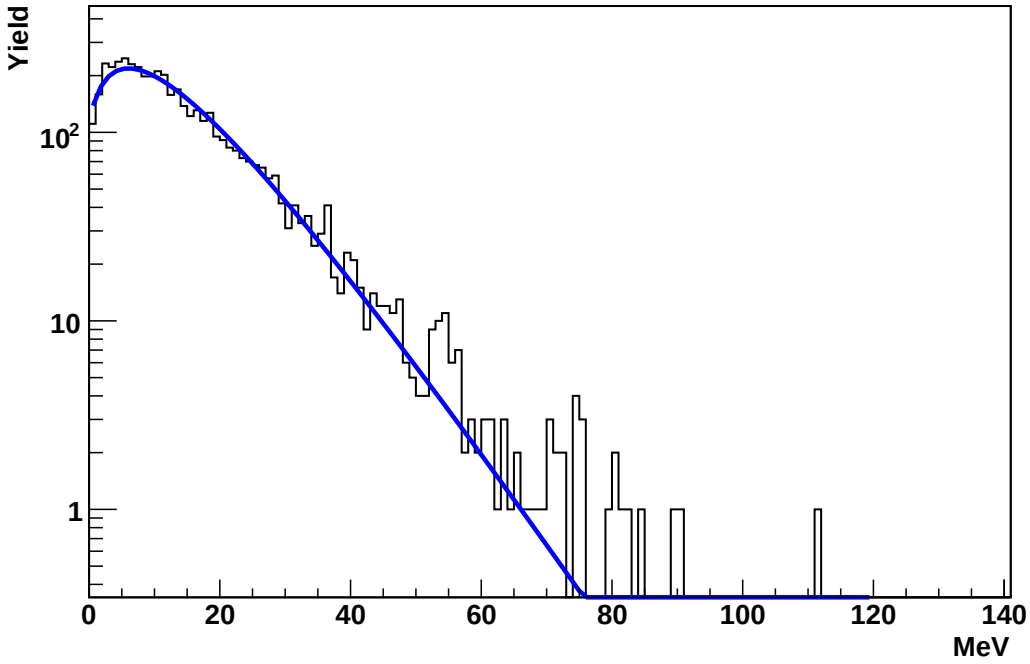

FIG. 49.: The kinetic energy spectrum for ^{12}C in black. The Maxwellian fit as described in Equation 7.2 is presented in blue.

TABLE XVII.: The Coulomb barrier parameter, B, and the apparent temperature parameter, T_{app} from the Maxwellian fit in Equation 7.2 for both Li and C isotopes for three systems ^{32}S + ^{112,124}Sn, ^{nat}Au.

	^{112}Sn		^{124}Sn		^{nat}Au	
isotope	B	T_{app}	B	T_{app}	B	T_{app}
^{3}He	0.06 ± 0.03	7.29 ± 0.03	0.04 ± 0.03	7.03 ± 0.03	0.06 ± 0.05	7.63 ± 0.04
^{4}He	0.93 ± 0.02	6.75 ± 0.01	0.99 ± 0.02	6.46 ± 0.01	0.91 ± 0.02	7.13 ± 0.01
^{6}He	0.43 ± 0.17	10.48 ± 0.15	0.45 ± 0.15	10.50 ± 0.14	0.40 ± 0.18	11.46 ± 0.15
^{6}Li	0.82 ± 0.08	9.38 ± 0.06	1.11 ± 0.09	9.00 ± 0.06	0.97 ± 0.11	10.04 ± 0.07
^{7}Li	0.85 ± 0.08	10.42 ± 0.06	0.85 ± 0.07	10.03 ± 0.05	0.60 ± 0.08	11.02 ± 0.06
^{8}Li	0.12 ± 0.13	12.14 ± 0.13	0.04 ± 0.11	11.66 ± 0.12	0.16 ± 0.12	12.93 ± 0.13
^{11}C	2.33 ± 0.30	9.39 ± 0.16	1.77 ± 0.23	8.53 ± 0.13	1.97 ± 0.32	10.46 ± 0.20
^{12}C	2.26 ± 0.15	7.98 ± 0.08	2.16 ± 0.13	7.34 ± 0.07	1.77 ± 0.14	8.86 ± 0.09
^{13}C	2.02 ± 0.21	8.18 ± 0.11	2.15 ± 0.19	7.91 ± 0.10	1.28 ± 0.16	8.71 ± 0.10
^{14}C	1.77 ± 0.38	8.62 ± 0.23	1.82 ± 0.32	8.32 ± 0.20	1.98 ± 0.36	9.87 ± 0.22

shows a small decrease to a flat behavior as one increases mass. Looking at each isotope and comparing between targets, the ^{112}Sn target has a slightly higher T_{app} than the ^{124}Sn target. This is easily explained from the source excitation energy distribution shown in Figure 50. When comparing the ^{124}Sn target to the ^{112}Sn target in Figure 50, the ^{112}Sn target has a slightly shifted energy spectrum that is consistently lower in excitation energy.

Because the excitation energy is lower it is expected that the source temperature would be lower as well. However, it is interesting to note that the ^{nat}Au target has a remarkably similar excitation energy spectrum as the ^{112}Sn target but consistently has a higher T_{app}. The explanation given to justify the difference in temperature between the ^{112}Sn and the ^{124}Sn targets by the differences in the excitation energy spectra does not hold for the ^{nat}Au case. If this justification could be used more broadly, then the ^{nat}Au target should produce similar T_{app} values to the ^{112}Sn target therefore the size of the target is an important factor in the excitation energy spectra.

In conclusion, the average kinetic energy extracted from a given system is dependent on the angle at which the particles were emitted. This observation is inherent in the break-up of the source regardless of the external Coulomb field and is postulated to be a direct result of the angular momentum. The average kinetic energy is also dependent on the N/Z of the emitting source. It is important to keep this in mind when comparing across systems to determine systematic trends as heavier systems tend to be neutron-rich and produce neutron-rich sources. Smaller systems near the $N = Z$ line have the ability to produce a greater proportion of proton-rich sources which could behave differently than their neutron-rich counterparts. The parameters of the Maxwell Boltzmann distribution show a large deviation within the slope parameter between the isotopes within a given element. The extracted apparent temperature values cannot be wholly explained by the excitation energy spectrum. The ^{nat}Au

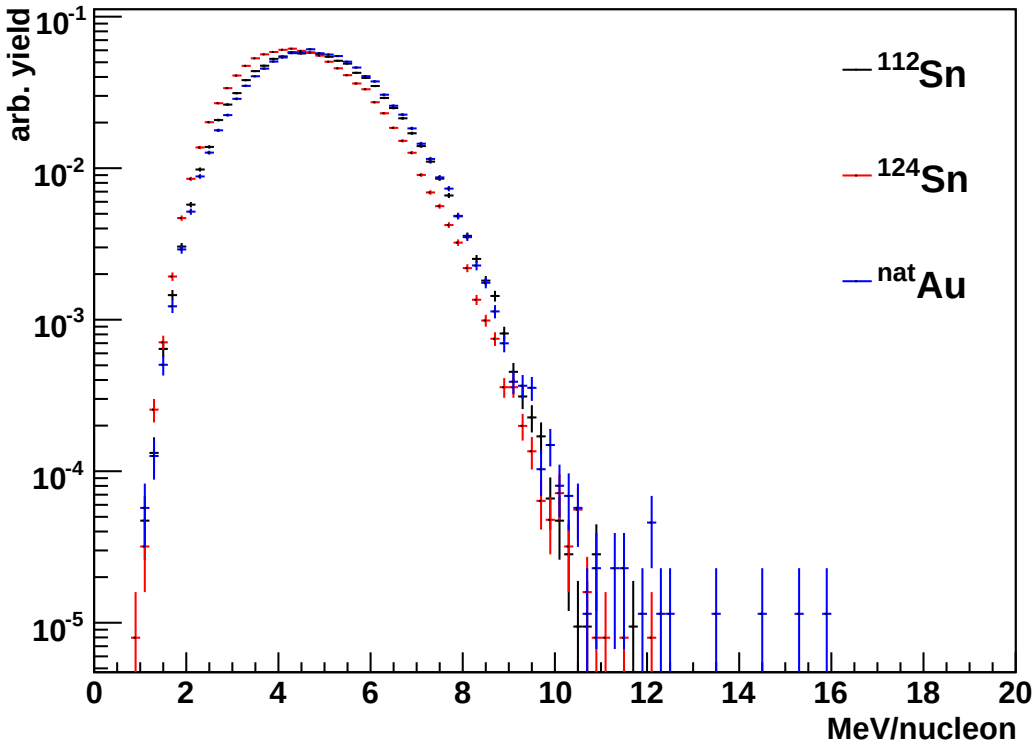

FIG. 50.: The excitation energy spectrum for the three systems ^{32}S + ^{112,124}Sn, ^{nat}Au in black, red, and blue respectively. Each spectrum was normalized to the total number of quasi-projectiles produced.

and ^{112}Sn target produce similar excitation energy spectra, but the T_{app} are different between these two targets. A possible explanation to this is that neutron-rich sources tend to produce higher excitation particles and the ^{nat}Au target does produce more neutron-rich sources than either of the two Sn targets.

CHAPTER VIII

CONCLUSIONS

The study of multifragmentation reactions, and subsequently the understanding of type II supernova explosions, has benefited from the diversity of experiments done in the intermediate energy domain. Theoretical studies have shown the multifragmentation reactions are an excellent platform for mimicking the environment of type II supernova explosions [41]. Type II supernova explosions are described by having a huge energy release of tens of MeV/nucleon. The excited system exhibits equilibrium behavior and can undergo statistical decay [39, 40]. It is hopeful that by studying the fragmentation of hot, dense nuclei in terrestrial experiments, the equation-of-state for supernova can be better constrained than current models [47, 62, 63, 65–68].

The work performed for this dissertation has tried to extend the boundaries of knowledge of how the source isospin affects the fragmentation pattern as well as the influence of an external Coulomb field on the fragmentation. This is analogous to the environment in supernova where there are many differing mass sources fragmenting and producing the observable signatures as well as having these sources being influenced by an external Coulomb field in their hot, dense environments. One projectile, ^{32}S, was reacted with three targets (^{112,124}Sn, ^{nat}Au) at 45 MeV/nucleon. The FAUST detector was essential for these reactions as it allows for a preferential selection on projectile fragmentation reactions. By having excellent isotopic resolution it allows for nearly complete (Z, A) reconstruction. Particles not detected included free neutrons which limit the reconstruction to only being able to obtain an observed mass of the quasi-projectile, which excludes any neutron evaporation. By selecting a $N = Z$ projectile, the evaporation of neutrons is minimal as it lies on the $N = Z$ line within the valley of stability. The reconstruction technique used along with the FAUST de-

tector provided fragments with negligible contamination of fragments produced from the target or other sources.

The source isospin has an effect on many observables. There is a clear transition in the charge distribution of emitted particles. A strong odd-even effect is present for neutron-poor sources that transitions to a more exponential or power law like distribution for neutron-rich sources. This observation is independent of the confidence with which the masses of the fragments are known. A study of the parallel velocity shows that there is an anisotropy about the center of the source which is a function of the external Coulomb field. Lastly it was found the slope of a particle's kinetic energy spectrum is a large contributor to the particles average kinetic energy.

While the previous paragraph summarizes the main conclusions of this thesis, further, more discriminating observations were made. Some basic observables were investigated using the hybrid DIT+SMM model. This model has done reasonably well at describing the average behavior of a fragmenting system [100, 101]. When reconstructing the source to where the sum of the charge collected is that of the beam, the DIT+SMM is able to reproduce the neutron-poor side of the N/Z distribution better than the neutron-rich side. This is most likely due to our lack of understanding of proton (neutron) transport and binding of nucleons within an interacting and fragmenting system.

By taking isotopically identified quasi-projectiles from the experimental data, there is a dependence of the fragmentation pattern on mass, charge, and source excitation energy. DIT+SMM grossly predicts the behaviors seen which suggests that the decay is highly statistical in nature. However, the results show that within the DIT+SMM framework the partitioning of the neutrons is not fully accounted for within neutron-rich systems. Differences in the fragment mass distributions between the neutron-poor ^{30}S source and the neutron-rich ^{34}S source indicate that the neu-

tron content of the hot primary fragments is potentially dependent on the symmetry energy but not the de-excitation itself. This can be inferred from looking at the mass distribution of heavier fragments such as nitrogen and oxygen as they show a greater sensitivity to the value of γ than their lighter counterparts. It is also clear that severely restricting the confidence in the isotopic identification to a 95% confidence over a broad definition shows little to no difference in the results. It was also found that the yield ratio of Y_{3H}/Y_{3He} as a function of source excitation energy changes as one changes the source isospin. This indicates that the summation of all sources is possibly only valid for charge yields.

By taking the fragments produced from isotopically identified quasi-projectiles, there is a clear anisotropy present in the particle emission as observed in the parallel velocities. The anisotropy can be described as particles being more likely emitted towards or away from the target. The more massive the isotope the more likely it is to be emitted towards the target. This appears to be a direct result of the Coulomb field as described through the DIT+SMM framework. The strength of the Coulomb interaction in the DIT+SMM framework is a function of the distance between the target and projectile, however, it appears it is not a straightforward $1/r$ dependence. More work will be needed to determine whether this can be a viable experimental probe to the break-up distance of the projectile from the target.

By taking the average kinetic energy of isotopes from a system, it is shown that the average kinetic energies are dependent on the angle at which the particles are emitted. This is inherent in the break-up of the source regardless of the external Coulomb field. These values are also dependent on the N/Z of the emitting source. This is an important observation when comparing across systems to determine systematic trends as heavier systems tend to be neutron-rich and produce more neutron-rich sources. The behaviors may change as one moves to more neutron-poor

sources. The shapes of the excitation energy spectra can be fit with a simple Maxwell Boltzmann distribution. The parameters of this distribution show a large deviation within the slope parameter between the isotopes within a given element. By looking at this slope parameter, there is a target dependence which is not explained solely by the source excitation spectrum. A possible explanation to this is that neutron-rich sources tend to produce higher excitation particles and the ^{nat}Au target does produce more neutron-rich sources than either of the two Sn targets.

By extracting the average kinetic energy of each isotope from its kinetic energy spectrum for the ^{32}S + ^{112}Sn at 45 MeV/nucleon system, there is a clear difference in the average kinetic energy value as a function of angle of emission. This is explained as a result of angular momentum dependencies rather than through a presence of an external Coulomb filed as evidenced by DIT+SMM theoretical calculations.

In conclusion, it is important to study and understand both the neutron-poor and neutron-rich sources produced in a nuclear reaction. From the results presented in this dissertation, it is clear that behaviors start to change when moving from the neutron-rich ^{34}S to the neutron-poor ^{30}S source. It would be useful in future studies to probe more neutron-poor sources to begin to map out the effects on general observables as one moves into the neutron-poor side of the valley of stability.

By being able to analyze isotopically identified sources, it is possible to begin to correct deficiencies in the theoretical models for supernova explosions. By looking at neutron-rich and neutron-poor hot nuclei, these studies can help correct current supernova models which only take into account neutron-rich nuclei in a cold or slightly excited state. Also, as multifragmentation reactions provide a look at the environment of the fragments from a decaying nucleus, the usage of isolated nuclei in supernova calculations can be changed as well. One of the biggest contributions, though, is to use the isotopically identified sources to give a more accurate mass distribution

of the produced fragments in return giving a more complete ensemble instead of the "average" nucleus approach. These refinements in our theoretical understanding of fragmenting nuclei can constrain calculations and increase our understanding of supernova explosions. It is hopeful that the results presented here can pave way for more studies which focus on isotopically-identified, neutron-poor sources to expand our knowledge and create a more coherent picture with regards to the transitions within the entire mass range of nuclei produced in nuclear reactions.

REFERENCES

[1] D. Gross, Rep. Prog. Phys. **53**, 605 (1990).

[2] E. Bauge, A. Elmaani, R. A. Lacey, J. Lauret, N. Ajitanand, D. Craig, M. Cronqvist, E. Gualtieri, S. Hannuschke, T. Li, B. Llope, T. Reposeur, A. V. Molen, G. Westfall, J. Winfield, J. Yee, S. Yennello, A. Nadasen, R. Tickle, and E. Norbeck, Phys. Rev. Lett. **70**, 3705 (1993).

[3] D. Bowman, G. Peaslee, N. Carlin, R. de Souza, C. Gelbke, W. Gong, Y. Kim, M. Lisa, W. Lynch, L. Phair, M. Tsang, C. Williams, N. Colonna, K. Hanold, M. McMahan, G. Wozniak, and L. Moretto, Phys. Rev. Lett. **70**, 3534 (1993).

[4] R. Charity, L. Sobotka, N. Robertson, D. Saranties, J. Dinius, C. Gelbke, T. Glasmacher, D. Handzy, W. Hsi, M. Huang, W. Lynch, C. Montoya, G. Peaslee, C. Schwarz, and M. Tsang, Phys. Rev. C **52**, 3126 (1995).

[5] B. Harmon, J. Pouliot, J. Lopez, J. Suro, R. Knop, Y. Chan, D. DiGregorio, and R. Stockstad, Phys. Lett. B **235**, 234 (1990).

[6] M. Gyulassy, K. Frankel, and H. Stocker, Phys. Lett. B **110**, 185 (1982).

[7] J. Cugnon and D. L'Hote, Nucl. Phys. A **397**, 519 (1983).

[8] J. Lopez and J. Randrup, Nucl. Phys. A **491**, 477 (1989).

[9] J. Aichelin and H. Stocker, Phys. Lett. B **176**, 14 (1986).

[10] L. Tassan-Got and C. Stephan, Nucl. Phys. A **524**, 121 (1991).

[11] V. Viola, W. Hsi, K. Kwiatkowski, G. Wang, D. Bracken, H. Breuer, J. Brzychczyk, Y. Chu, E. Cornell, E. R. Foxford, F. Gimeno-Nogues, D. Ginger,

S. Gushue, M. Huang, R. Korteling, R. Legrain, W. Lynch, K. Morley, E. Pollacco, E. Ramakrishnan, L. Remsberg, D. Rowland, M. Tsang, C. Volant, H. Xi, S. Yennello, and N. Yoder, Nucl. Phys. A **626**, 287 (1997).

[12] J. Cugnon, Nucl. Phys. A **462**, 751 (1987).

[13] G. Wang, K. Kwiatkowski, , V. Viola, W. Bauer, and P. Danielewicz, Phys. Rev. C **53**, 1811 (1996).

[14] R. Laforest, D. Dore, J. Pouliot, R. Roy, C. St-Pierre, G. Auger, P. Bricault, S. Groult, E. Plagnol, and D. Horn, Nucl. Phys. A **568**, 350 (1994).

[15] D. Dore, L. Beaulieu, R. Laforest, J. Laville, O. Lopez, J. Pouliot, R. Regimbart, R. Roy, J. Steckmeyer, and C. St-Pierre, Phys. Lett. B **323**, 103 (1994).

[16] A. Schuttauf, W. Kunze, A. Worner, M. Bergemann-Blaich, T. Blaich, D. Bowman, R. Charity, A. Cosmo, A. Ferrero, C. Gelbke, C. Gross, W. Hsi, J.Hubele, G. Imme, I. Iori, J. Jempter, P. Kreutz, G. Kunde, V. Lindenstruth, and M. Lisa, Nucl. Phys. A **607**, 457 (1996).

[17] U. Lynen, A. collaboration, R. Bassini, M. Bergemann-Blaich, T. Blaich, H. Emiling, A. Ferrero, S. Fritz, S. Gaff, C. Gross, G. Imme, I. Iori, U. Kleinevoss, G. Kunde, W. Kunze, V. Lindenstruth, M. Mahi, A. Moroni, T. Mohlenkamp, and W. Muller, Nucl. Phys. A **630**, 176c (1998).

[18] L. Moretto and G. Wozniak, Annu. Rev. Nucl. Part. Sci. **379** (1993).

[19] B. Li, C. Ko, and W. Bauer, Int. J. Mod. Phys. E **7**, 147 (1998).

[20] J. Dempsey, R. Charity, L. Sobotka, G. Kunde, S. Gaff, C. Gelbke, T. Glasmacher, M. Huang, R. Lemmon, W. Lynch, L. Manduci, L. Martin, M. Tsang,

D. Agnihotri, B. Djerroud, W. Schroder, W. Skulski, J. Toke, and W. Friedman, Phys. Rev. C **54**, 1710 (1996).

[21] G. Kunde, S. Gaff, C. Gelbke, T. Glasmacher, M. Huang, R. Lemmon, W. Lynch, L. Manduci, L. Martin, M. Tsang, W. Friedman, J. Dempsey, R. Charity, L. Sobotka, D. Agnihotri, B. Djerroud, W. Schroder, W. Skulski, J. Toke, and K. Wyrozebski, Phys. Rev. Lett. **77**, 2897 (1996).

[22] S. D. Gupta and G. Westfall, Phy. Today **46**, 34 (1993).

[23] I. Tanihata, Prog. Part. Nucl. Phys. **35**, 505 (1995).

[24] B. Noren, B. Jakobsson, A. Kristiansson, A. Oskarsson, M. Westenius, J. Julien, V. Bellini, R. Fonte, T. Johansso, J. Thun, and C. Guet, Nucl. Phys. A **489**, 763 (1988).

[25] S. Yennello and *et. al.*, *Advances in Nuclear Dynamics 2* (Plenum Press, New York, 1996).

[26] B. Li and S. Yennello, Phys. Rev. C **52**, R1746 (1995).

[27] H. Muller and B. Serot, Phys. Rev. C **52**, 2072 (1995).

[28] V. Baran, M. Colonna, M. D. Toro, and A. Larionov, Nucl. Phys. A **632**, 287 (1998).

[29] P. Chomaz and F. Gulminelli, Phys. Lett. B **447**, 221 (1999).

[30] H. Xu, M. Tsang, T. Liu, X. Liu, W. Lynch, W. Tan, A. V. Molen, G. Verde, A. Wagner, H. Xi, C. Gelbke, L. Beaulieu, B. Davin, Y. Larochelle, T. Lefort, R. de Souza, R. Yanez, V. Viola, R. Charity, and L. Sobotka, Phys. Rev. Lett. **85**, 716 (2000).

[31] M. Veselsky, R. Ibbotson, R. Laforest, E. Ramakrishnan, D. Rowland, A. Ruangma, E. Winchester, E. Martin, and S. Yennello, Phys. Rev. C **62**, 041605 (2000).

[32] A. Hirsch, A. Bujak, J. Finn, L. Gutay, R. Minich, N. Porile, R. Scharenberg, B. Stringfellow, and F. Turkot, Phys. Rev. C **29**, 508 (1984).

[33] R. Green, R. Korteling, and K. Jackson, Phys. Rev. C **29**, 1806 (1984).

[34] H. Gutbrod, K. Kampert, B. Kolb, A. Poskanzer, H. Ritter, R. Schicker, and H. Schmidt, Phys. Rev. C **42**, 640 (1990).

[35] K. Doss, H. Gustafsson, H.H, B. Kol, H. Lohner, B. Ludewigt, A. Poskanzer, T. Renner, H. Riedsel, H. Ritter, A. Warwick, and H. Wieman, Phys. Rev. C **32**, 116 (1985).

[36] R. Charity, M. McMahan, G. Wozniak, R. McDonald, L. Moretto, D. Saranties, L. Sobotka, G. Guarino, A. Pantaleo, L. Fiore, A. Gobbi, and K. Hildenbrand, Nucl. Phys. A **483**, 371 (1988).

[37] J. Bondorf, A. Botvina, A. Iljinov, I. Mishustin, and K. Sneppen, Physics Reports **257**, 133 (1995).

[38] A. Steiner, M. Prakash, J. Lattimer, and P. Ellis, Acta Phys. Hung. A **25**, 203 (2006).

[39] G. Brown, H. Bethe, and G. Baym, Nucl. Phys. A **375**, 481 (1982).

[40] H. Bethe, Rev. Mod. Phys. **62**, 801 (1990).

[41] A. Botvina and I. Mishustin, Phys. Rev. C **72**, 048801 (2005).

[42] A. Vertes, S. Nagy, and Z. Klencsar, editors, *Handbook of Nuclear Chemistry* (Kluwer Academic Publishers, The Netherlands, 2003).

[43] K. Chen, Z. Fraenkel, G. Friedlander, J. Grover, J. Miller, and Y. Shimamoto, Phys. Rev. **166**, 949 (1968).

[44] D. L'Hote and J. Cugnon, Int. Rev. of Nuc. Phys., World Scientific **38**, 1 (1991).

[45] G. Montarou, J. Marroncle, J. Alard, J. Augerat, N. Bastid, P. Charmensat, P. Dupieux, L. Fraysse, M. Parizet, A. Rahmani, R. Babinet, C. Cavata, M. Demoulins, H. Fanet, J. Gosset, D. L'Hote, M. Lemaire, B. Lucas, J. Poitou, O. Valette, F. Brochard, P. Gorodetzky, C. Racca, and J. Cugnon, Phys. Rev. C **47**, 2764 (1993).

[46] J. Randrup, Nucl. Phys. A **327**, 490 (1979).

[47] R. Buras, M. Rampp, H.-T. Janka, and K. Kifonidis, AA **3**, 1049 (2006).

[48] E. Uehling and G. Uhlenbeck, Phys. Rev. **43**, 552 (1933).

[49] B. Li and G. Gross, Nucl. Phys. A **554**, 257 (1993).

[50] C. Gregoire, B. Remaud, F. Sebille, L. Vinet, and Y. Raffray, Nucl. Phys. A **465**, 317 (1987).

[51] L. Nordheim, Proc. R. Soc. London **119**, 317 (1928).

[52] A. Botvina, A. Iljinov, and I. Mishustin, Nucl. Phys. A **507**, 649 (1990).

[53] N. Ballaize, O. Lopez, J. Wieleczko, D. Cussol, G. Auger, C. O. Bacri, F. Bocage, B. Borderie, R. Bougault, B. Bouriquet, R. Brou, P. Buchet, A. Buta, J. Charvet, A. Chbihi, J. Colin, R. Dayras, N. D. Cesare, A. Demeyer, and D. Dore, Nucl. Phys. A **709**, 367 (2002).

[54] G. Peilert, J. Konopka, H. Stocker, W. Greiner, M. Blann, and M. Mustafa, Phys. Rev. C **46**, 1457 (1992).

[55] A. Ono, H. Horiuchi, T. Maruyama, and A. Ohnishi, Phys. Rev. Lett. **68**, 2898 (1992).

[56] M. Tsang, C. Gelbke, X. Liu, W. Lynch, W. Tan, G. Verde, H. Xu, W. Friedman, R. Donangelo, S. Sousa, C. Das, S. D. Gupta, and D. Zhabinsky, Phys. Rev. C **64**, 054615 (2001).

[57] G. Souliotis, M. Veselsky, G. CHubarian, L. Trache, A. Keksis, E. Martin, D. Shetty, and S. Yennello, Phys. Rev. Lett. **91**, 022701 (2003).

[58] W. Tan, B. Li, R. Donangelo, C. Gelbke, M. van Goethem, X. Liu, W. Lynch, S. Souza, M. Tsang, G. Verde, A. Wagner, and H. Xu, Phys. Rev. C **64**, 051901 (2001).

[59] V. Baran, M. Colonna, M. D. Toro, V. Greco, M. Zielinska-Pfabe, and H. Wolter, Physics of Atomic Nuclei **66**, 1460 (2003).

[60] S. Hudan, R. Alfaro, B. Davin, Y. Larochelle, H. Xu, L. Beaulieu, T. Lefort, R. Yanez, R. de Souza, R. Charity, L. Sobotka, T. Liu, X. Liu, W. Lynch, R. Shomin, W. Tan, M. Tsang, A. V. Molen, A. Wagner, and H. Xi, Phys. Rev. C **71**, 054604 (2005).

[61] T. Liu, W. Lynch, M. van Goethem, X. Liu, R. Shomin, W. Tan, M. Tsang, G. Verde, A. Wagner, H. Xi, H. Xu, W. Friedman, S. Sousa, R. Donangelo, L. Beaulieu, B. Davin, Y. Larochelle, T. Lefort, R. de Souza, R. Yanez, V. Viola, R. Charity, and L. Sobotka, Europhys. Lett. **74**, 806 (2006).

[62] D. Lamb, J. Lattimer, C. Pethick, and D. Ravenhall, Nucl. Phys. A **360**, 459 (1981).

[63] J. Lattimer, C. Pethick, D. Ravenhall, and D. Lamb, Nucl. Phys. A **432**, 646 (1985).

[64] J. Lattimer and F. Swesty, Nucl. Phys. A **535**, 331 (1991).

[65] H. Shen, H. Toki, K. Oyamatsu, and K. Sumiyoshi, Nucl. Phys. A **637**, 435 (1998).

[66] C. Ishizuka, A. Ohnishi, and K. Sumiyoshi, Nucl. Phys. A **723**, 517 (2003).

[67] A. Botvina and I. Mishustin, Phys. Lett. B **584**, 233 (2004).

[68] A. Aprahamian, K. Langanke, and M. Wiescher, Prog. Part. Nucl. Phys. **54**, 535 (2005).

[69] A. Botvina and I. Mishustin, Nucl. Phys. A **843**, 98 (2010).

[70] F. Gimeno-Nogues, D. Rowland, E. Ramakrishnan, S. Ferro, S. Vasal, R. Gutierrez, R. Olsen, Y.-W. Lui, R. Laforest, H. Johnston, and S. Yennello, Nucl. Instr. and Meth. A **399**, 94 (1997).

[71] http://www.caen.it/getattach.php?mod=c257&obj=mn&id=1817, caen s.p.a, 2009.

[72] http://www.caen.it/getattach.php?mod=n568b&obj=mn&id=1610, caen s.p.a, 2009.

[73] http://www-esd.fnal.gov/esd/catalog/main/ces/cbd8210.pdf.

[74] http://www.lecroy.com/lrs/dsheets/222.htm, lecroy corporation, 2009.

[75] http://www.lecroy.com/lrs/, lecroy corporation, 1997.

[76] http://www.lecroy.com/lrs/dsheets/3420.htm, lecroy corporation, 2009.

[77] http://www.lecroy.com/lrs/dsheets/428.htm, lecroy corporation, 2009.

[78] http://www.lecroy.com/lrs/dsheets/2551.htm, lecroy corporation, 2009.

[79] http://www.lecroy.com/lrs/dsheets/688.htm, lecroy corporation, 2009.

[80] http://www.lecroy.com/lrs/dsheets/623.htm, lecroy corporation, 2009.

[81] EG & G Ortec, 100 Midland Rd., Oakridge, TN, 37830, *EG&G Ortec RD 2000 Dual Fast Rate Divider Manual*.

[82] http://www.jlab.org/ moller/e_upgrade/pdf/754ds.pdf, 2009.

[83] http://www.phillipsscientific.com/pdf/7164ds.pdf, phillips scientific, 2009.

[84] http://www.canberra.com, canberra, 2009.

[85] B. Davin, R. de Souza, R. Yanez, Y. Larochelle, R. Alfaro, H. Xu, A. Alexander, K. Bastin, L. Beaulieu, J. Dorsett, G. Fleener, L. Gelovani, T. Lefort, J. Poehlman, R. Charity, L. Sobotka, J. Elson, A. Wagner, T. Liu, and X. Liu, Nucl. Instr. and Meth. A **473**, 302 (2001).

[86] B. Davin, R. de Souza, R. Yanez, Y. Larochelle, R. Alfaro, H. Xu, A. Alexander, K. Bastin, L. Beaulieu, J. Dorsett, G. Fleener, L. Gelovani, T. Lefort, J. Poehlman, R. Charity, L. Sobotka, J. Elson, A. Wagner, T. Liu, X. Liu, W. Lynch, L. Morris, R. Shomin, W. Tan, M. Tsang, G. Verde, and J. Yurkon, Nucl. Instrum. Methods Phys. Res. A **473**, 302 (2001).

[87] L. May, Z. Kohley, S. Wuenschel, K. Hagel, S. Soisson, G. Souliotis, B. Stein, R. Wada, and S. Yennello, To Be Submitted. .

[88] F. Hubert, R. Bimbot, and H. Gauvin, At. Data Nucl. Data Tables **46**, 1 (1990).

[89] G. F. Knoll, *Radiation Detection and Measurement, Second Edition* (John Wiley & Sons, Inc., New York, 1989).

[90] L. Tassan-Got, Nucl. Instr. and Meth. B **194**, 503 (2002).

[91] M. Parlog, B. Borderie, M. Rivet, G. Tabacaru, A. Chbihi, M. Elouardi, N. L. Neindre, O. Lopez, E. Plagnol, L. Tassan-Got, G. Auger, C. O. Bacri, N. Bellaize, F. Bocage, R. Bougault, B. Bouriquet, R. Brou, P. Buchet, J. L. Charvet, J. Colin, and et al., Nucl. Instr. and Meth. A **482**, 674 (2002).

[92] M. Parlog, B. Borderie, M. Rivet, G. Tabacaru, A. Chbihi, M. Elouardi, N. L. Neindre, O. Lopez, E. Plagnol, L. Tassan-Got, G. Auger, C. O. Bacri, N. Bellaize, F. Bocage, R. Bougault, B. Bouriquet, R. Brou, P. Buchet, J. L. Charvet, J. Colin, and et al., Nucl. Instr. and Meth. A **482**, 693 (1992).

[93] P. Mastinu, P. Milazzo, M. Bruno, M. D'Agostino, and L. Manduci, Nucl. Instr. and Meth. A **338**, 419 (1994).

[94] D. Horn, G. Ball, A. Galindo-Uribarri, E. Jagberg, R. Walker, R. Laforest, and J. Pouliot, Nucl. Instr. and Meth. A **320**, 273 (1992).

[95] E. D. Filippo, G. Lanzano, A. Pagano, S. Urso, . Berthier, J. Charvet, R. Dayras, R. Legrain, R. Lucas, C.Mazur, E. Pollacco, J. Sauvestre, C. Volant, C. Beck, and B. Djerroud, Nucl. Instr. and Meth. A **342**, 527 (1994).

[96] N. Colonna, G. Wozniak, A. Veeck, W. Skulski, G. Goth, L. Manduci, P. Milazzo, and P. Mastinu, Nucl. Instr. and Meth. A **321**, 529 (1992).

[97] D. Stracener, D. Saranties, L. Sobotka, J. Elson, J. Hood, Z. Majka, V. Abenante, A. Chbihi, and D. Hensley, Nucl. Instr. and Meth. A , 485 (1990).

[98] Y. Larochelle, L. Beaulieu, B. Djerroud, D. Dore, P. Gendron, E. Jalbert, R. Laforest, J. Pouliot, R. Roy, M. Samri, and C. St-Pierre, Nucl. Instr. and Meth. A **348**, 167 (1994).

[99] A. Wagner, W. Tan, K. Chalut, R. Charity, B. Davin, Y. Larochelle, M. Lennek, T. Liu, X. Liu, W. Lynch, A. Ramos, R. Shomin, L. Sobotka, R. de Souza, M. Tsang, G. Verde, and H. Xu, Nucl. Instr. and Meth. A **456**, 290 (2001).

[100] D. Rowland, Ph.D. dissertation, Texas A&M University (2000).

[101] A. Keksis, Ph.D. dissertation, Texas A&M University (2007).

[102] A. Badala, R. Barbera, A. Palmeri, G. Pappalardo, and F. Riggi, Phys. Rev. C **48**, 633 (1993).

[103] R. Dalitz, Philosophical Magazine **44**, 1068 (1953).

[104] F.Gramegna, U. Abbondanno, A. Bonasera, M. Bruno, G. Casini, S. Cavallaro, M. Chiari, M. D'Agostino, A. Lanchais, G. Margagliotti, P. Mastinu, P. Milazzo, A. Moroni, A. Nannini, A. Ordine, R. Ricci, F. Tonetto, L. Travaglini, G. Vannini, and L. Vannucci, Fizika B **12**, 39 (2003).

[105] J. Randrup, Nucl. Phys. A **397**, 319 (1978).

[106] W. Schroder and J. Huizenga, Annu. Rev. Nucl. Part. Sci. **27**, 465 (1977).

[107] N. Bohr, Nature **137**, 344 (1936).

[108] A. Botvina, A. Iljinov, I. Mishustin, J. Bondorf, R. Donangelo, and K. Sneppen, Nucl. Phys. A **475**, 663 (1987).

[109] A. Botvina and I. Mishustin, Phys. Rev. C **63**, 061601 (2001).

[110] A. Botvina, private communication. (2009).

[111] S. Wuenschel, Ph.D. dissertation, Texas A&M University (2009).

[112] C. Knott, S. Albergo, Z. Caccia, C. Chen, S. Costa, H. Crawford, M. Cronqvist, J. Engelage, P. Ferrando, R. Fonte, L. Greiner, T. Guzik, A. Insolia, F. Jones, P. Lindstrom, J. W. Mitchell, R. Potenza, J. Romanski, G. Russo, A. Soutoul, O. Testard, C. Tull, C. Tuve, C. Waddington, W. Webber, and J. Wefel, Phys. Rev. C **53**, 347 (1996).

[113] A. LeFevre, G. Auger, M. Begemann-Blaich, N. Bellaize, R. Bittiger, F. Bocage, B. Borderie, R. Bougault, B. Bouriquet, J. Charvet, A. Chbihi, R. Dayras, D. Durand, J. Frankland, E. Galichet, D. Gourio, D. Guinet, S. Hudan, G. Imme, P. Lautesse, F. Lavaud, R. Legrain, O. Lopez, J. Lukasik, U. Lynen, W. Muller, L. Nalpas, H. Orth, E. Plagnol, G. Raciti, E. Rosato, A. Saija, C. Schwarz, W. Seidel, C. Sfienti, B. Tamain, W. Trautmann, A. Trzcinski, K. Turzo, E. Vient, M. Bigilante, C. Volant, B. Zwieglinski, and A. Botvina, Phys. Rev. Lett. **94**, 162701 (2005).

[114] J. Iglio, D. Shetty, S. Yennello, G. Souliotis, M. Jandel, A. Keksis, S. Soisson, B. Stein, S. Wuenschel, and A. Botvina, Phys. Rev. C **74**, 024605 (2006).

[115] D. Henzlova, A. Botvina, K. Schmidt, V. Henzel, P. Napolitani, and M. Ricciardi, J. Phys. G: Nucl. Part. Phys. **37**, 085010 (2010).

[116] D. Shetty, G. Souliotis, S. Galanopoulos, Z. Kohley, S. Soisson, B. Stein, S. Wuenschel, and S. Yennello, J. Phys. G: Nucl. Part. Phys. **36**, 075103 (2010).

[117] L. Chen, C. Ko, and B. Li, Phys. Rev. C **68**, 017601 (2003).

[118] L. Chen, C. Ko, and B. Li, Phys. Rev. C **69**, 054606 (2004).

[119] L. Chen, V. Greco, C. Ko, and B. Li, Phys. Rev. Lett. **90**, 162701 (2003).

[120] L. Chen, V. Greco, C. Ko, and B. Li, Phys. Rev. C **68**, 014605 (2003).

[121] L. Chen, C. Ko, and B. Li, Nucl. Phys. A **729**, 809 (2003).

[122] A. Botvina, M. Bruno, M. D'Agostino, and D. Gross, Phys. Rev. C **59**, 3444 (1999).

[123] A. Botvina, private communication. (2010).

[124] S. Albergo, S. Costa, E. Constanzo, and A. Rubbino, Nuovo Cimento **89**, 1 (1985).

[125] M. Tsang, W. Lynch, H. Xi, and W. Friedman, Phys. Rev. Lett. **78**, 3836 (1997).

[126] D. Durand, E. Suraud, and B. Tamain, *Nuclear Dynamics in the Nucleonic Regime* (Institute of Physics Publishing, Bristol and Philadelphia, 2001).

APPENDIX A

MONTE CARLO SIMULATIONS OF THE FAUST ARRAY

Previous simulations of the FAUST array use the Monte Carlo technique to randomize where a particle hits within the array. However, these previous models assumed that each ring of FAUST was on a flat plane and only varied in the X and Y direction, ignoring the curvature introduced by the fact that FAUST is a square projected on a sphere. This is a reasonable assumption as measurements within the detector will only be off by 0.01cm at its largest variation. It is possible to remove the variation introduced by this assumption by representing each detector as vectors in 3-D space. The procedure is as follows.

First, it is assumed that each detector is a perfect square defined by four corners, 1-4, arranged in a clockwise fashion. Each point is defined by coordinates x_i, y_i, and z_i. For each detector, the coordinates were obtained from the original mechanical drawings. A function of a line between point 1 and point 2 is constructed.

$$f(x_1) = x_1 + (x_2 - x_1)t_1 \tag{A.1}$$

$$f(y_1) = y_1 + (y_2 - y_1)t_1$$

$$f(z_1) = z_1 + (z_2 - z_1)t_1$$

A second function is constructed between point 3 and point 4.

$$fx_2 = x_4 + (x_3 - x_4)t_1 \tag{A.2}$$

$$fy_2 = y_4 + (y_3 - y_4)t_1$$

$$fz_2 = z_4 + (z_3 - z_4)t_1$$

In equations A.1 and A.2 t_1 is a random number between 0 and 1. Using equation A.1 as an example, if t_1 is set to 0, than point 1 is returned. If t_1 is set to 1, then point 2 is returned. At values between 0 and 1, it represents the distance traveled along the line vector constructed. The same value of t_1 is used in both equation A.1 and A.2 to define the end points of a vector that is perpendicular to f_1 and f_2. This vector is define with point 5 and pint 6 and vector g is constructed between these points.

$$g(x) = x_5 + (x_6 - x_5)t_2 \tag{A.3}$$

$$g(y) = y_5 + (y_6 - y_5)t_2$$

$$g(z) = z_5 + (z_6 - z_5)t_2$$

A new random number between 0 and 1 is generated for t_2. When using t_2 in A.3, the resulting $g(x)$, $g(y)$, and $g(z)$ gives a random point on the surface of a given detector. This in turn gives a random θ and ϕ for the particle in question. In the laboratory frame, θ and ϕ are found through the equations

$$\tan\phi = \frac{x}{y} \tag{A.4}$$

and

$$\cos\theta = \frac{z}{\sqrt{x^2 + y^2 + z^2}}. \tag{A.5}$$

Figure 51 show the efficiency of this method in reproducing a representation in phase space of the FAUST array. This figure shows a 3-D side view of the FAUST array. In this view, it is easy to show the curvature that each ring has due to its nature of being a square projected on a sphere.

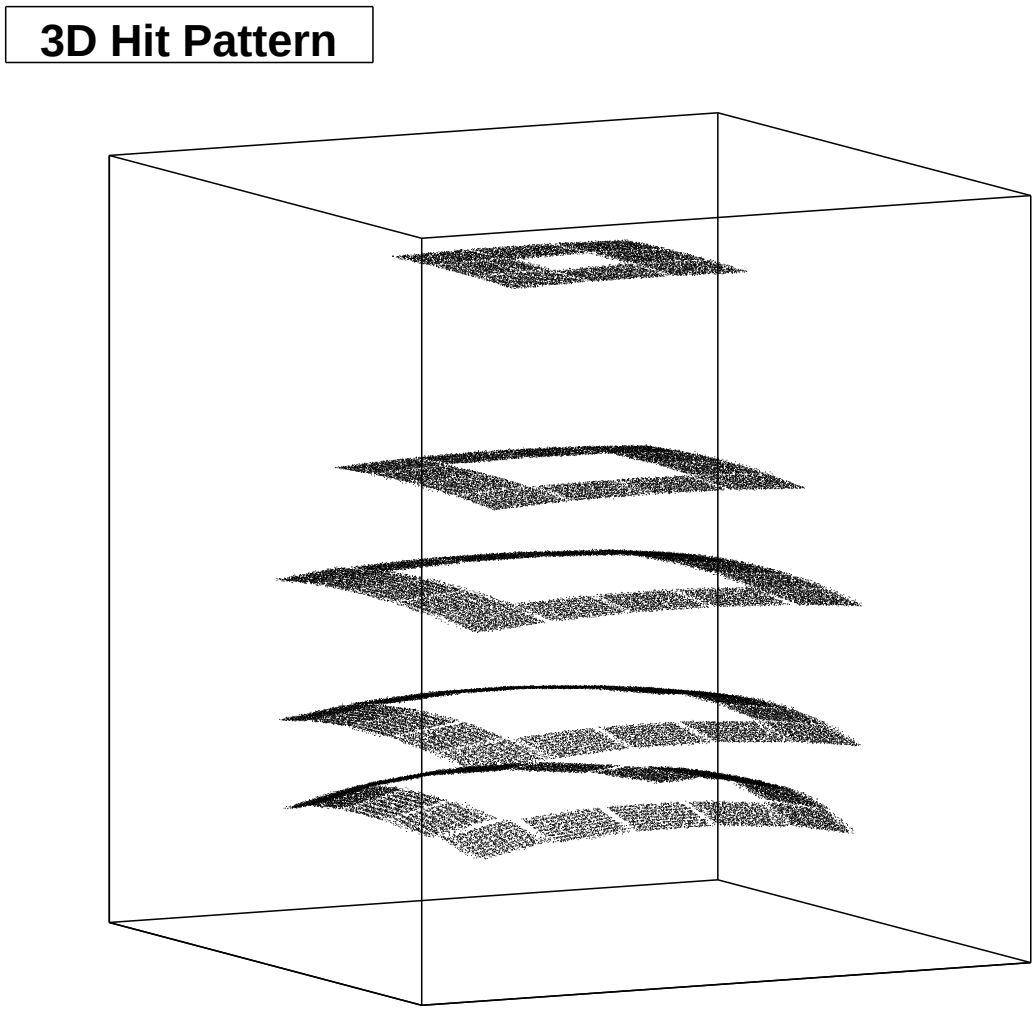

FIG. 51.: 3-D representation of the FAUST array.

APPENDIX B

FRAGMENTATION WITH NO A CONSTRAINT

It is natural to question the effect of placing a 95% confidence cut on each isotope within a selected event. In Chapter V a fragmentation analysis was done to show that the source N/Z has an effect on many different fragmentation signatures. Below is several of the graphics presented in Chapter V. When comparing it shows that the 95% confidence cut provides little to no change to the observables. This lends credence to the idea that regardless of the percentages between those isotopically identified with a 95% confidence and those in generally isotopically identified (see Table IV) do not provide a good representation between the observables and the percentage being "cut out" due to the nature of the overlapping Gaussians in a non-uniform environment. Only the experimental data has this isotopic confidence cut placed on it as the identity of fragments from the theoretical calculation is absolutely known.

Figure 52 shows the mass distribution for sources for the ^{32}S + ^{112}Sn at 45 MeV/nucleon system. The yield per event of the neutron-rich sources is much lower than for the systems with the A constraint.

One of the largest differences is seen Figure 56 within the N isotopes. When no isotopic constraint is placed within the data, the ^{14}N aligns itself more with the calculation that it does with the 95% confidence cut.

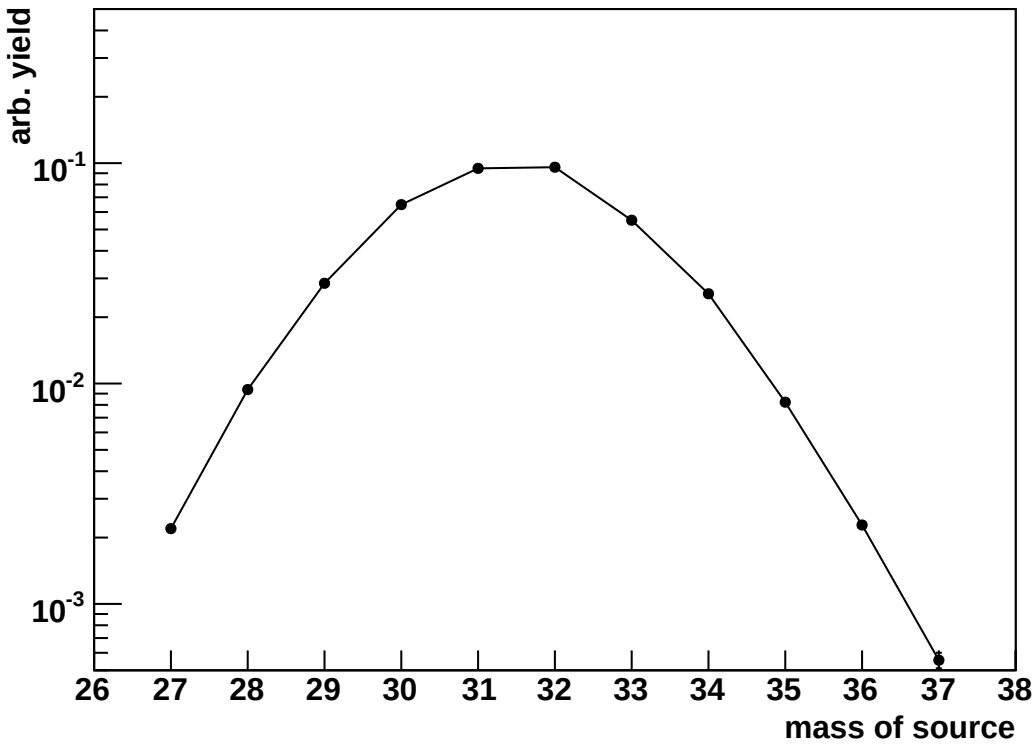

FIG. 52.: The mass distribution of sources for the $^{32}S + ^{112}Sn$ system for reconstructed sources. No isotopic confidence cut is placed within the data.

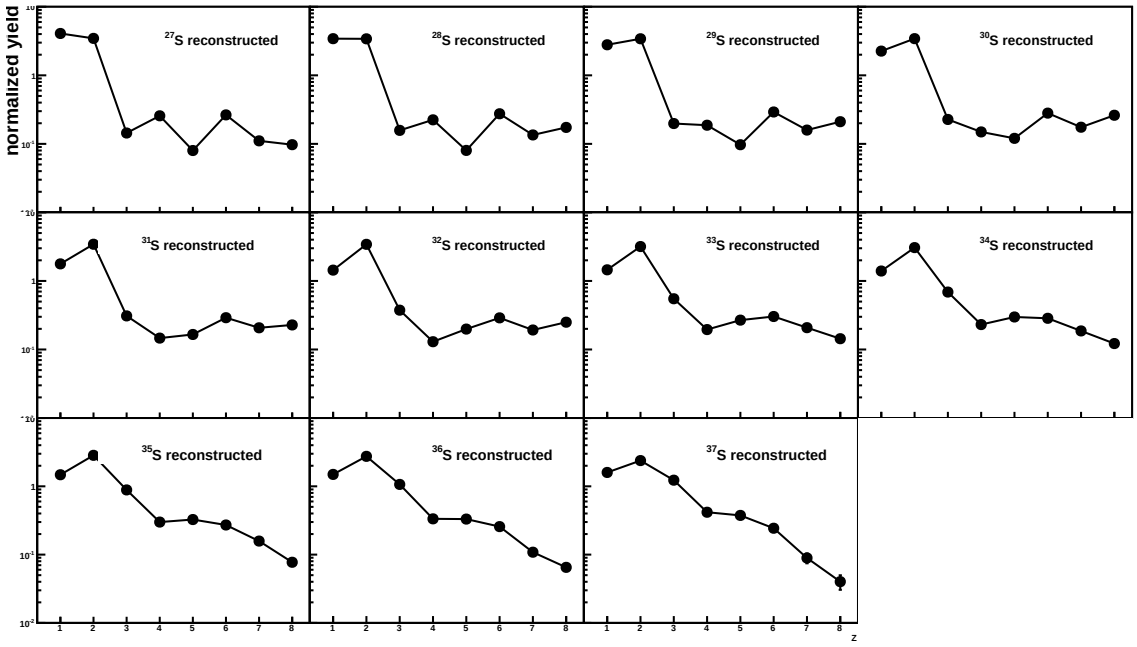

FIG. 53.: The charge distribution for ^{27}S - ^{37}S sources. The yield of each element is normalized to the number of sources produced for each source mass. No isotopic confidence cut is placed within the data.

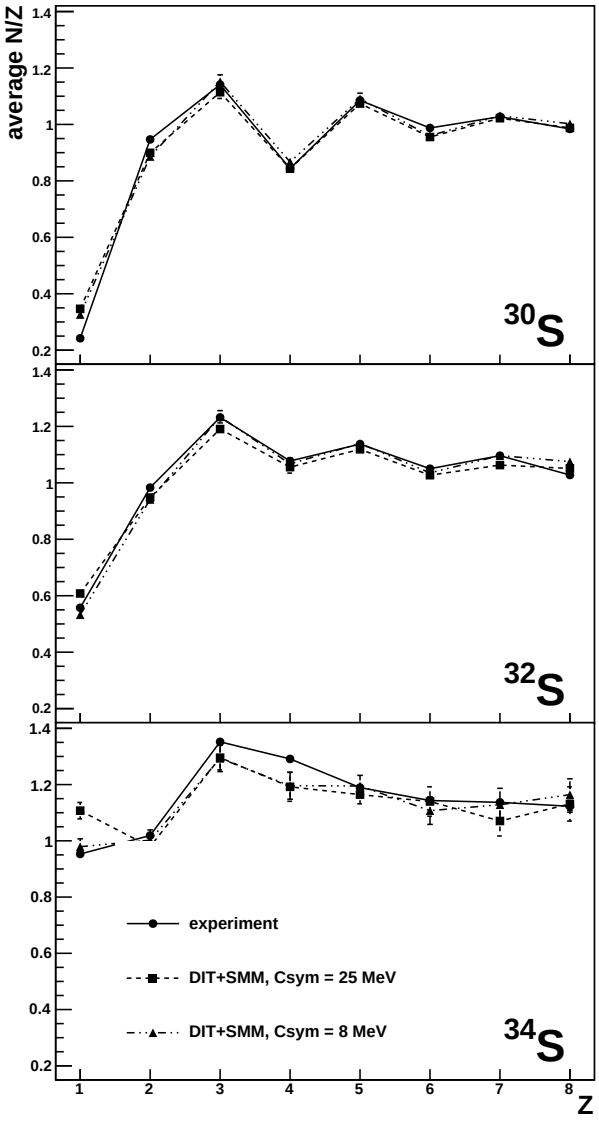

FIG. 54.: The average N/Z distribution for the sources ^{30,32,34}S from the reaction ^{32}S + ^{112}Sn at 45 MeV/nucleon. No isotopic confidence cut is placed within the data. Two DIT+SMM calculations are present: $\gamma = 25$ MeV and $\gamma = 8$ MeV.

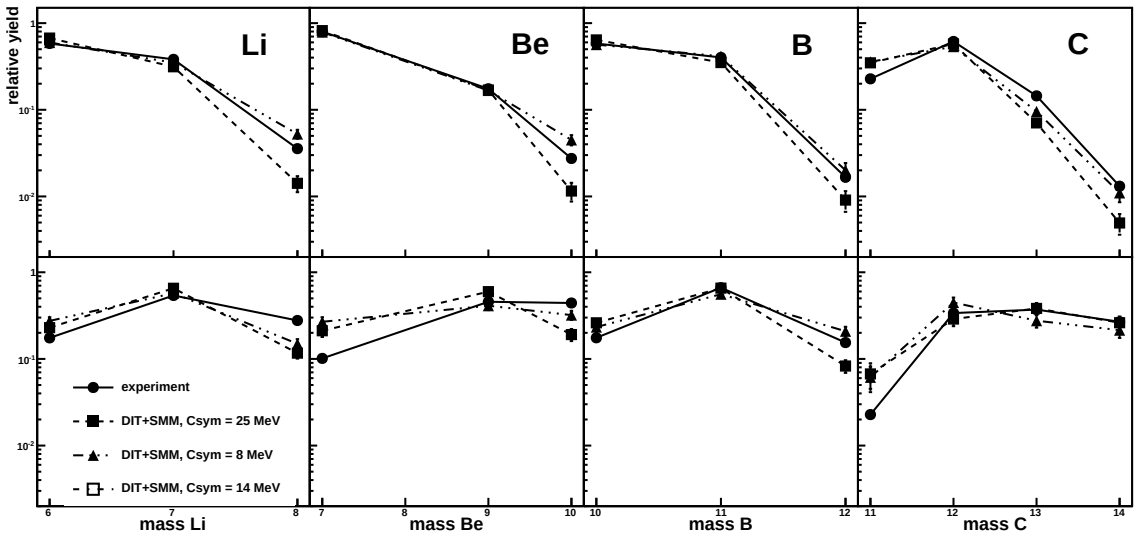

FIG. 55.: The mass distribution for Li - C isotopes for the reaction ^{32}S + ^{112}Sn at 45 MeV/nucleon. No isotopic confidence cut is placed within the data. Two DIT+SMM calculations are present: $\gamma = 25$ MeV and $\gamma = 8$ MeV.

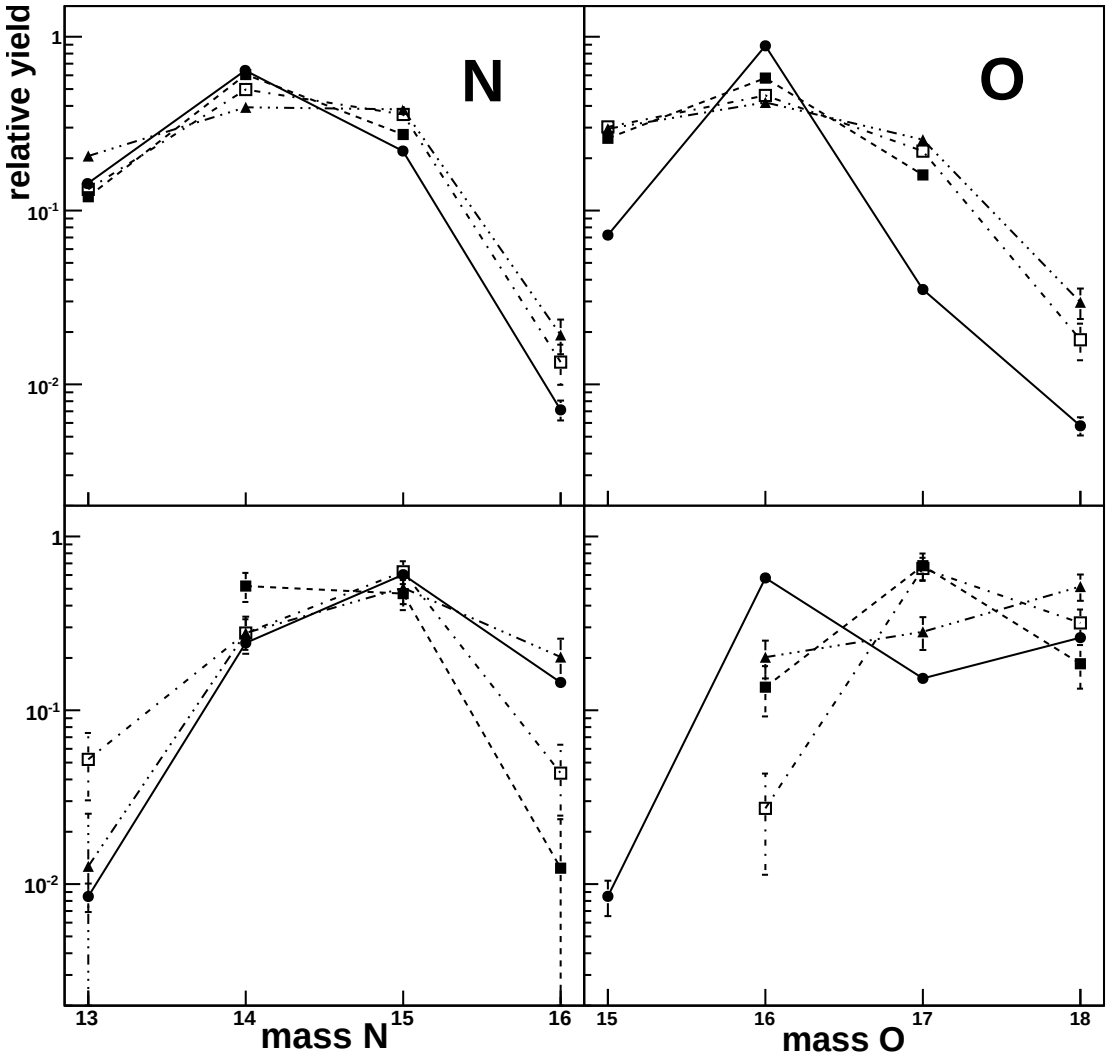

FIG. 56.: The mass distribution for N - O isotopes for the reaction ^{32}S + ^{112}Sn at 45 MeV/nucleon. No isotopic confidence cut is placed within the data. Three DIT+SMM calculations are present: $\gamma = 25$ MeV, $\gamma = 8$ MeV, and $\gamma = 14$ MeV.

APPENDIX C

GAUSSIAN FITS

Taking the fits assuming two gassians into consideration and looking at them qualitatively, one can garner information about the relationship between the two Gaussian components. In Figures 57 - 67, the experimental data plus the DIT+SMM distance calculations are also given. The reader is cautioned to not compare the Gaussian method to the ratio method described in Chapter VI. The ratio method is governed by the assumption of things being emitted in a positive or negative direction, i.e. centered around zero. The Gaussian method discussed here, the point where the forward and backward Gaussian cross is not dependent on a given parallel velocity value.

Beginning with Helium (Figures 57 - 58), the relative size and shape of the front Gaussian and the back Gaussian among the calculations do not vary dramatically. For the Lithium and Beryllium isotopes (Figures 59 - 62), as one increases the distance, for example 20 fm - 40 fm, there is a growth in the backward component in relation to the forward component. For Boron and Carbon isotopes (Figures 63 - 67), there is an increase in the forward component as one increases the distance. However, the comparison between the forward and backward components for Boron and Carbon isotopes is not as dramatic as it is for the Lithium and Beryllium isotopes. For the Boron and Carbon isotopes, once a large distance is reached (between 40 fm and 60 fm) the difference becomes slight or is not present.

These observations show that the anisotropic behavior is present and is a function of the distance between the target and projectile. The difference between the forward and backward components as one increases the distance diminishes as one

increases mass approaching the largest fragment in an event. While the discrete distance calculations do show a difference, no single calculation can reproduce the entire range present in the experimental data. Distances between 20 fm and 40 fm show the greatest promise due to the experimental data usually lying between the trends shown at these distances.

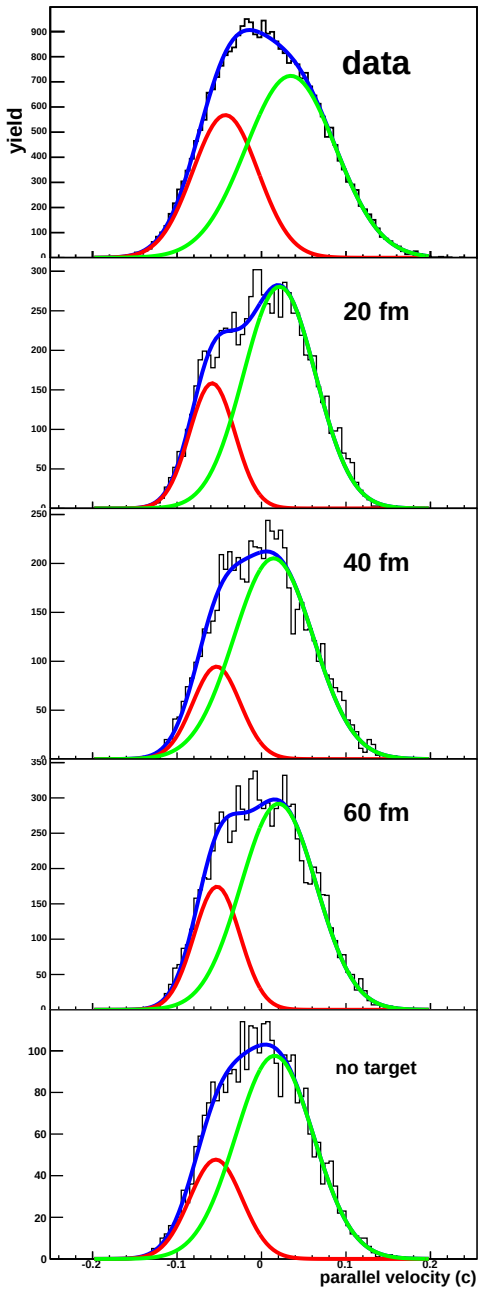

FIG. 57.: Parallel velocity plot for ^{3}He for the system ^{32}S + ^{112}Sn at 45 MeV/nucleon. From top to bottom are the experimental data, the DIT+SMM calculation at a fixed starting distance of 20 fm, 40 fm, and 60 fm, and the bottom panel is for no external Coulomb field (no target present for de-excitation).

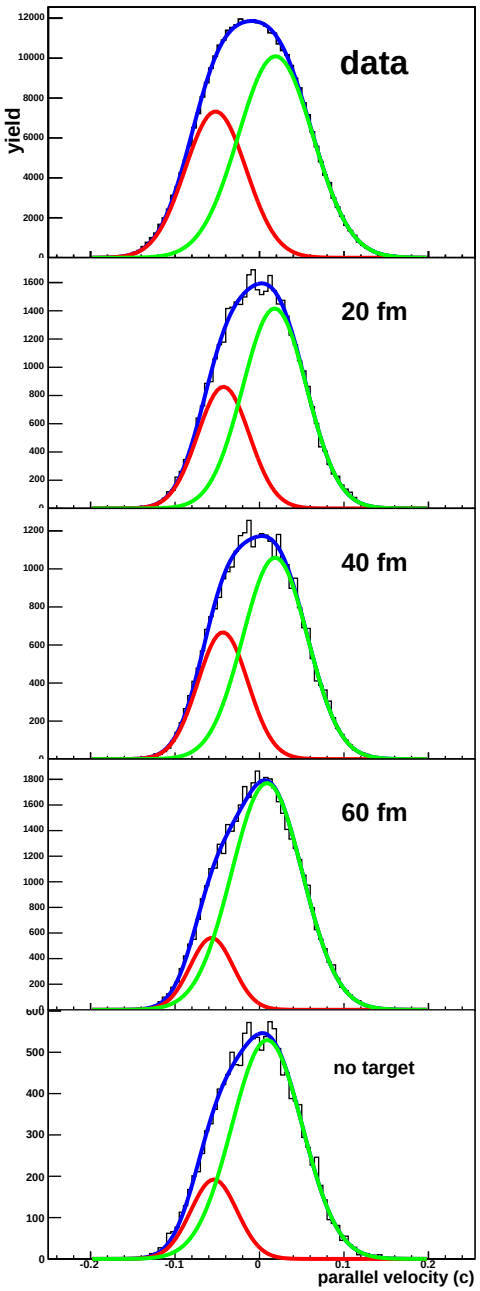

FIG. 58.: Parallel velocity plot for ^{4}He for the system ^{32}S + ^{112}Sn at 45 MeV/nucleon. From top to bottom are the experimental data, the DIT+SMM calculation at a fixed starting distance of 20 fm, 40 fm, and 60 fm, and the bottom panel is for no external Coulomb field (no target present for de-excitation).

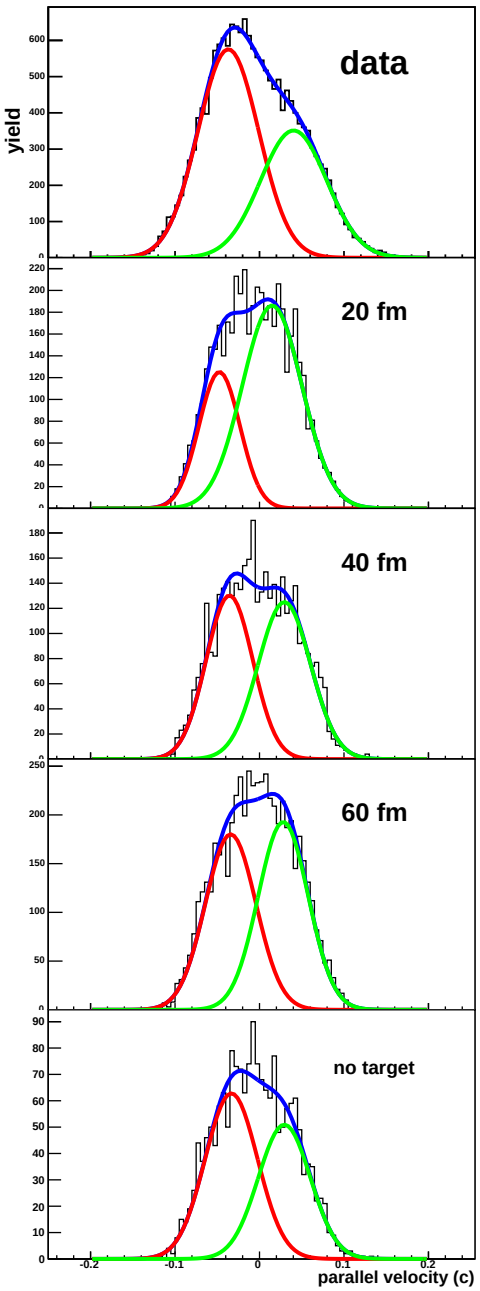

FIG. 59.: Parallel velocity plot for ^{6}Li for the system ^{32}S + ^{112}Sn at 45 MeV/nucleon. From top to bottom are the experimental data, the DIT+SMM calculation at a fixed starting distance of 20 fm, 40 fm, and 60 fm, and the bottom panel is for no external Coulomb field (no target present for de-excitation).

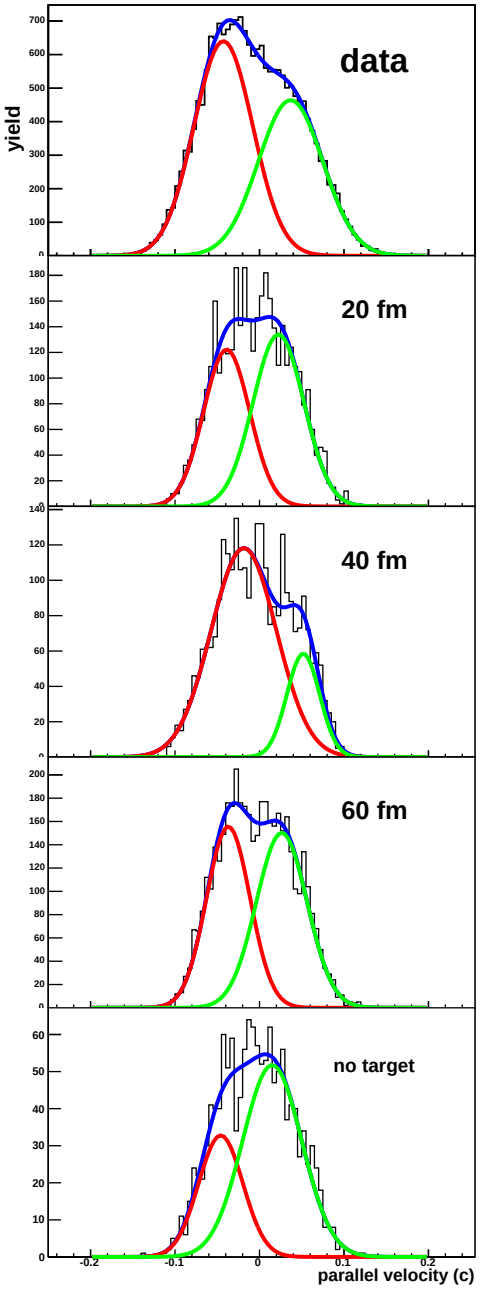

FIG. 60.: Parallel velocity plot for ^{7}Li for the system ^{32}S + ^{112}Sn at 45 MeV/nucleon. From top to bottom are the experimental data, the DIT+SMM calculation at a fixed starting distance of 20 fm, 40 fm, and 60 fm, and the bottom panel is for no external Coulomb field (no target present for de-excitation).

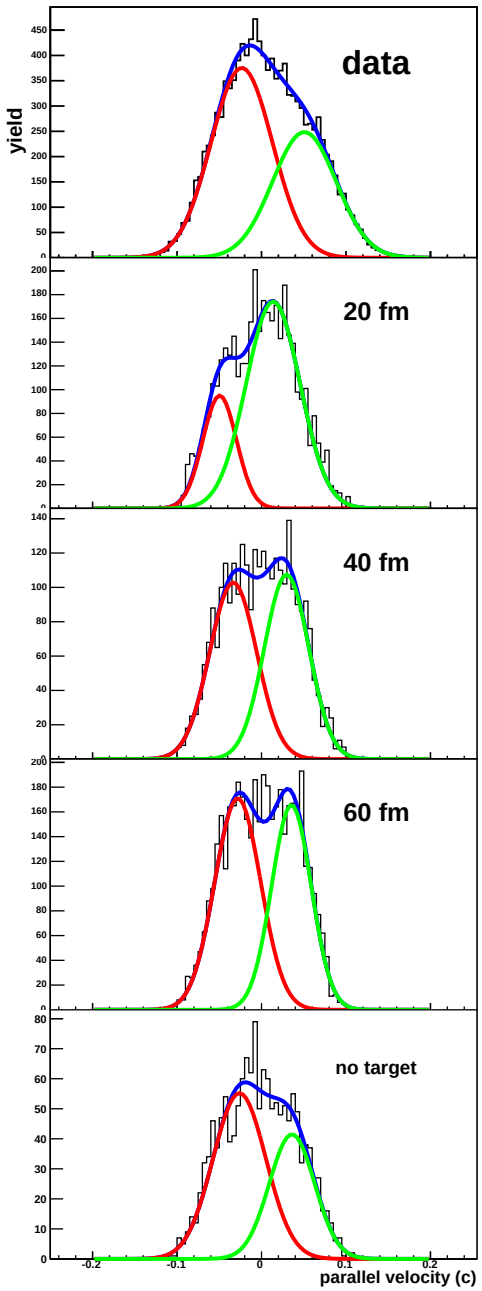

FIG. 61.: Parallel velocity plot for ^{7}Be for the system ^{32}S + ^{112}Sn at 45 MeV/nucleon. From top to bottom are the experimental data, the DIT+SMM calculation at a fixed starting distance of 20 fm, 40 fm, and 60 fm, and the bottom panel is for no external Coulomb field (no target present for de-excitation).

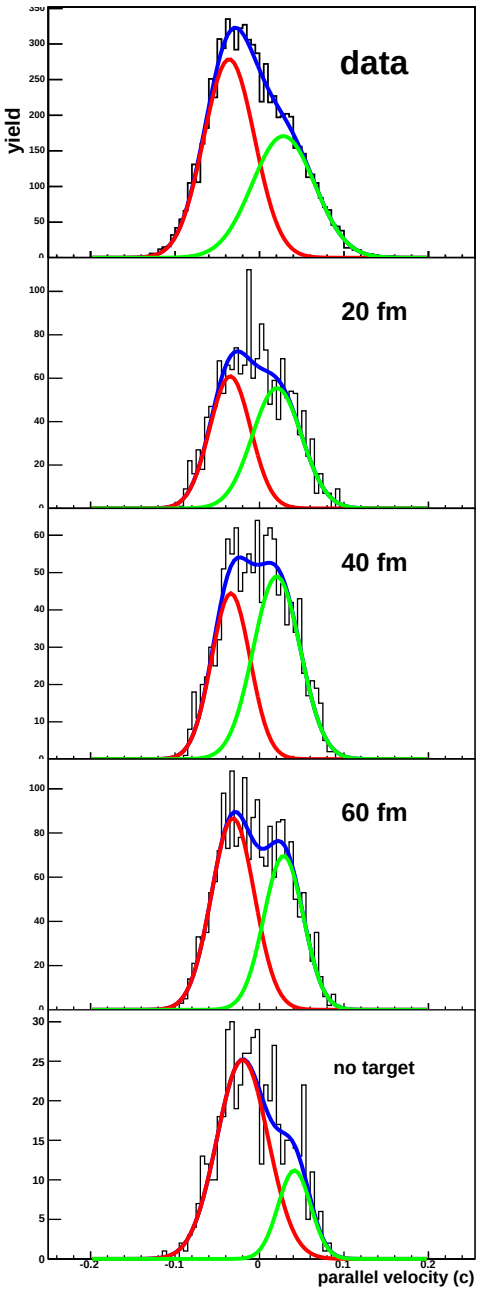

FIG. 62.: Parallel velocity plot for ^{9}Be for the system ^{32}S + ^{112}Sn at 45 MeV/nucleon. From top to bottom are the experimental data, the DIT+SMM calculation at a fixed starting distance of 20 fm, 40 fm, and 60 fm, and the bottom panel is for no external Coulomb field (no target present for de-excitation).

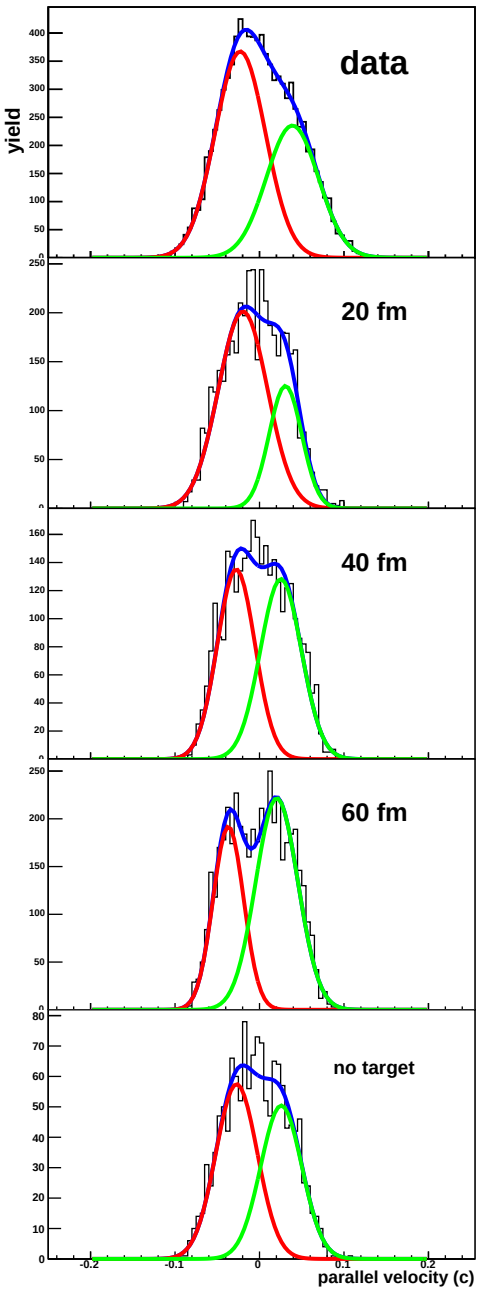

FIG. 63.: Parallel velocity plot for ^{10}B for the system ^{32}S + ^{112}Sn at 45 MeV/nucleon. From top to bottom are the experimental data, the DIT+SMM calculation at a fixed starting distance of 20 fm, 40 fm, and 60 fm, and the bottom panel is for no external Coulomb field (no target present for de-excitation).

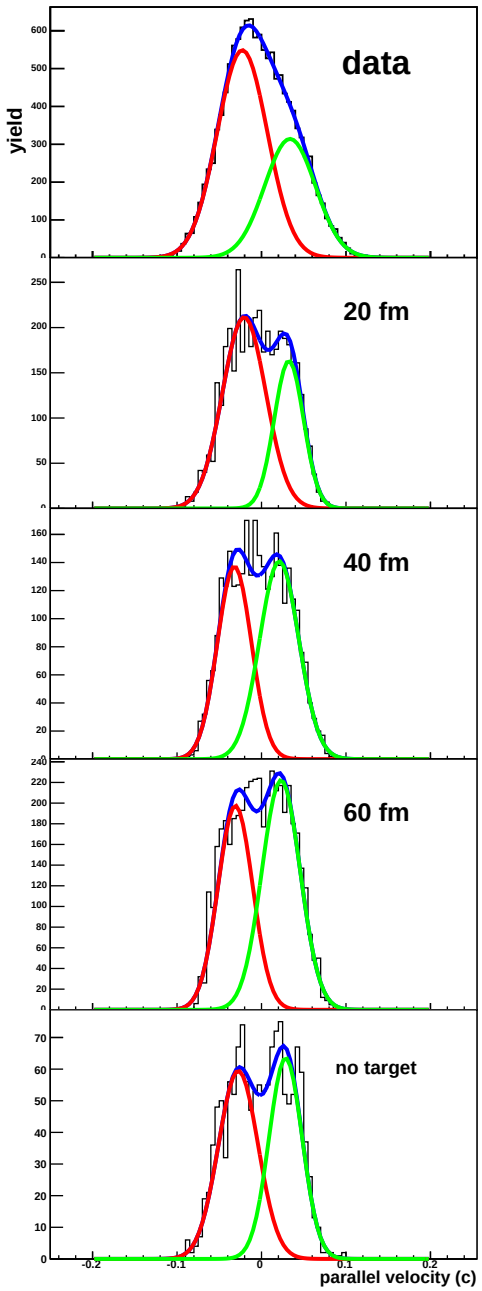

FIG. 64.: Parallel velocity plot for ^{11}B for the system ^{32}S + ^{112}Sn at 45 MeV/nucleon. From top to bottom are the experimental data, the DIT+SMM calculation at a fixed starting distance of 20 fm, 40 fm, and 60 fm, and the bottom panel is for no external Coulomb field (no target present for de-excitation).

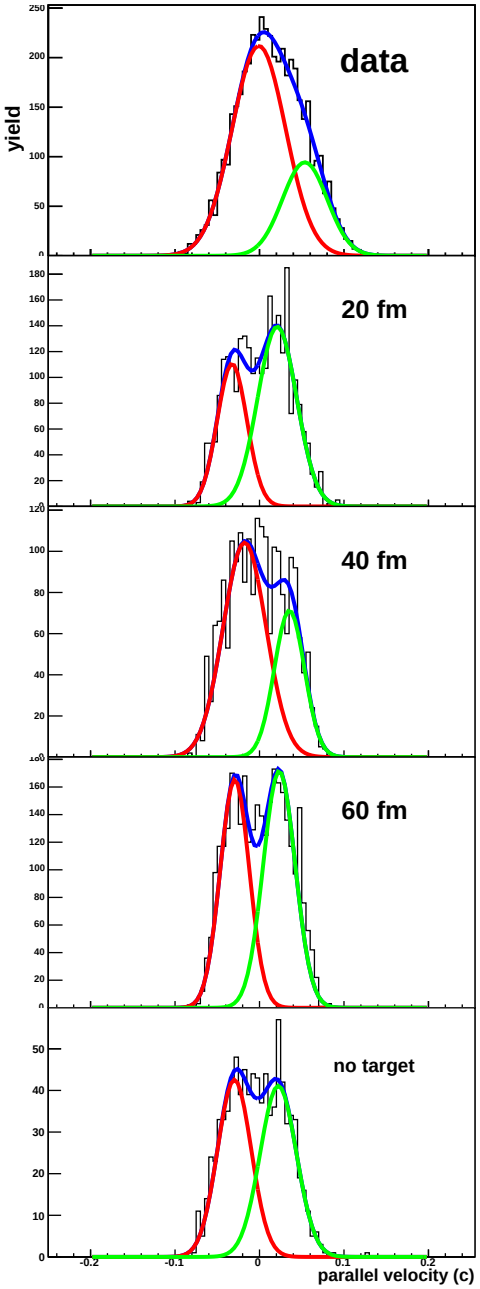

FIG. 65.: Parallel velocity plot for ^{11}C for the system ^{32}S + ^{112}Sn at 45 MeV/nucleon. From top to bottom are the experimental data, the DIT+SMM calculation at a fixed starting distance of 20 fm, 40 fm, and 60 fm, and the bottom panel is for no external Coulomb field (no target present for de-excitation).

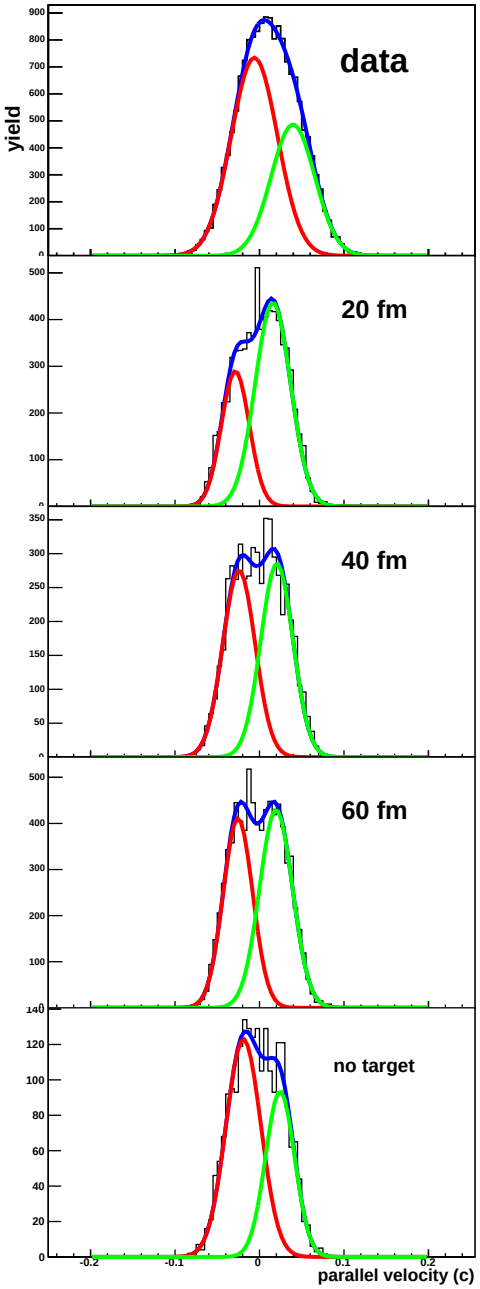

FIG. 66.: Parallel velocity plot for ^{12}C for the system ^{32}S + ^{112}Sn at 45 MeV/nucleon. From top to bottom are the experimental data, the DIT+SMM calculation at a fixed starting distance of 20 fm, 40 fm, and 60 fm, and the bottom panel is for no external Coulomb field (no target present for de-excitation).

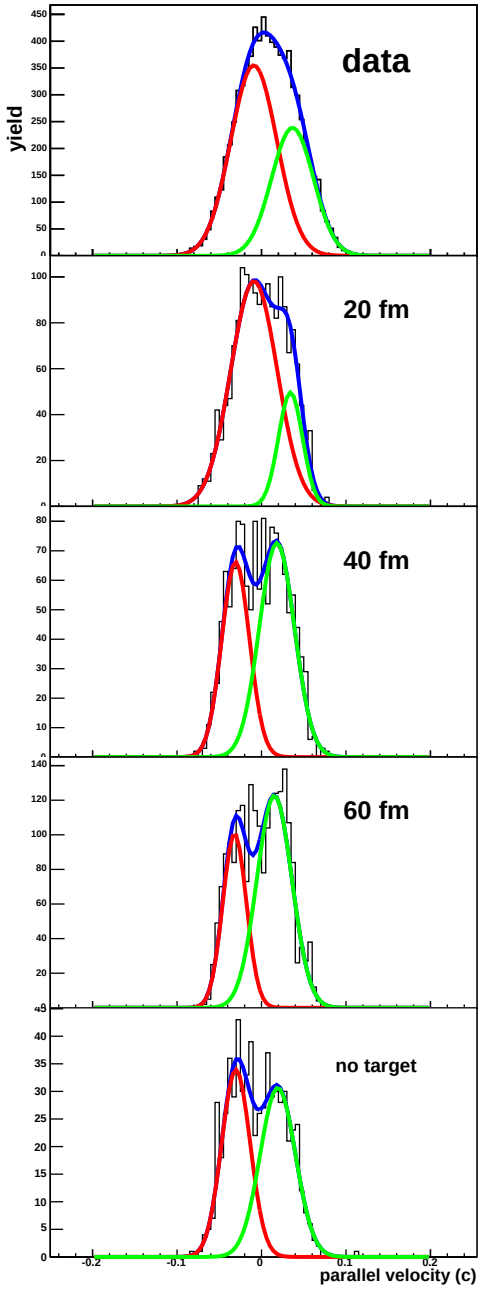

FIG. 67.: Parallel velocity plot for ^{13}C for the system ^{32}S + ^{112}Sn at 45 MeV/nucleon. From top to bottom are the experimental data, the DIT+SMM calculation at a fixed starting distance of 20 fm, 40 fm, and 60 fm, and the bottom panel is for no external Coulomb field (no target present for de-excitation).

VITA

Sarah Nicole Soisson

EDUCATION

Ph.D., Texas A&M University, Chemistry, December 2010

B.S., Stetson University, Chemistry, May 2003

EXPERIENCE

Senior Member Technical Staff, Sandia National Laboratories (2010 - present)

Nonproliferation Graduate Fellow, Pacific Northwest National Laboratory and the National Nuclear Security Administration (2009-2010)

Graduate Assistant Research, Texas A&M University (2003-2009)

Graduate Assistant Teaching, Texas A&M University (2003-2005)

CONTACT INFORMATION

Sarah Soisson can be reached through Dr. Sherry Yennello at the Cyclotron Institute, Texas A&M University, College Station, Texas, 77843-3366

E-mail: sarah.soisson@gmail.com

SELECTED AWARDS, SCHOLARSHIPS, AND ASSISTANTSHIPS

Department of Energy representative to the 55^{th} annual Nobel Laureate Conference(2005)

SELECTED AFFILIATIONS

American Physical Society (Since 2005), American Chemical Society (Since 2006)

SELECTED PUBLICATIONS

A dual-axis dual-lateral position sensitive detector for charged particle detection S.N. Soisson *et. al.* Nucl. Instrum. Methods Phys. Res. A 613 (2010)